Title

Wearable ultra-thin and flexible antenna for next generation wireless 5G networks and indoor localization using artificial intelligence algorithm

Permalink

https://escholarship.org/uc/item/94t4304r

Author

Ashrafi Nia, Behzad

Publication Date

2022

Peer reviewed|Thesis/dissertation

UNIVERSITY OF CALIFORNIA,
IRVINE

Wearable ultra-thin and flexible antenna for next generation wireless 5G networks and indoor localization using artificial intelligence algorithm

DISSERTATION

submitted in partial satisfaction of the requirements
for the degree of

DOCTOR OF PHILOSOPHY

in Electrical Engineering

by

Behzad Ashrafi Nia

Dissertation Committee:
Professor Franco De Flaviis, Chair
Professor Ender Ayanoglu
Professor Nader Bagherzadeh

2022

TABLE OF CONTENTS

LIST OF FIGURES

LIST OF TABLES

ACKNOWLEDGMENTS

VITA

Behzad Ashrafi Nia

EDUCATION

Doctor of Philosophy in Electrical and Computer Engineering **2022**
University of California, Irvine *Irvine , California*

Master of Science in Electrical Engineering **2015**
University of Tehran *Tehran , Tehran*

Bachelor of Science in Electrical Engineering **2012**
University of Isfahan *Isfahan, Isfahan*

RESEARCH EXPERIENCE

Graduate Research Assistant **2018–2022**
University of California, Irvine *Irvine, California*

Graduate Research Assistant **2012–2015**
University of Tehran *Tehran, Tehran*

TEACHING EXPERIENCE

Teaching Assistant **2019–2020**
University of California, Irvine *Irvine, California*

WORK EXPERIENCE

Wireless RF Design Engineer Intern **Summer 2022**
Tesla, Inc. *Palo Alto, California*

Display Hardware Engineering Intern **Summer 2021**
Apple, Inc. *Cupertino, California*

REFEREED JOURNAL PUBLICATIONS

A New Class of Ultra-low Profile, Highly Flexible Antenna Arrays for the 5G mm-wave Communication Band on Flexible Printed Circuit Board
URSI Radio Science Letters

2022

Compact Dual-Band Dual-Polarized Stack Patch Antenna Array With Capacitive Feed for Fifth-Generation (5G) Applications
URSI Radio Science Letters

2021

Applications of information channels to physics-informed neural networks for WiFi signal propagation simulation at the edge of the industrial internet of things
Neurocomputing

2021

REFEREED CONFERENCE PUBLICATIONS

Ultra Thin Dual-Polarized Flexible Patch Antenna for the 5G Communication
2022 IEEE AP-S

Jul 2022

Flexible Quasi-Yagi-Uda antenna for 5G communication
2021 IEEE AP-S

Jun 2021

Using the Convolutional Neuron Network for Target Localization and Wall Characterization in the Through the Wall Imaging Problem
EuCAP

Oct 2021

ABSTRACT OF THE DISSERTATION

Wearable ultra-thin and flexible antenna for next generation wireless 5G networks and indoor localization using artificial intelligence algorithm

By

Behzad Ashrafi Nia

Doctor of Philosophy in Electrical Engineering

University of California, Irvine, 2022

Professor Franco De Flaviis, Chair

The primary purpose of this dissertation is to address the critical issues in the development and design of a new class of antennas for the 5G application. Using mm-wave frequencies including 28 GHz and 38 GHz brings new challenges partially related to the high frequency of operation and partially related to the design of small low-cost phased arrays to operate at those frequencies. The first challenge in the 5G receiver and transmitter is the antenna design. When operating at high frequencies we need to overcome high path loss. To overcome this obstacle, a small antenna array with high gain and the ability to generate dynamically directional beams is desirable. Moreover, in a 5G cellular network using low cost, high efficiency, low weight, thin, and conformable (flexible) structures are desirable. The second challenge in using a flexible material is associated with its thickness which normally provides very narrowband designs. To the best of our knowledge, only a few antennas using a thin substrate with wideband and high-gain, have been reported. To address those two challenges, we present different types of compact and flexible antennas in single and linear array configurations operating at 28 GHz and 38 GHz. Second Purpose of this dissertation using Machine learning and AI in the n electromagnetic problems. To show, First we have presented an efficient scientific workflow that produces a Physics-Informed Convolutional Neural Network (CNN) model capable of running complicated electromagnetic wave propa-

gation (at WiFi frequencies) simulations to determine the real-time Received Signal Strength Intensity (RSSI) which can be used for determining wireless communication connectivity in advanced manufacturing contexts. These simulations are done in a constant enclosed space composed of inner objects with variable position, shape, size, and reflectivity. The workflow utilizes numerical PDE simulations to generate synthetic data for both training and testing states and suggests adaptive mechanisms to incorporate real-time sensed data to improve accuracy for geolocating people (inferred from their mobile technologies such as smart watches) moving through WiFi fields. The second application that we have investigated is related to using machine learning for the Through the Wall Imaging (TWI) problem. To solve the TWI problem in presence of the wall, a Convolution Neuron Network (CNN) is proposed. The detection of the scatterers behind the wall when there is a strong reflection from the front wall is very challenging. Several microwave imaging algorithms have been introduced to extract the unknown parameters of the wall and mitigate the wall clutter to predict the location of the target. This process is very time-consuming even though it has accurate results. In this paper, we developed a method for exploiting the complex information for the TWI problem by using a CNN that accepts complex numbers from the receiver to predict wall thickness, material, and location of the target behind the wall at the same time. We show that our proposed model can predict these parameters with an accuracy of 92.6%.

Chapter 1

Introduction

This chapter will first introduce the general background and research motivation of this work. Thereafter, a thesis overview will be provided.

1.1   The 5G era, challenges, and solutions

There are growing concerns about whether the current 4G wireless cellular system and its related mobile antenna configuration will be able to sustain the continuing demand for wireless traffic. The Fifth Generation (5G) mobile communication technology is considered a very attractive solution for exponentially expanding wireless data traffic in the future [1, 2], due to its ability to use significantly larger bandwidths at millimeter-wave (mm-wave) frequencies, which have been made available by the U.S. Federal Communications Commission (FCC). The new 5G bands include 28 GHz (27.5–28.35 GHz), 37 GHz (37–38.6 GHz), and 39 GHz (38.6–40 GHz). Moving to the mm-wave frequencies would bring new challenges partially related to the high frequency of operation and partially related to the design of small low-cost phased arrays to operate at those frequencies [3].

One of the challenges in the front-end of the 5G receiver is the antenna design. When operating at high frequencies we need to overcome high path loss. To overcome this obstacle, a small antenna array with high gain and the ability to generate dynamically directional beams is desirable. Moreover, for future 5th generation (5G) cellular networks, low cost, high efficiency, low weight, thin and conformable structures are envisaged as very desirable properties. Recent studies have demonstrated that roughly three times more base stations than anticipated are required to lunch 5G networks with excellent coverage. This translates into a coverage radius of 200 um or less. Existing 4G systems have a coverage radius of 500 m to 1 km [4]. This dissertation focuses on the development of low-cost flexible antennas and arrays to be used in portable devices such as smartphones, pads, and smart bracelets. The low-cost, flexible antenna offers a much faster and more cost-effective way of production. Recently, several electronic device fabrication technologies are moving towards low-loss and low-cost, flexible substrates such as polyimides, polyester, and polymers. The ability of Flex circuits to accommodate tightly bending radii and to eliminate the need for cables and connectors gives designers greater flexibility compared to traditional PCB. It enables products and applications that would not otherwise be possible, including vehicular, airborne, communication and navigation, cellular, and body-centric devices by simplifying a compact and reliable integration of wireless devices [5, 6, 7, 8, 9]. The use of recent low-cost and precise fabrication techniques on flexible materials (such as screen printing, laser prototyping, and injection printing) has provided the possibility for flexible antenna and circuits fabrication [10, 11, 12]. In this paper, subtractive processes have been used for the fabrication of the antenna [13]. This manufacturing method allows for low-cost antenna fabrication via high throughput production with inexpensive copper conductors, because 25um, 38um, and 50um layer dielectric thickness substrates are available. In this process, if desired, the thickness of the substrate can also be increased by stacking multiple layers. Previous work demonstrates the use of a flexible antenna at low frequencies [14, 15, 16, 17, 18, 19]. In this work, we extend the potential of flexible substrates to high-frequency antennas

for 5G applications. The second challenge in using a flexible material is associated with its thickness which normally provides very narrowband designs. Although some antenna concepts have been proposed for 5G wireless applications [20, 21, 22, 23], to the best of our knowledge, only a few antennas using a thin substrate with wideband and high-gain, have been reported [12], [24, 25, 26, 27]. In comparison to past work the proposed antennas, dominate in performance due to their flexibility, bandwidth, stable radiation pattern, and realizable gain. In this work, in order to address those two challenges, we present different types of compact and flexible antennas in linear array configurations operating at 28 GHz and 38 GHz.

1.2 Applications of Neural Networks in electromagnetic problems

WIFI Received Signal Strength Intensity (RSSI) mathematical models are typically based on Geometrical Optics (GO). This approach exploits a simplification of Maxwell's equations for the case when the emitted wavelength is much smaller than the objects and obstacles and hence the wavenumber tends to infinity $k \rightarrow \infty$ [28]. GO is widely used to compute WiFi converge simulations or WiFi-based applications because of its low computational cost [29, 30, 31].

Different approaches to computing the RSSI can be found in the literature. For example, a finite difference approach is shown in [32]. Herein, the authors predict WIFI coverage in a 3-story building by computing 2D simulations and then discuss the trade-offs between model complexity, accuracy, and computational cost. In [33], the authors compare 5 methods to simulate the RSSI by simplifying the process in order to obtain a faster computational solution. The described methods are: One-Slope Model [34], Dual-Slope Model, Partitioned

Model [35], Cost 231 Multi-Wall Model [33] and Average Walls Model [36]. They conclude that the Average Walls Model (AWS) is the most practical procedure for coverage estimation. By using AWS, the authors obtain a standard deviation of error between measured and predicted values of between 5 and 12 dB. Independently of the approach, the main source of error is typically caused by the diffraction behavior due to the channel effect [37].

In [38], the authors solve the inverse problem: Measuring the RSSI for range-based WIFI access point localization for the case when no information on the radio propagation model is provided. To achieve this goal, the authors linearly approximate the exponential relationship between RSSI and distance and apply a multilateration technique. Many authors' WIFI RSSI simulation's main purpose is indoor localization and most of these simulations mainly consider three parameters: time of arrival [39], angle of arrival [40] and time difference of arrival [41]. In [42], the authors propose a WiFi-based positioning algorithm that is claimed to reduce the number of antennas required by utilizing the transmission of multiple predefined messages. For this indoor localization purpose, due to its complexity and the importance of computing it in real-time, Artificial Intelligence (AI) is being deployed to decrease computational requirements. [43] is one of the first studies to use AI (backpropagation Neural Networks) to estimate the user location. In [44] the authors train a Neural Network (NN) to solve the hardware variance problem in RSSI-based WIFI localization systems and show its effectiveness for both variable-speed and constant-speed movement localization detection. [45, 46] are some examples of using Deep Neural Networks (DNNs) for improving indoor localization with robotic applications. Finally, in [37], the authors use Convolutional Neural Networks (CNNs), which will be the architecture used in this paper, to range error regression models in order to decrease indoor localization error due to the unpredictable nature of radio channel effects (such as reflection and diffraction).

Additionally, electromagnetic field simulations are found in many different fields with a wide range of applications. In [47] they construct a NN trained with a backpropagation algorithm

to predict the electromagnetic field created by a monopole antenna in the region inside a metallic enclosure and then compare the predicted values with the measurement done on a printed circuit board. In [48], the authors use NNs to reduce the computational effort of a 3D magnetic flux leakage compared to the traditional Finite Element Method (FEM). In [49], the authors build a NN in order to estimate the magnetic field strength near a power substation. In [50], Physics-informed Neural Networks (PINNs) are applied in order to emulate transient electrodynamics physics.

In recent years PINNs have become a cutting-edge topic with the idea of emulating physics by using DNNs. Other examples where PINNs have recently been applied are [51], where NNs are trained to solve supervised learning tasks while respecting laws of physics described by general nonlinear partial differential equations. As a more practical example, in [52], authors present a multi-physics approach based on NNs to solve various partial differential equations such as the Poisson equation, the Burgers equation, or the inverse problem for the Lorenz system. One of the most common PINNs applications has been fluid simulations [53?, 54]. For comparison purposes, [54] is very interesting as they apply a technique similar to what is proposed in this paper (i.e., using images to train the model to solve the same physics but in new random geometries) even if they solve completely different physics. A common technique for comparing real and predicted data, independent of the application, is the use of computer vision that treats the known terms and solutions of Partial Differential Equations (PDEs) on rectangular meshes as though they were images. Such methods approach the task of solving a PDE as an image-to-image translation problem similar to the pixel-to-pixel method proposed by [55]. In such a scenario, pixel values in a grey scale are considered for Initial Conditions (IC) and Dirichlet Boundary Conditions (BC). Therefore, the input of the NN will be an image of the BC, and its output is an RSSI heatmap.

In this work, we will demonstrate novel computationally efficient methods for developing high-fidelity NN-based RSSI simulations. The data acquisition effort will remain the most

significant time-consuming part, but by applying GO to our initial data acquisition we will demonstrate a significant decrease in the total computational cost. Also in order to improve the final results of our PINNs algorithm, we will inform the training stages via input channels that provide key physics-based information to the learning algorithms, i.e information channels. This approach decreases the amount of data required for training and hence the total effort of the overall computational workflow decreases as well. We will also show that we can train a NN to predict the RSSI for a random geometry representing machine locations on a factory floor with the antenna located in any position of this geometry. The resulting heat map of the RSSI can then be utilized for determining effective antenna locations that enable the communications between Industrial Internet of Things (IIoT) devices gathering data at the edge of advanced manufacturing facilities.

The other application of machine learning that we have successfully implemented in the previous topic in the Millimeter-wave frequency, is the thorough the wall imaging (TWI) problem via machine learning. Recent experiments in microwave imaging cover various applications such as radar imaging [56], object detection [57], medical imaging [58] and so on. Real-time through-the-wall imaging is one of the most interesting applications of this technology [59, 60, 61]. In a TWI system, the main goal is to detect and locate targets behind the wall by transmitting and receiving EM waves. The back-scattered signal from the wall and targets should be analyzed to extract the necessary information such as location, wall thickness, and dielectric constant. The main challenges in this process are unknown parameters of the wall, the strong reflection of the wall, and time-consuming algorithms to reconstruct images. In the introduced microwave imaging algorithms in the literature, first, we need to estimate wall parameters and then complex algorithms are required for clutter removal as wall reflection.

An alternative method that is introduced in this part of the research is in the area of machine learning (ML). This method is based on the statistical theory to extract the interesting,

practical, and unknown parameters from the big database. ML is a very practical way to extract information from big data. Support vector machines (SVMs) are new tools that by using optimization methods solve the problem of machine learning. Many applications based on the ML have been developed for the imaging problem such as through-the-wall imaging and synthetic aperture radar (SAR) [62, 63, 64].

In this work, we have introduced the Convolution Neuron Network (CNN) to provide comparative performance to the previous microwave imaging algorithms when TWI is considered as the regression problem. This method not only estimates the wall thickness and permittivity but also estimates the location of the target behind the wall. In comparison with traditional electromagnetic methods, our proposed approach needs only a few seconds to process the estimation. However, to the best of our knowledge, this is the first reported attempt to use ML in the TWI problem to extract four parameters one at a time. It means we can remove the back-scattered signal and at the same time roughly calculate the parameters of the wall and more importantly calculate the location of the target behind the wall, all at the same time and in one algorithm.

1.3 Overview

The first purpose of this dissertation is to develop a new class of ultra-low profile antenna arrays for the 5G mm-wave communication band on a flexible substrate by the emphasis on: (1) developing the most accurate model material characterization and simulation set up for the Millimeter-waves frequencies (2) The details of the design of the new class antenna for the 5G communication for ultra-thin material. The second purpose of this work is to present an efficient scientific workflow that produces a Convolutional Neural Network (CNN) model capable of running complicated Electromagnetic wave propagation (at Millimeter-waves) simulations to determine the real-time Received Signal Strength Intensity (RSSI) which can

be used for determining wireless communication connectivity in advanced manufacturing contexts. Moreover, by using a deep convolutional neural network, we have shown that we can predict the location of unknown targets as well as wall material and the thickness of the wall precisely and at the same time and with less time in comparison with previously proposed algorithms which are very complex. This result shows that this method can be utilized for suppressing the wall and background clutter as well.

Chapter 2, discusses the procedure used to characterize the dielectric constant of the flexible substrate and a new method for the optimization modeling of on-wafer measurements at millimeter-wave frequencies. This includes the probes and the lines connecting the probes with DUT in CST STUDIO SUITE.

In Chapter 3, each antenna design is discussed individually, and their advantages and disadvantages are highlighted. In this section also, the simulation and experimental results for single and array antennas are presented. Moreover, one of the proposed techniques is used to design a compact 4×4 dual-band dual-polarized (DBDP) antenna array with a wide bandwidth operating at the Ka-band is presented. A stacked patch topology is used for dual-band operation and feeding probes are used to excite the antenna array. Higher band elements have parasitic patches to achieve higher gain and increase the bandwidth. Moreover, a small metal ground on top of the common ground plane is designed for each element to suppress the coupling between the antenna elements and improve the beam scanning range effectively. The proposed antenna array with the size of $19mm \times 19mm$ operates at the center frequencies of 28 GHz and 38 GHz and the simulated results show that both wide bandwidth and stable gain were achieved.

In Chapter 4, we propose creating a novel method that exploits the notion of information channels to create efficient Convolutional Neural Networks (CNNs) capable of determining the RSSI given a completely new geometry (never used in training) where objects or obstacles (walls, machines, tables, etc.) and their respective location, size and reflectivity

indices, along with the antenna location are completely random. Also, we investigated the Through Wall Imaging (TWI) problem via machine learning. To solve the TWI problem in presence of the wall, a Convolution Neuron Network (CNN) is proposed. The detection of the scatterers behind the wall when there is a strong reflection from the front wall is very challenging. Several microwave imaging algorithms have been introduced to extract the unknown parameters of the wall and mitigate the wall clutter to predict the location of the target. This process is very time-consuming even though it has accurate results. In this work, we developed a method for exploiting the complex information for the TWI problem by using a CNN that accepts complex numbers from the receiver to predict wall thickness, material, and location of the target behind the wall at the same time. We show that our proposed model can predict these parameters with an accuracy of 92.6%.

Chapter 2

Material Characterization and Accurate EM Simulations for On-wafer Measurement Setup

In this chapter first In order to design a wide band and high gain antennas on flexible substrates, we developed an accurate substrate material characterization method. Secondly, we discuss the accurate 3D electromagnetic simulation techniques. The three dimension (3D) electromagnetic (EM) simulation is widely considered a very powerful tool for designing passive structures in millimeter-wave applications, such as antennas, filters, packaging and interconnects, and other structures [65]. 3D EM simulations solve Maxwell's equations in 3D spatial domains of the structure and provide EM field information. One may monitor the EM field distribution to analyze the EM characteristics of the designed structure. Important microwave parameters, such as S-parameters and propagation constants, can be derived after EM simulations for the purpose of passive device designs. However, with such wonderful tools, it is not straightforward to obtain accurate simulation results. For instance, incorrect excitation setups can result in nonsense results at the end of simulations. Therefore it is

necessary to develop a method to do accurate EM simulations. The technique of accurate 3D EM simulations will be discussed in this chapter.

2.1 Material Characterization for different thicknesses

While many substrates are treated as isotropic materials for design simplicity, in high-frequency applications they need to be characterized more accurately in case they exhibit some anisotropic properties. Glass and ceramic-filled polymer substrates, such as Duroid and Epsilam as well as sapphire, alumina, and a variety of other types of materials are anisotropic [65, 66, 67, 68]. Due to this, it is vital to investigate the anisotropy property of the material we are using in this work. The analysis of the resonance frequency of the proposed resonator antennas have been applied to the 50 µm thick substrate used for the Yagi antenna. This part of the paper aims to accurately calculate the resonance frequency of the proposed antenna on the anisotropic flexible substrate. However, to perform this analysis, the correct electromagnetic simulation setup is essential for accurate results. To meet this need, a ground-ring excitation setup is introduced to precisely model the G-S-G probe at the mm-wave application. The proposed method is validated by experimental results in the frequency range of interest. This setup can be considered Fig. 2.1. Far-field probe station set up. as the correct method for the simulation of GCPW structures with a finite ground plane for mm-waves applications in the CST STUDIO SUITE.

In this thesis, three thicknesses are used to design the antennas. The first one is 50 um and 120 um (Quasi Yagi-Uda antenna), and the third one is 202 µm (cavity-slot and patch antenna). Details of the design of each antenna will be discussed individually in the next section. The substrate used is called Pyralux@ TA laminate, which is designed for high-speed flex applications. Based on the datasheet, the relative permittivity and loss tangent are 3.2 and 0.004 at 10 GHz, respectively. The antennas are fed by a grounded co-planar waveguide
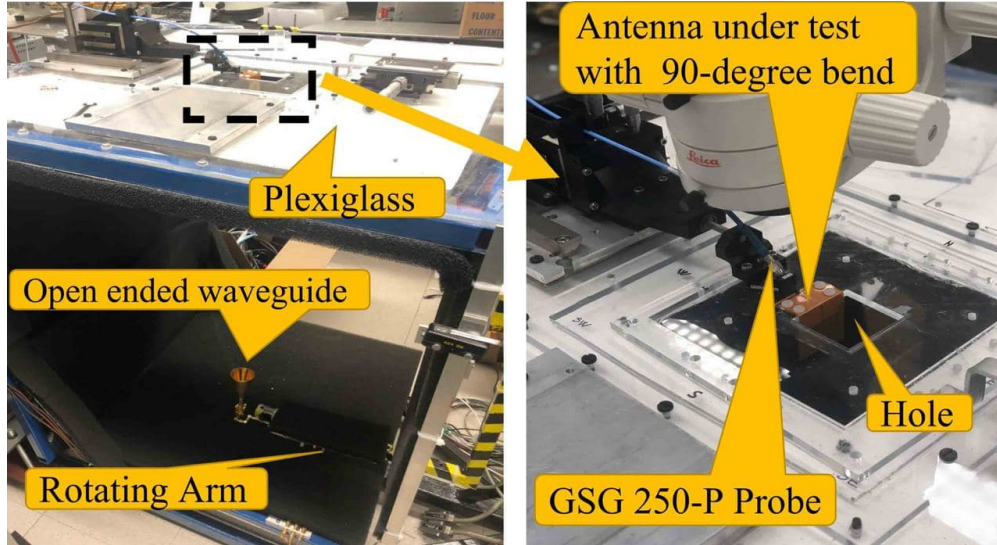
Figure 2.1: Far-field probe station set up.

(GCPW), and all the measurements are done using a custom-designed probe station, as illustrated in Fig 2.1.

This setup was designed at the University of California, Irvine, and offers a unique capability in allowing for probing while permitting the antenna to radiate in free space. In traditional probe station setups, where the samples are normally placed on a metal chuck for the measurement, the antenna radiation would be blocked by the metal and the return loss corrupted. To overcome these difficulties, the designed system consists of a probe positioner mounted on a large plexiglass plate, where a square hole in the center of the plate is used to support the antenna, leaving free its radiating side. Probing is done on the back side (with respect to the antenna radiation side). Therefore, the antenna is free to radiate downward during probing. The system is mounted on an optically isolated table for easy probing, equipped with a digital microscope. A computer-controlled rotating arm with a V band receiver moves around the antenna to collect its radiation, as shown in Fig. 2.1. Antenna, probe, and receiver antenna can be rotated by 90° individually, to allow the collecting four radiation patterns at each frequency (E-plane, H-plane, Co-pol and Cross-pol). A conical horn having 21 dB gain is used to calibrate the system and extract the absolute gain information of our antennas. To
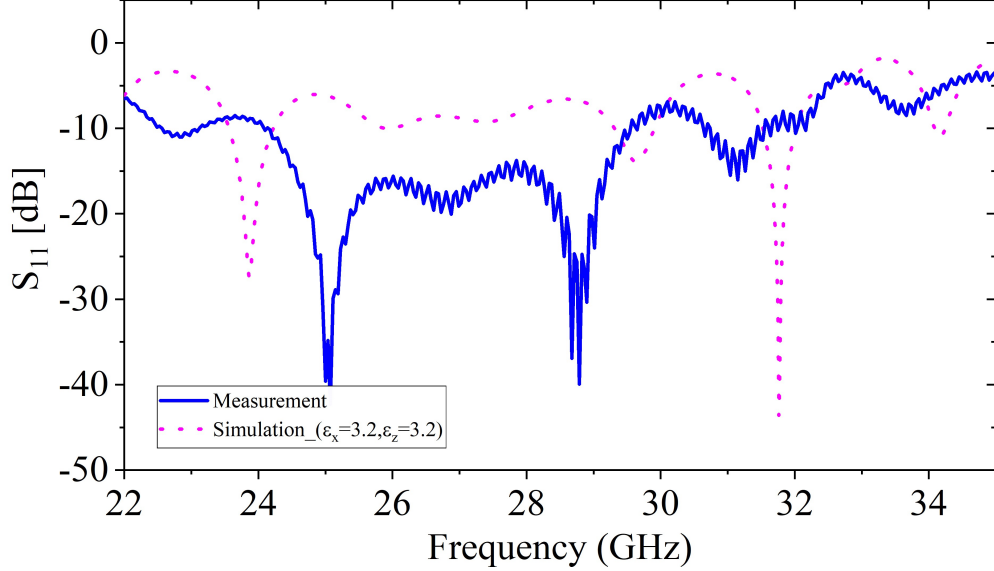
Figure 2.2: Simulation setup of the through the wall imaging problem.

estimate the substrate's effective dielectric constant, we recorded the resonance frequency of the Quasi Yagi-Uda antenna. Then we extracted the real part of the dielectric permittivity of the material. To achieve this, the exact layout of two fabricated antennas is simulated by CST STUDIO SUITE again, and S-parameters results are compared with measurement. The simulated and measured reflection coefficients (S11) of the Quasi Yagi-Uda antenna are presented in Fig. 2.2. After the analysis, it can be seen that there is a shift in the resonance frequency of the antenna.

Nelson et al. [69] investigated the frequency shift of the patch antenna based on the substrate's anisotropy effects. In this work, a more convenient method is used to investigate the effects of permittivity variation on resonance frequency for different thicknesses, which allows variation in both ϵ_z (relative permittivity along the optical axis) and $\epsilon_x = \epsilon_y$ (relative permittivity along the two axes perpendicular to the optical axis). Simulated return loss for the best-extracted value of ϵ_z and ϵ_x is shown in Fig. 2.3. The anisotropic ratio is not the only factor that needs to be considered. It can be concluded that changing the ϵ_z while keeping the Ex constant affects the operating frequency more strongly. This means the effect of permittivity variation along the optical axis is dominant. Results also show that the in-
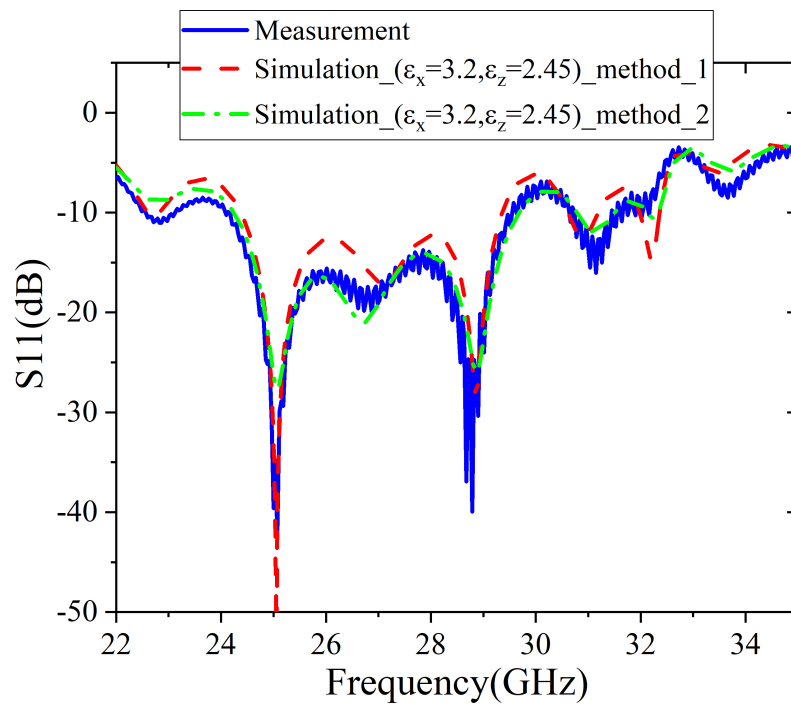
Figure 2.3: Comparison of two simulation setups for excitation of the GCPW line with measurement for the best extracted relative permittivity value of the anisotropic material (Quasi Yagi-Uda antenna).

Table 2.1: Relative permittivity for different thicknesses

Thickness	Dielectric Constant		
	ϵ_x	ϵ_y	ϵ_z
50 um	3.2	3.2	2.45
120 um	3.2	3.2	2.55
202 um	3.2	3.2	2.75

fluence of the variation of the relative permittivity tends to be higher for thinner substrates, while for a very thick substrate, it is predicted that it acts as an isotropic substrate. The same approach is applied for the substrate with 202 um and 120 um thickness and the best matched values are reported in Table I.

Even though measurement and simulation matched very well by choosing the values in Table I, there was a shift in the value of S11 (see Fig. 2.3, simulation method 1, Red curve). The possible reason for the frequency shift can be the modeling of the G-S-G probe at millimeter-wave frequencies. in the rest part of this chapter we will talk in more details about the accurate 3D simulation setup in CST STUDIO SUITE.

2.2 Different 3D EM Simulation Tools

The different domains will be used by the 3D EM simulation software to solve the EM problems. The domain is either frequency domain or time domain. In the frequency domain, the software uses the finite element method (FEM), Method of Moments (MoM), and finite integration technique (FIT). in the time domain, the most famous ones are FIT, finite difference time domain (FDTD) method and the transmission line method (TLM)[70].

2.2.1 Time Domain Tools

In an area of the time domain, the input port is excited by a Gaussian signal with broadband spectra and simulation will be started at this point. In the final, the time response of any point of interest is calculated while all output signals ideally decay to zero. After this step by using Fourier transform, the frequency response will be extracted. Because of using impulse shape, one run of the time domain simulation will generate an S-parameter in the whole range of frequency that we are interested in. One of the challenges of this method is when the device with high Q resonance is simulated by using this method. it is due to it taking a long time that inserted input power to decay to near zero. In this case, the convergence may take a lot of time and we need to consider this point. In conclusion, the time domain will not be efficient for the structure with a high Q factor. CST MICROWAVE STUDIO [71] is a full 3D EM simulator using FIT method. The transient solver in CST MICROWAVE STUDIO is the main feature of the software

2.2.2 Frequency Domain Tools

In the Frequency domain, the solver will build a matrix, and invert the matrix to find the solution [72]. The finite Element Method (FEM) is a typical approach in the frequency domain and solves the problem at each point of the frequency we are interested in. Due to using automatic mesh refinement even at arbitrary objects, FEM is a very powerful method to deal with almost any kind of structure. Since FEM can compute the multi-mode propagation in passive structures, mode conversions in structures can be observed in simulation results. It seems using the Frequency domain takes more time in comparison with the Time domain, because it needs to run the simulation multiple times at different frequency points. But, using the efficient tool which is "fast sweep" enables us to scan the whole frequency range and compute the frequency response just by one simulation run. CST MICROWAVE STUDIO

is a full 3D EM simulation software using the FEM method. all of the EM simulations in this thesis are implemented in CST MICROWAVE STUDIO. The following discussion about the accurate EM simulation techniques is mainly carried out based on CST MICROWAVE STUDIO. The accurate EM simulation methodology is discussed in the following.

2.2.3   Boundary Condition Setups

The correct setups of EM simulations are essential for having accurate and reasonable results at the end of simulations. almost all of the structures that are desired to be simulated are finite regions. Setting the boundary condition is very important to have correct setups of EM simulations and at the end of the simulation to have consistent results. The first proposed design of the antenna for the 5G communication in this thesis is the Yagi-Uda antenna. We have designed and confirmed our proposed accurate simulation setup based on this design. an air box is set as the solution region for the CST STUDIO simulator, and the surface of this box is defined as an open boundary condition which will be considered an open area and absorb the electromagnetic wave. The other boundary conditions that can be chosen are "perfect-E boundary" and "perfect-H boundary" which enforce parallel electric and magnetic component zero. Moreover, Some boundary conditions may also diminish the computation time in the simulation. This boundary condition which is called "Symmetric boundaries" can be utilized when may be placed at the symmetric plane of symmetric 3D models to reduce the size and complexity of the model by half. This boundary condition is used in optimizing the patch and cavity slot antenna in this thesis to save more time and memory. The finite conductivity boundary can also model the surface roughness loss. During our simulations and design, we consider the substrate roughness as conductive loss in the simulations by changing the conductivity of the copper. Moreover, the lumped element boundary introduces the possibility of utilizing lumped elements, such as resistors, capacitors and inductors, in 3D EM models.

2.2.4 Excitation Setups

3D EM models should be excited properly to extract relevant EM properties. Ports in the simulators enforce unique boundary conditions to insert power to the EM structure, As a result, excitation power in a correct mode is the precondition and a very important factor to computing and solving Maxwell's equations correctly. The characteristic parameters of the device like realized gain, S-parameters, and efficiency are highly dependent on the excitation setups. There is no comprehensive method to determine how to excite ports in the simulation in different software. Here we try to demonstrate ports' geometries when determining the excitation setup for two general excitation tools in the simulators which are the waveguide port and lumped port.

Waveguide ports have perfect-E boundary conditions on the related port edge because of the definition of a virtual semi-infinite long waveguide. The most common way to use waveguide ports is in structures such as coaxial cables, rectangular waveguides, and transmission lines including stripline, microstrip lines, CPWs, and GCPWs lines. One of the problems of this method is that the perfect-E boundary does not found in the real case scenario. As the result, the simulation results might be a little different by measurement.

There are different rules to set the size of the waveguide port to excite the different types of the structure. Fig. 2.4 demonstrates practical rules to determine the size of the waveguide port while we excite the structure. For all cases, the port edges should contact the ground planes of lines. Moreover, the width of the port should be large enough to avoid signal strip touch or be close to the edge of the waveguide port. The same point exists for the vertical distance too. The size of the waveguide port should be high enough to keep away from the signal strip. This case is more important for the microstrip and CPW lines. For instance, for the CPW line, the metal layer should evenly separate the waveguide port. More details are demonstrated in Fig. 2.4.

(a)

(b)

(c)

(d)
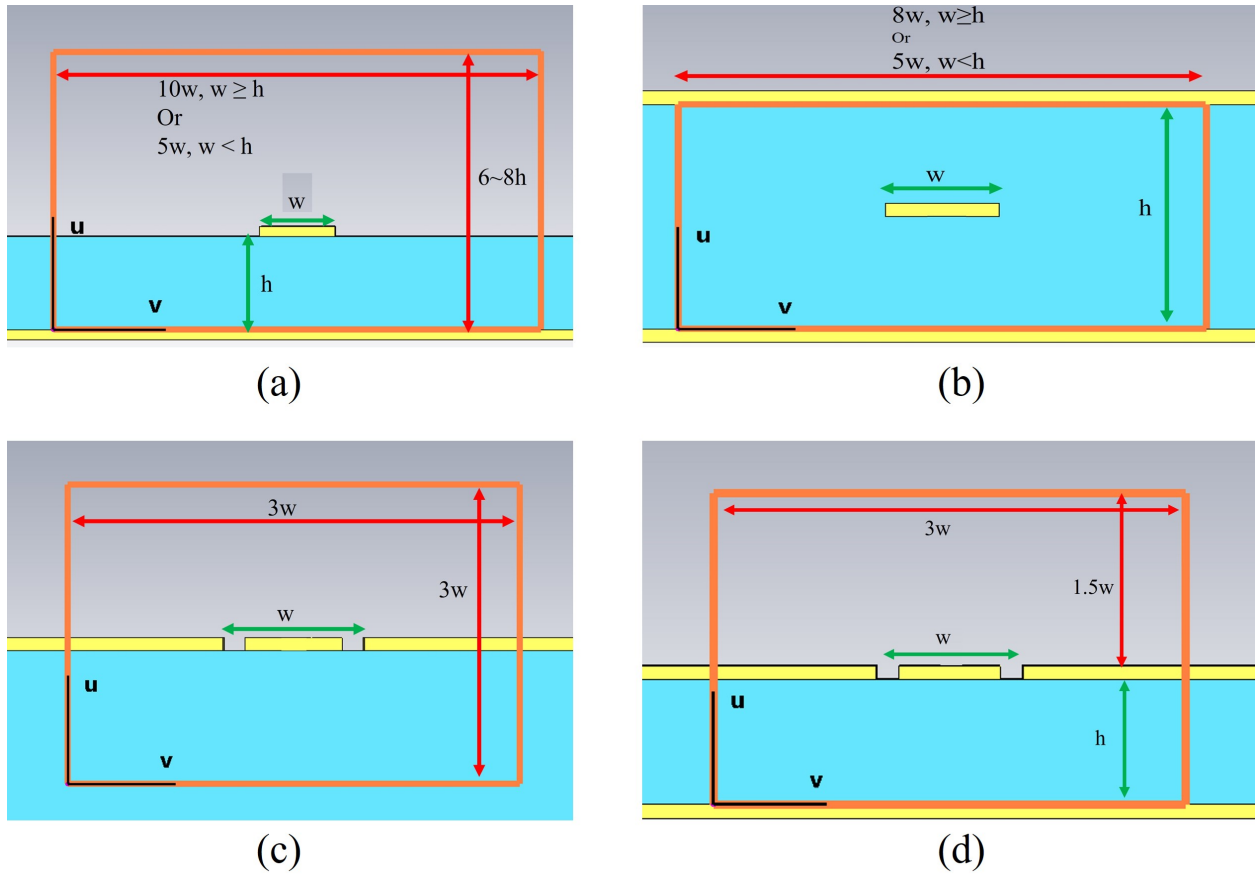
Figure 2.4: The wave port size specification for different planar transmission lines: (a) microstrip; (b) stripline; (c) CPW line; (d) GCPW line.

2.2.5 Accurate Simulations setup for On-Wafer Components

To model the on-wafer measurement at millimeter-wave frequencies, one needs to represent the exact excitation model of the measurement setup. This model should include the probes and the lines connecting the probes with the device. The measurement probes usually own a ground-signal-ground (G-S-G) configuration and contact the GCPW-like contacts while measuring the device. One can use a waveguide port as is explained in the previous part to excite the structure. But, the waveguide port has the tendency to distort the modes in the GCPW and CPW lines. The edge of the waveguide port can make artificial via holes and make the lines short at those points. By considering this fact, using the lumped port instead can solve this problem and make the simulation setup more accurate. In this thesis as we explained in the material characterization part in Fig. 2.3. Even though measurement and simulation matched very well by choosing the values in Table I, there was a shift in the value of S11 (see Fig. 2.3, simulation method 1, Red curve). The possible reason for the frequency shift can be the modeling of the G-S-G probe at millimeter-wave frequencies. An optimized version of the excitation setup which is named "simulation method 2" is shown in Fig. 2.4(b). Perfect electric conductor (PEC) sheets are used to connect the lumped port to the ground planes. This PEC sheet is associated with the lump port model the G-S-G probes better. These sheets are placed vertically on top of the contact pad and provide the same voltage for both ground planes. This excitation setup is referred to as "ground ring". By using this setup, simulation results are perfectly matched with measurements (see Fig. 2.3, simulation method 2, Green curve).

This section demonstrates an efficient simulation setup for the structures with the waveguide port excitation method and an accurate simulation setup for on-Wafer components, which improves the accuracy of results from EM simulations. Comparison between measured and simulated results for different configurations provides excellent agreement if the simulation data are calibrated using the proposed model. Especially at increased frequencies, this
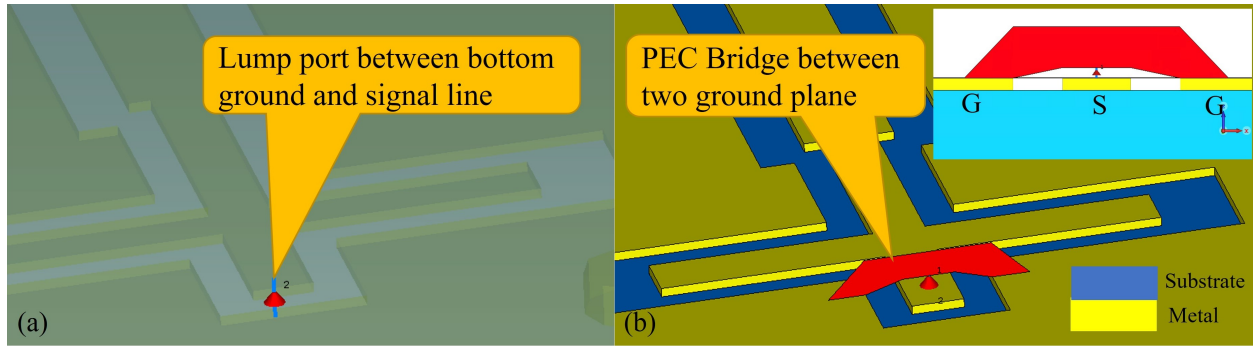
Figure 2.5: (a) Simulation setup for excitation of the GCPW line (method_1) and (b) Simulation setup for excitation of the GCPW line (method_2).

procedure ensures accurate results suitable for modeling purposes.

Now by knowing the properties of the substrate at 28 GHz and accurate EM simulation setup for the GCPW line, we can move forward to the next section and discuss in detail the designs of the three proposed antennas.

Chapter 3

Proposed 5G Antennas and Different Approach to Increase Bandwidth

In this section, the detail of each antenna is presented. These The antennas are Quasi Yagi-Uda, Patch, and Cavity-Slot antenna which has single and array topologies. A picture of the measurement setup used to measure the radiation pattern is shown in Fig. 3.1. It uses a vector network analyzer (VNA) and a custom probe station. Two transitions from the GCPW line to the embedded microstrip line and strip line are designed for patch and cavity-slot loop antennas, respectively. The Quasi Yagi-Uda antenna was tested under 90-degree bending conditions and results have shown excellent performance in the 28GHz region.

3.1 Compact Yagi-Uda Antenna

The Fifth-generation (5G) mobile communication is considered a very attractive solution for exponentially expanding wireless data traffic in the future, due to its ability to use significantly larger bandwidths at millimeter-wave (mm-wave) frequencies which have been
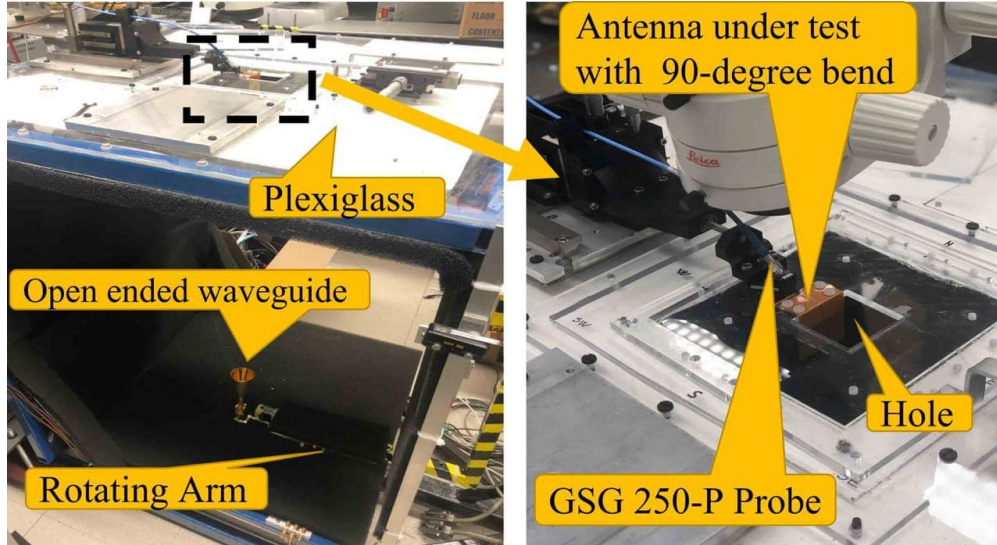
Figure 3.1: Far-field probe station set up.

available by the U.S. Federal Communications Commission (FCC). This frequency range includes a new licensed spectrum located in the 28 GHz (27.5–28.35 GHz), 37 GHz (37–38.6 GHz), and 39 GHz (38.6–40 GHz) bands. Unfortunately, switching to the mm-Waves would bring us new challenges and certainly needs more consideration on the antenna design for 5G devices. One of the limitations with mm-Waves wireless communication is the increased path loss because of large propagation attenuation at mm-Wave frequencies. In order to overcome this obstacle, the antenna array with wideband, high gain, and the ability to generate directional beams, stable radiation characteristics are desirable. The small wavelengths of mm-Wave frequencies facilitate the use of multiple number antenna elements in a compact size and enable us to have higher gain. Among different types of the antennas, such as patch, and slot, the end-fire antennas including Quasi-Yagi, Dipole, and Vivaldi are more suitable to cover the required cover-space of 5G cellular communication. Among them, the Quasi-Yagi antenna has more potential due to its high gain, easy fabrication, stable radiation pattern, and compact size. In this study, we have selected the frequency band of 28GHz as the design target. Design of compact Quasi-Yagi–Uda antennas with end-fire radiation are presented for mm-Wave wireless applications. The proposed Quasi-Yagi antenna is on a low-cost, single-substrate-layer flexible printed circuit (FPC). Flexible substrate materials

have brought advanced electronic circuits into products ranging from smartphones to medical devices. The ability of flex circuits to accommodate tight bending radii and eliminate the need for cables and connectors gives designers greater flexibility and enables products that would not otherwise be possible. Another key factor for flex material is to have a low loss tangent across a wide range of frequencies, including 28 and 38 GHz, which make them a good choice for 5G mm-wave applications.

The schematic of the proposed antenna is shown in Fig. 3.2. which has GCPW feeding. The antenna is constructed on the modified polyimide (MPI) material by MFLEX, which is designed for high-speed flex applications. Key property advantages of this material are Low dielectric constant (2.85), Low loss tangent (0.004), Tight thickness tolerance, Better bendability, and Low moisture absorption. The total thickness of the substrate in this design is only 120um. This antenna is fed by a grounded coplanar waveguide (GCPW) to a microstrip line and a dipole, which is designed by half-wavelength resonance at 28GHz. A microstrip to parallel-strip balun is used to feed the dipole in balanced mode. Then two arms of each dipole are printed on both sides of the substrate. Also, two directors are employed in front of the dipole, which directs the antenna propagation toward the end-fire direction and helps to improve the directivity of the radiation pattern. Moreover, these elements act as impedance matching elements. Meanwhile, two sets of reflectors are used on both sides of the substrate for effective reflection of back-radiated electromagnetic waves.

After successfully developing and design of a single element of the Quasi-Yagi antenna, this study also explores the schematic and characterization of the array antenna with four elements of the Quasi-Yagi antenna for applications in 5G platforms. As you can see in Fig. 3.3, four elements of the antenna are placed on both sides of the substrate and fed by a T junction power divider.

The Fabricated Quasi-Yagi antenna is shown in Fig. 3.3. The full-wave simulation was performed using CST STUDIO SUITE. All the measurements were done by a far-field probe
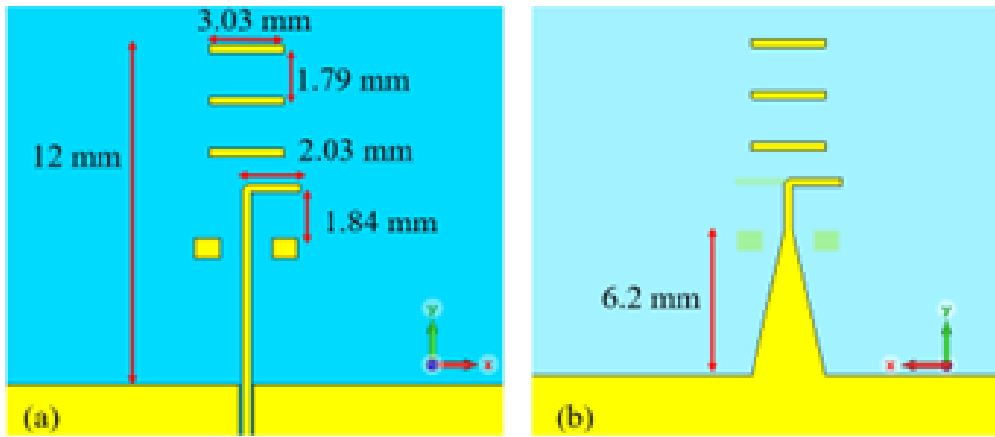
Figure 3.2: Structure of proposed antenna. (a) top view and (b) bottom view.
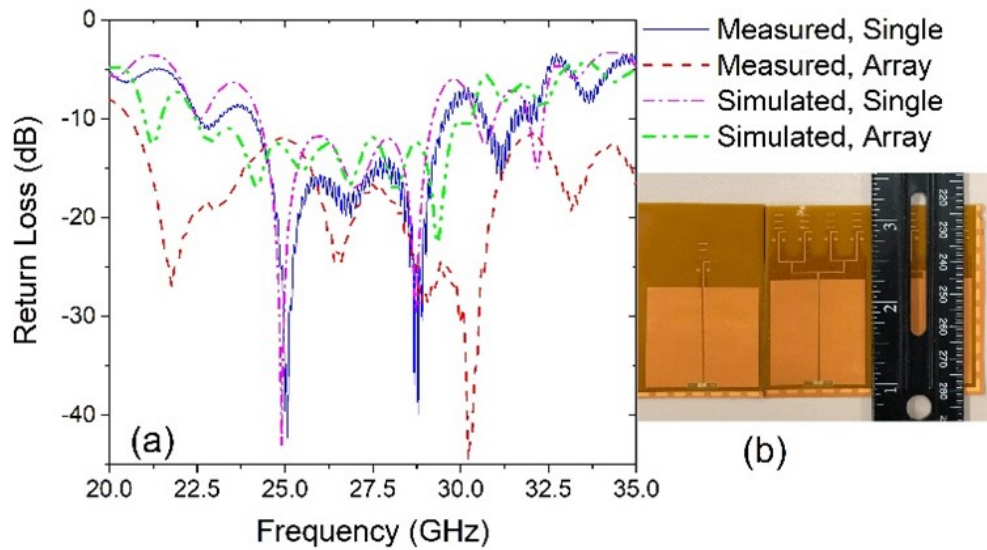
Figure 3.3: (a) Measured and simulated result of S parameters. (b) fabricated antennas.
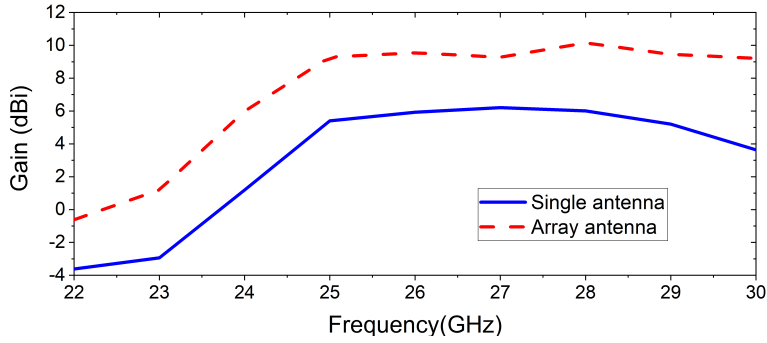
Figure 3.4: Measured Gain of single and array Quasi-Yagi-Uda antenna over frequency.

station system, and the GSG-250-P probe was used to excite the GCPW line. Simulated and measured S-parameters are shown in Fig. 2, where good agreement is obtained. Both single and array antennas have a measured bandwidth from 23 to 30GHz; thus, a wide frequency coverage is realized. Measured pick gain also is shown for both single element and array antenna in Fig. 3. The measured gain is almost stable in the range of the operation and is in the range of 5.2 6.2 dBi for a single element and 9.2 10.2 dBi for an array antenna.

Measured and simulated far-field radiation patterns at 28GHz are compared in Fig. 4. It can be observed the measurement results approved the simulation in both E-plane and H-plane. The patterns of the single antenna show the HPBW of 50° and 58° in the H-and E-planes, and the array antenna shows the HPBW of 60° and 21° in the H-and E-planes, respectively.

In this part, a high gain, wideband Yagi-Uda antenna at 28GHz with the vertical end-fire radiation has been proposed. The antenna has been designed on a flex substrate. The design has resulted in good agreements between the simulated and measured in the single array. Measurements show the average realized gain of the single antenna is about 6.2dBi, impedance bandwidth of 25.7% covering from 23 to 29.8 GHz, and the radiation efficiency is up to 88%. Therefore, the proposed antenna is a good candidate for the 5G communication systems.

After the first design and make sure the structure is designed to thin as much as possible. in
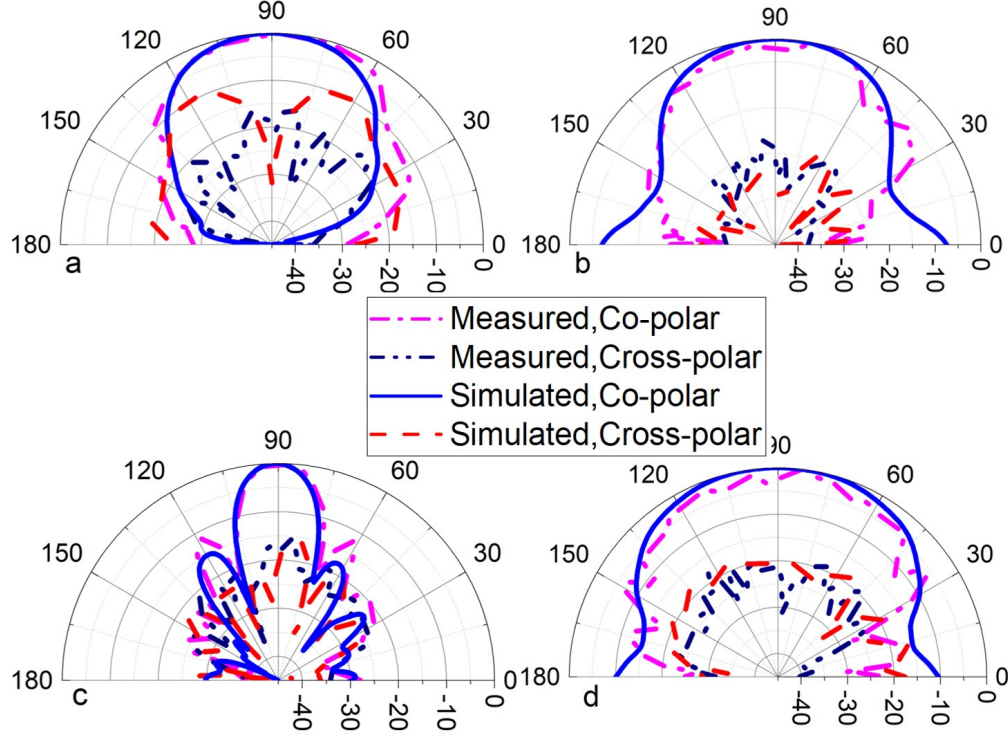
Figure 3.5: Measured and simulated radiation pattern at 28GHz. (a) At E-plane (single). (b) At H-plane (single). (c) At E-plane (Array). (c) At H-plane (Array).

the next stage, a substrate with a total thickness of 50um is utilized to design a Quasi-Yagi antenna. Again the antenna consists of a printed strip dipole operating at 28 GHz with two quarter-wavelength legs located on either side of the substrate. On the top side of the substrate, the GCPW line is connected to the dipole antenna, where the impedance of the parallel strip is equal to the impedance of the antenna which is as same as the previous design. On the bottom side of the substrate, the width of the ground plane is gradually tapered to the microstrip line and parallel strip. The taper accomplishes the mode and impedance transformation. Three directors are employed in front of the dipole to direct the radiated field toward the end-fire direction while simultaneously improving the directivity of the radiation pattern as well as the gain. Meanwhile, the distance between the dipole antenna and the ground reflector planes is approximately one-quarter of a wavelength to improve the back-radiation effects. All optimized geometry dimensions of the antenna are presented in table 3.1.
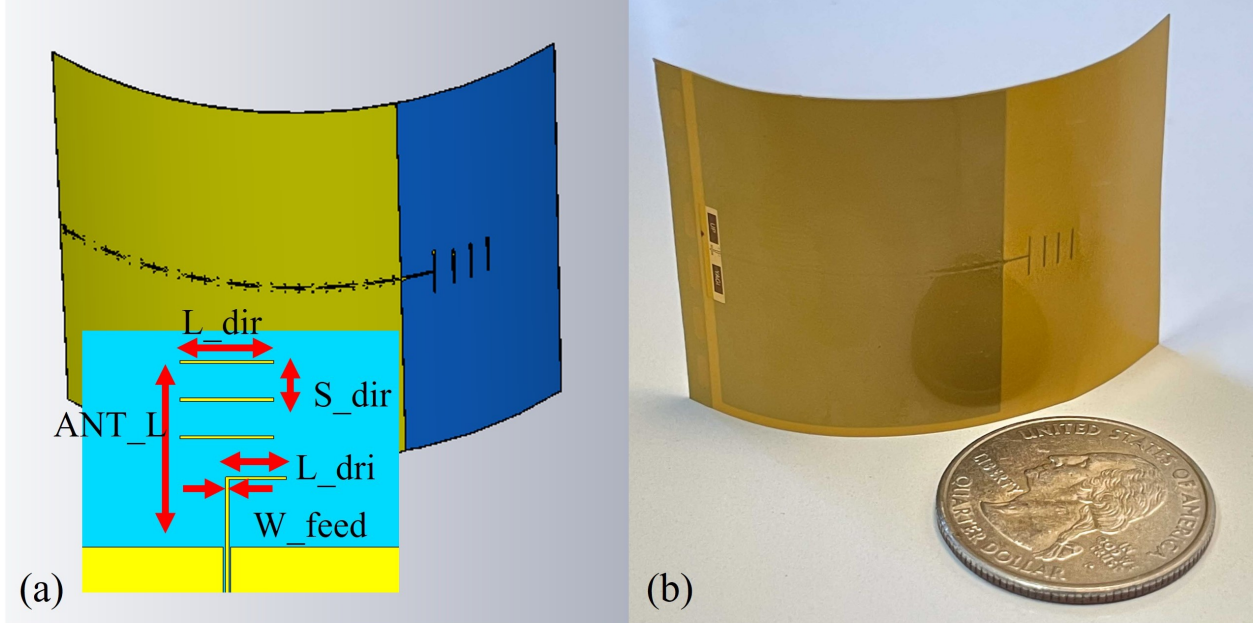
Figure 3.6: (a) The geometry of the proposed antenna, (b) Prototype of the fabricated Quasi Yagi-Uda antenna.

Table 3.1: Parameters of the Quasi Yagi-Uda antenna

ANT_L	L_dri	W_feed	L_dir	S_dir
6.8 mm	2.03 mm	0.120 mm	3.3 mm	1.4 mm

Next, the Quasi Yagi-Uda antenna is used in a four-element linear array. These antennas are spaced 7.5 mm from each other and they are all fed simultaneously by one T-junction power divider.

The simulated and measured S-parameters of the proposed antennas are shown in Fig. 3.7. Good agreement is observed between them. Both single element and antenna array exhibit a measured wideband performance from 24.7 to 30.8 GHz, and 24.2 to 31.6 GHz, respectively. Measured peak gain versus frequency is also shown for both single element and array antenna in Fig. 3.7. The measured gain is essentially stable in the operation range and between 5.2~6.2 dBi for the single element and 9.2~11.4 dBi for the array antenna. In theory, it is expected that the four-element antenna array will add 6 dBi to the total realized gain, but in the lower frequency the improvement is around 4.5 dBi, and this is in part due to the T-junction characteristic (which is not as wide-band as the Quasi Yagi-Uda antenna) and
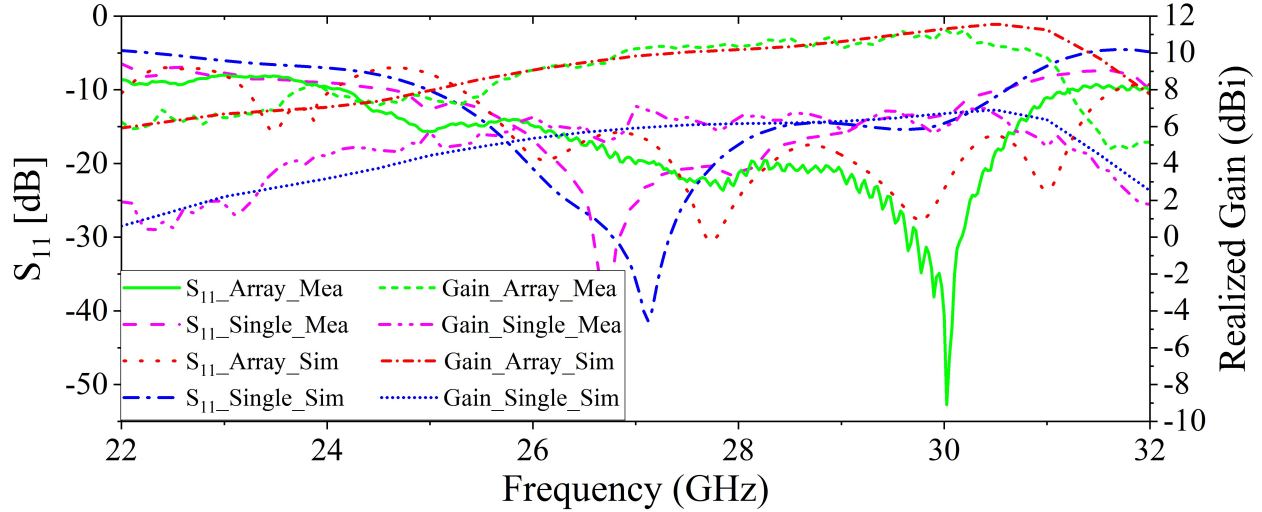
Figure 3.7: S-parameter and realized gain of the proposed Quasi Yagi-Uda antenna (with 90° bend).

therefore cannot cover the entire frequency band of the proposed antenna.

The measured and simulated far-field radiation patterns at 28 GHz are compared in Fig. 3.8. Good agreement is obtained in both E-plane and H-plane. The single antenna shows half power beam width (HPBW) of 50° and 58° in the H-and E-planes, respectively. The array has HPBW of 60° and 21° in the H-and E-planes,

In this part, a high gain, wideband Yagi-Uda antenna at 28GHz with the vertical end-fire radiation on 50 um and 120 um substrate has been proposed. The antenna has been designed on a flex substrate. The design has resulted in good agreements between the simulated and measured in the single array.

3.2 Patch Antenna Design

In this section, the geometry for the patch antenna is introduced which is suitable for a thin substrate. The patch antenna is printed on a 202 μm thick substrate and is designed to resonate at 28 GHz. The geometry of the proposed antenna is depicted in Fig. 3.9. In
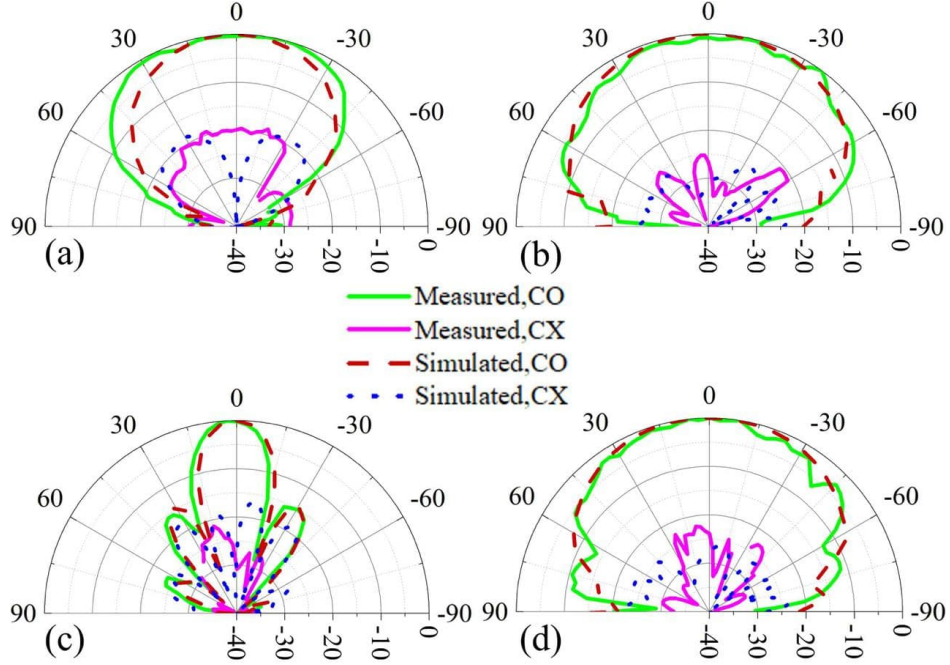
Figure 3.8: Simulated and measured radiation patterns of the proposed Quasi Yagi-Uda antenna at 28 GHz (a) E-plane (single), (b) H-plane (single), (c) E-plane (Array), (d) H-plane (Array) (with 90° bend).

general, the bandwidth of the typical patch antenna would not exceed 5%, however, to meet the requirement of the 5G millimeter-wave band and increase the bandwidth on such a thin substrate, a capacitive feeding method and parasitic rectangular elements around the main patch are implemented. The capacitive feeding method counteracts the inductance of the via which is connected to the embedded microstrip line under the main patch. The proposed antenna can also be used as a dual-polarized antenna due to its symmetrical structure which is explained shortly.

Eliminating the corner section of the patch can help to tune the resonance frequency by decreasing the length of the current path.

Moreover, to improve the bandwidth and gain of the antenna, four parasitic rectangular elements are added to the same layer. These parasitic elements can add a new resonance near the primary patch resonance and as a result, increase the bandwidth.
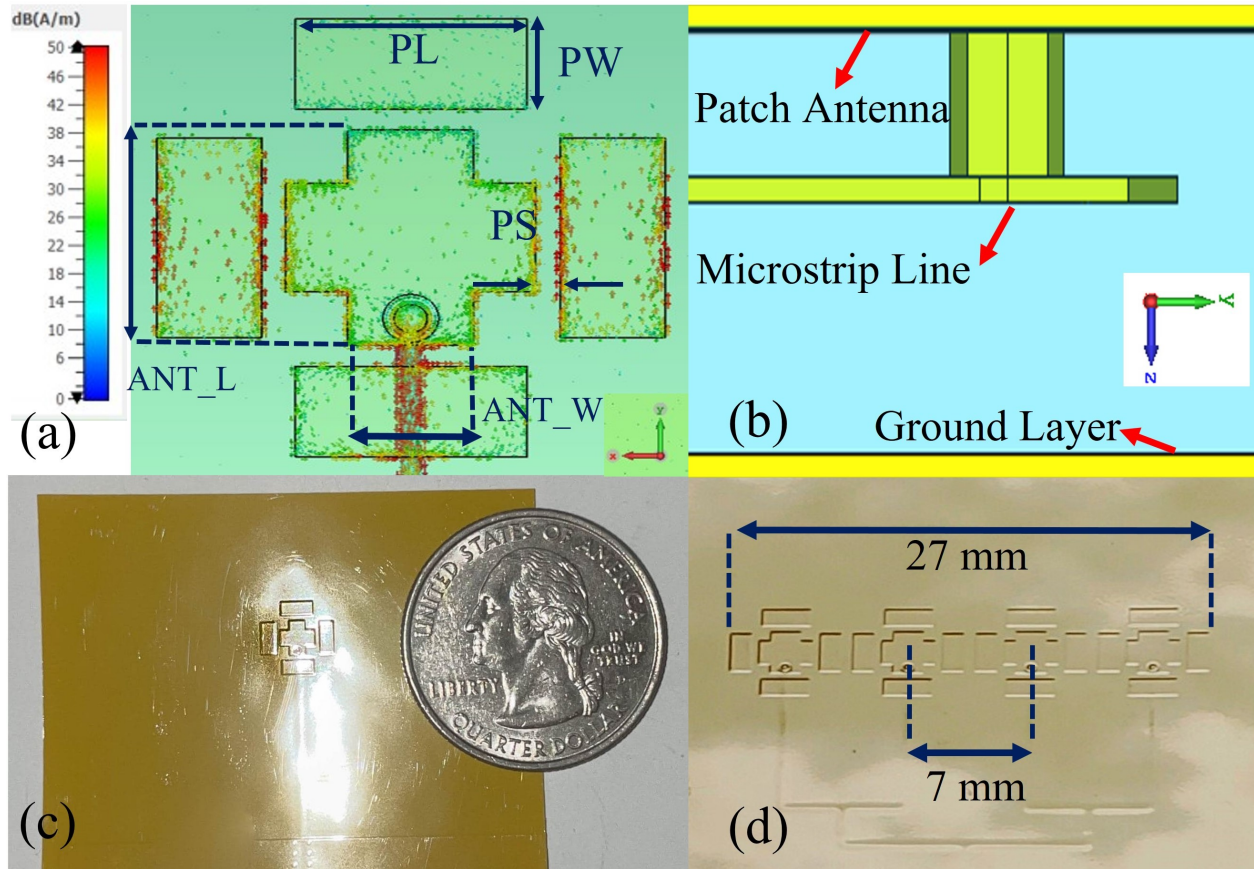
Figure 3.9: (a) The geometry and distribution of the current surface at the resonance frequency of the proposed antenna, (b) side view, (c) and (d) fabricated single and array antennas.

The overall size of the proposed patch antenna, including parasitic elements, is 6.5 mm × 6.5 mm. The optimized value of each parameter in Fig. 3.9 is shown in table 3.2.

In this design, only one port is used to excite the antenna, and therefore a GCPW line to embedded microstrip with a vertical transition is used to excite the patch antenna by using a capacitive feed. A feed network comprised of microstrip lines and a T-junction is used to integrate the patch in a 1×4 linear array which is shown in Fig. 3.9(d). The size of the linear array is 7 mm × 29 mm. The simulated and measured S-parameter results for both

Table 3.2: Parameters of the patch antenna

ANT_L	ANT_W	PL	PW	PS
3.25 mm	1.5 mm	3 mm	1.3 mm	0.45 mm
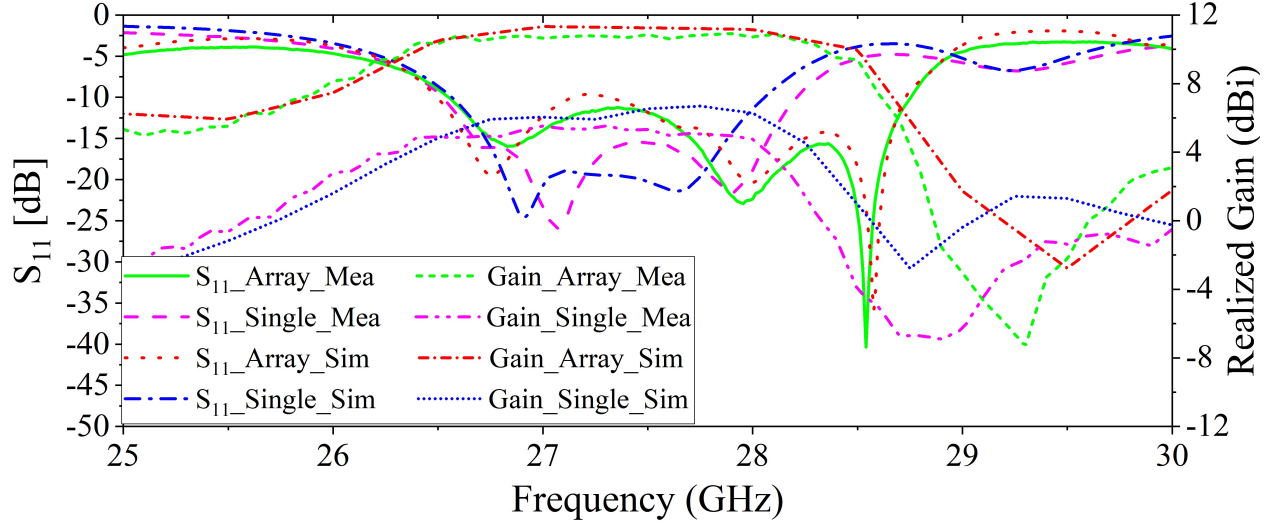
Figure 3.10: S-parameter and realized gain of the patch antenna vs frequency.

single and array elements are shown in Fig. 3.10. The -10 dB impedance bandwidth covers 26.5-28.3 GHz and 26.4-28.7 GHz for the single and array elements, respectively.

The realized gain of the single and array antenna versus frequency has been measured and compared with simulation in Fig. 3.10. The average gain of the single patch antenna is above 4.2 dBi and the array average gain is 10.2 dBi within their bandwidth. It is worth mentioning that the antenna array has a maximum realized gain of around 10.8 dB at 28.3 GHz, which makes it a good candidate for 5G Communications.

In Fig 3.11(a)-(d), the simulated and measured E-plane and H-plane, co-polarization and cross polarization at 28 GHz are plotted. The 3-dB beam width is 16.6° (H-Plane) and 79° (E-Plane) for the array element and 45° (H-Plane) and 86° (E-Plane) for a single element. The cross-polarization level is around 25 dB.

While most the antenna design is a linearly polarized antennas, in the real case scenario the devices will face a different kind of movement in the Euler area which adds more loss to the characteristic loss in mm-waves which is miss polarization loss between transmitter and receiver antennas. To use the full ability of the 5G in communications, the antenna with dual polarization is recommended and plays the critical key to overcoming radiation
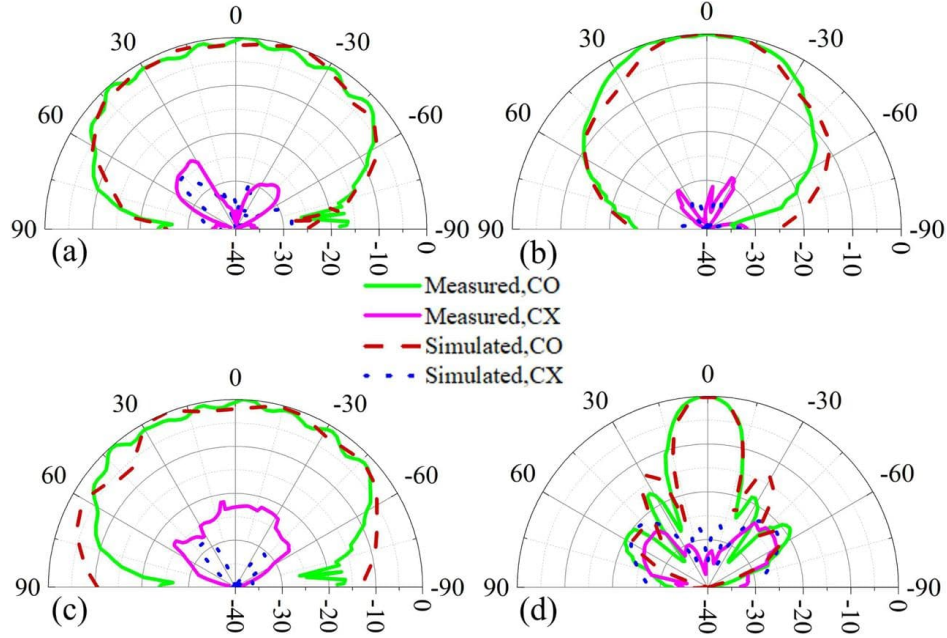
Figure 3.11: Simulated and measured radiation pattern of the proposed patch antenna at 28GHz (a) E-plane (single), (b) H-plane (single), (c) E-plane (Array), (d) H-plane (Array).

loss and increasing the data rate of the 5G network [73]. In addition, having devices with smaller sizes, low cost, thin and conformable, and flexible structures are very desirable. The geometry and dimensions of the dual-polarized flexible patch antenna operating at 28 GHz are depicted in Fig. 3.12. Both single and array patch elements are printed on a substrate with a thickness of 202 um. The main patch antenna with its parasitic elements has a total size of 6.3 mm × 6.3 mm. The GCPW line to the embedded microstrip line is used to excite two polarizations of the antenna by capacitive feed and enable it to transmit and receive two orthogonal signals at the same time in the same aperture the other part of the design is the same as the previous design. This configuration shows a low level of cross-polarization around 20 dB for both single and array elements.

A 1×4 linear array with a T-junction power divider is designed with a size of 6.3 mm × 27.5 mm. The S-parameters of the proposed antenna is shown in Fig. 3.13 and 3.14. The comparison shows simulations and experimental results are consistent with each other. Reflection coefficients of the proposed antenna achieved wide bandwidth from two ports
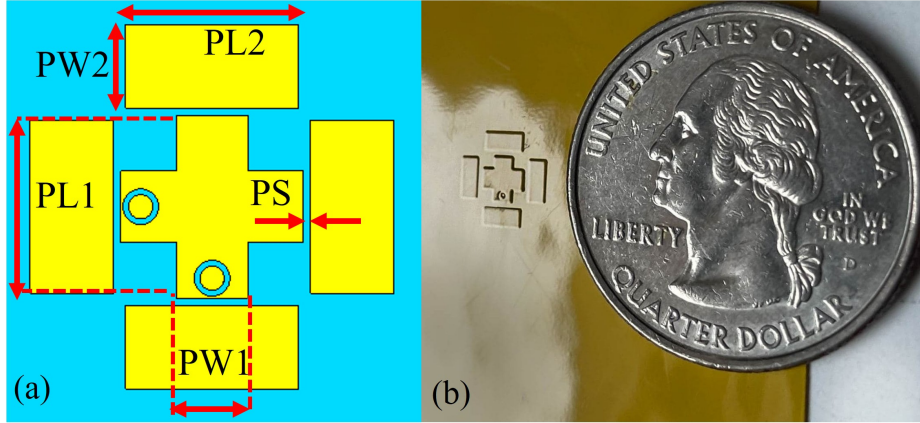
Figure 3.12: The geometry of the proposed antenna, (b) Prototype of the fabricated patch antenna.. PL1=3.17 mm, PL2=3 mm, PW1=1.24 mm, PW2=1.4 mm, and PS=0.150 mm.

with 1.9 GHz and 2.4 GHz bandwidth for single and array antennas, respectively. One can notice that the worst isolation coefficient in the desired operation bandwidth is around 20 dB between port 1 and port 2. It has a sufficient gain of 6.5 dBi and 12.3 dBi for the single and array antenna, respectively over the bandwidth and it is depicted in Fig. 3.15. The simulated far-field radiation patterns at 28 GHz are shown in Fig. 3.16. The simulated 3-dB gain-beamwidth is 73°, 65°, 19.3°, and 64° for the H-plane single, E-plane single, H-plane array, and E-plane array antenna, respectively for both vertical and horizontal ports. By aforementioned properties, the proposed dual-polarized patch antenna can be practical in 5G communications in addition to providing flexible properties.

In this part, a compact flexible single and dual-polarized patch antenna for a 5G communication system with relatively large bandwidth coverage on 202 um substrates is designed for both single and array topology. Dual polarization antenna benefits to overcoming high attenuation in 5G systems. Moreover, the proposed antenna achieved high efficiency of 80%. In addition, high isolation of around 20 dB between the ports is achieved. The resultant antenna offers dual-polarized at 28 GHz having impedance bandwidths of 1.9 GHz and 2.4 GHz for single and array elements, respectively. The average gain offered by the proposed antennas over the operating bandwidth is about 6.5 dBi and 12.3 dBi in single and array

Figure 3.13: S-parameter of the patch antenna vs frequency(single element).
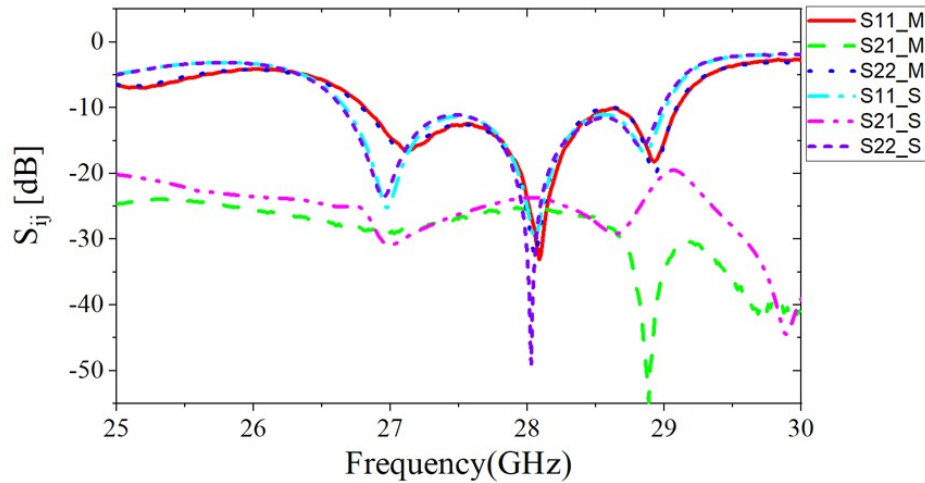
Figure 3.14: S-parameter of the patch antenna vs frequency(array element).

antennas, respectively. Antenna performance indicates that it is a potential candidate for 5G cellular communication and Ka-band applications.

3.3   Cavity slot Antenna Design

In this section, an original mm-wave cavity slot antenna design is presented as shown in Figs. 3.17. The cavity slot antenna is also a good candidate for this frequency band due

Figure 3.15: Realized gain of the patch antenna vs frequency.

Figure 3.16: Radiation pattern at 28GHz for vertical port. (a) At E-plane (single). (b) At E-plane (Array). (c) At H-plane (Single). (d) At H-plane (Array).

to its compact size, shielding, easy fabrication, and low profile. In addition, the cavity slot antenna is more compact and has better cross-polarization in comparison to the proposed

patch antenna. The cavity slot antenna is also etched on a 202 μm thickness substrate. The circle-ring slot is etched on the ground plane on the backside of the substrate. Ground vias are placed around the ring to connect the bottom ground layer to the top ground layer to create a cavity. The cavity is excited by a stripline feed. The feed line is extended and tapered beyond the slot to form a tuning stub. The tapered stub helps to reduce the high impedance offered by the small cavity slot by balancing out the reactive part of the circle-ring slot with its impedance represented by Rs+jωLs while exciting the resonance frequency. The initial design is a narrow gap ring slot that offers a high impedance and narrow bandwidth. However, because the substrate is very thin, it is very challenging to have a wideband antenna at this frequency. To overcome this issue, four stepped stub arms are etched with 90-degree separation to increase the bandwidth and create a symmetric structure to provide a big co-pol to cross-pol ratio. These arms are shown in Fig. 3.17(a) as ARC2 and ARC3.

A general expression for the resonance frequency of the stepped slot antenna can be given as:

$$f = \frac{c}{4 \times L_A} \tag{3.1}$$

Where c is the speed of the light and L_A is the active length of the slot. The first and second resonance of the slot can be written as follows [?]:

$$L_{A1} = L_{S1} + 2 \times L_{S2} + 2 \times L_{S3} + 2 \times \frac{(W_{S2} - W_{S_1})}{2} + \\ 2 \times \frac{(W_{S_3} - W_{S2})}{2} \tag{3.2}$$
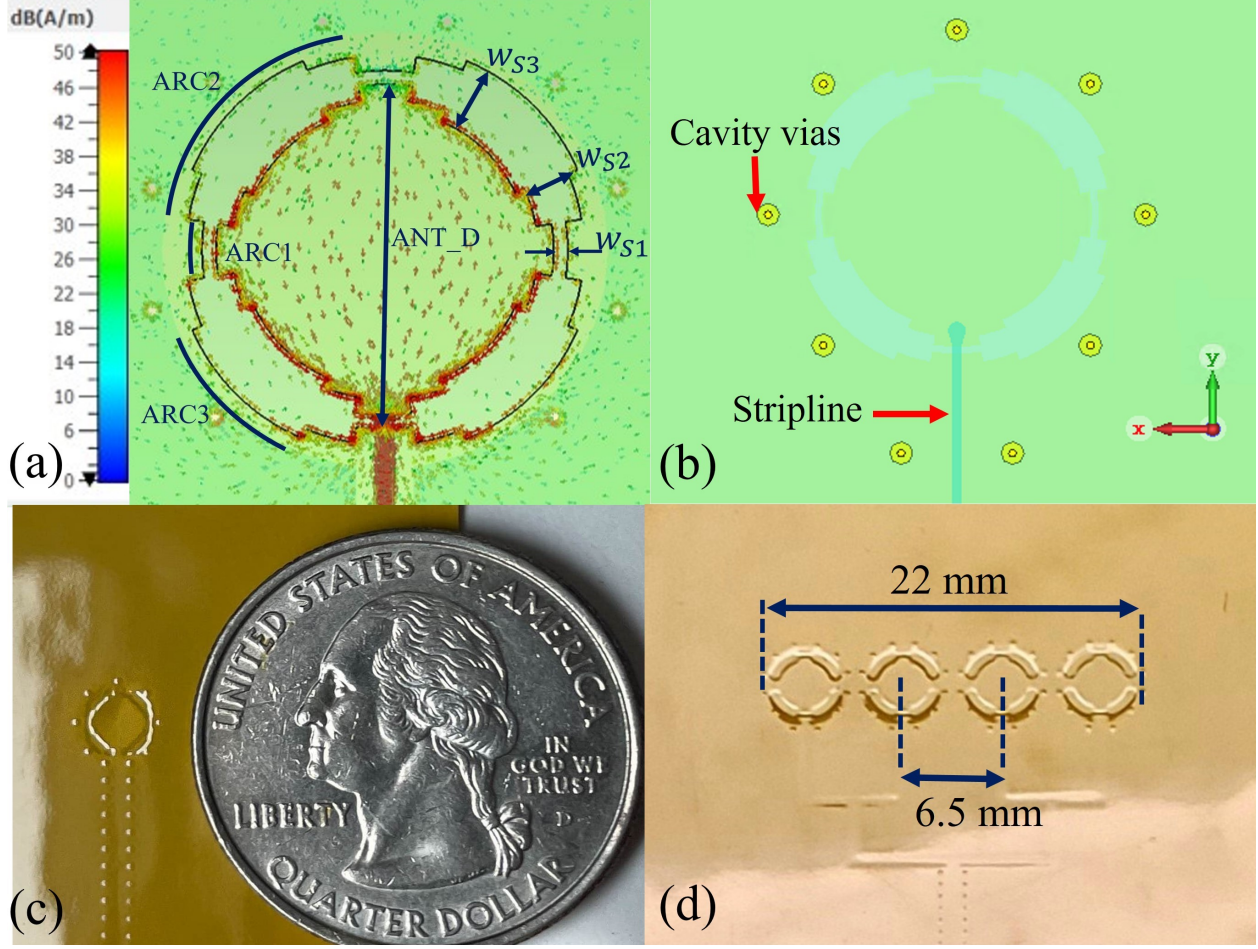
Figure 3.17: (a) The geometry and distribution of the current surface at the resonance frequency of the proposed antenna, (b) transparent top view, (c) and (d) fabricated single and array antennas.

$$L_{A2} = 2 \times \left(L_{S2} + L_{S3} + \frac{(W_{S2} - W_{S1})}{2} + \frac{(W_{S3} - W_{S2})}{2} \right) \tag{3.3}$$

Where $L_{S1} = \frac{ANT_D}{2} \times ARC1$, $L_{S2} = \frac{ANT_D}{2} \times \frac{ARC2-ARC3}{2}$ and $L_{S3} = \frac{ANT_D}{2} \times \frac{ARC3}{2}$. The first and second resonance frequencies are set to be around 27 GHz and 28 GHz. Then by tuning the width and length (the portion is extended outwards from the ring slot loop) of the stubs in the ring slot and stub of the feeding line, good impedance matching can be achieved by merging two resonance frequencies. This occurs because these additional current paths,

38

Table 3.3: PARAMETERS OF THE CAVITY SLOT ANTENNA

ANT_D	W_{S1}	W_{S2}	W_{S3}	ARC1	ARC2	ARC3
3.5 mm	0.09 mm	0.35 mm	0.508 mm	14°	76°	48°
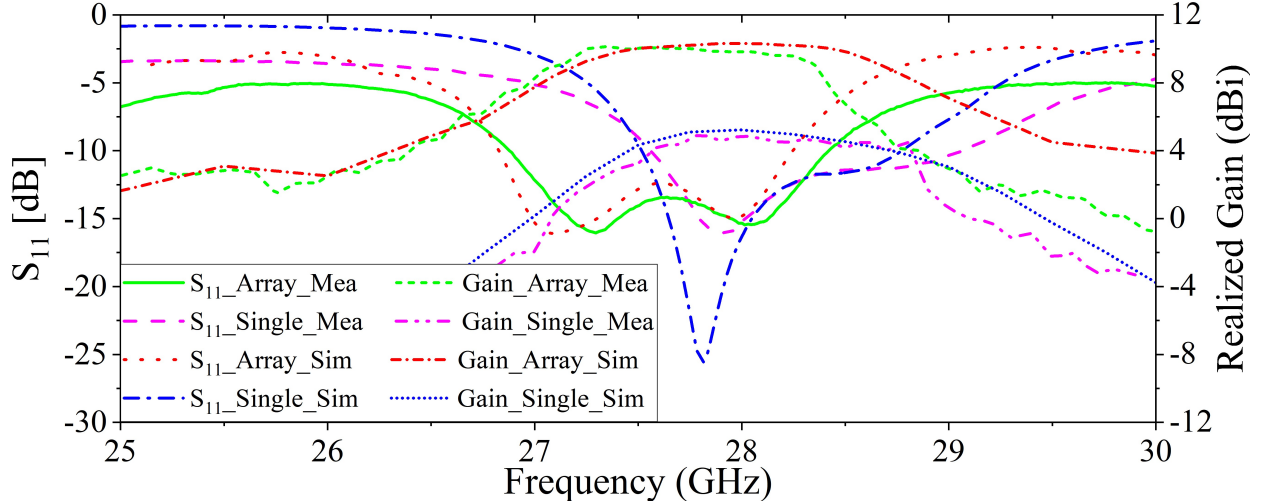
Figure 3.18: S-parameter and realized gain of the proposed cavity slot antenna.

create a resonance near the primary resonance of the cavity slot antenna. The gap in the ring slot remains narrow to improve the coupling power from the stripline to the antenna. Also, these stubs enlarge the aperture for radiation, and therefore increase the realized gain of the antenna. Moreover, the proposed antenna is symmetric with respect to the origin in the xy-plane. This configuration gives a low level of cross polarization around 35 dB which is due to the symmetry of the electrical field across the aperture of radiation. The parameter values of the designed antenna are shown in table IV.

After designing a single element of the antenna, a 1×4 linear array is designed as well. The total size of the array area is 3.6 mm × 22 mm. The S_{11} parameters of the proposed single element and array antenna were measured and Fig. 3.18 shows a comparison with simulation. There is good agreement between the curves if we consider S_{11}<-10 dB as good impedance matching. The single element and array antennas have a bandwidth of 1.55 GHz, [27.6-29.15] GHz, 1.7 GHz, [26.7-28.4] GHz, respectively.

The simulated and measured radiation pattern of the single and the array element are il-
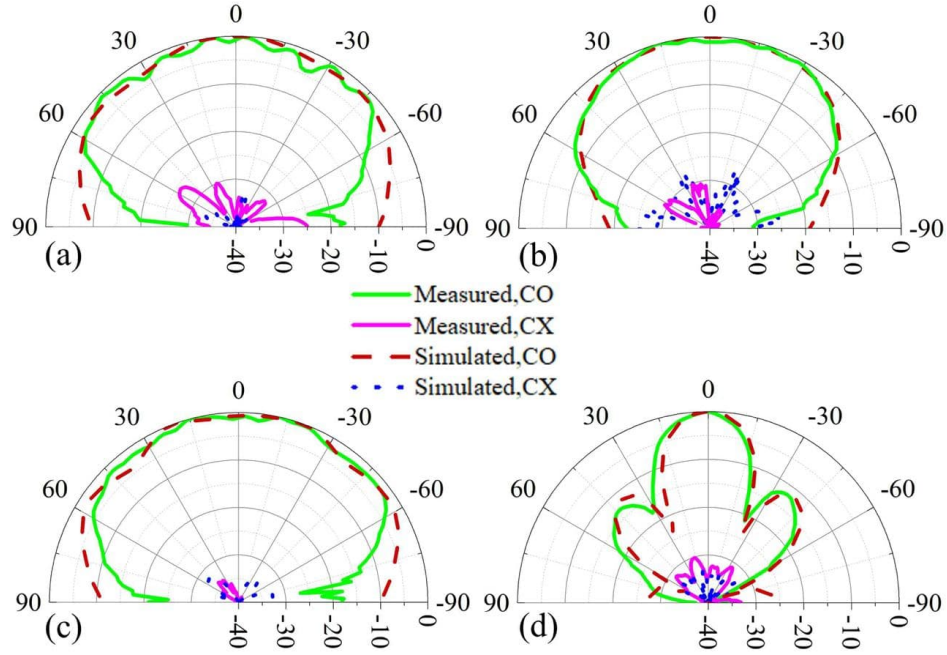
Figure 3.19: Simulated and measured radiation patterns of the proposed cavity slot antenna at 28GHz (a) E-plane (single), (b) H-plane (single), (c) E-plane (Array), (d) H-plane (Array).

lustrated in Fig. 3.19. In the two main orthogonal radiation planes (E-plane and H-plane), according to the plots, the half-power beam width of a single element is 46° and 89° for H-plane and E-plane respectively, and 23° and 73° for H-plane and E-plane respectively for the array element. Measured and simulated realized gain for the two types of antenna are plotted in Fig. 3.18. The maximum gain is 4.6 dB and 10.3 dB for single and array elements, respectively.

Same as patch antenna, after successfully implementation of the single polarized antenna, dual-polarized cavity-slot antenna is investigated. The S-parameters of the proposed antenna is shown in Fig. 3.20 and 3.21. The comparison shows simulations and experimental results are consistent with each other. Reflection coefficients of the proposed antenna achieved bandwidth from two ports with 0.94 GHz and 1.65 GHz bandwidth for single and array antennas, respectively.

The worst isolation coefficient in the desired operation bandwidth is around 35 dB between
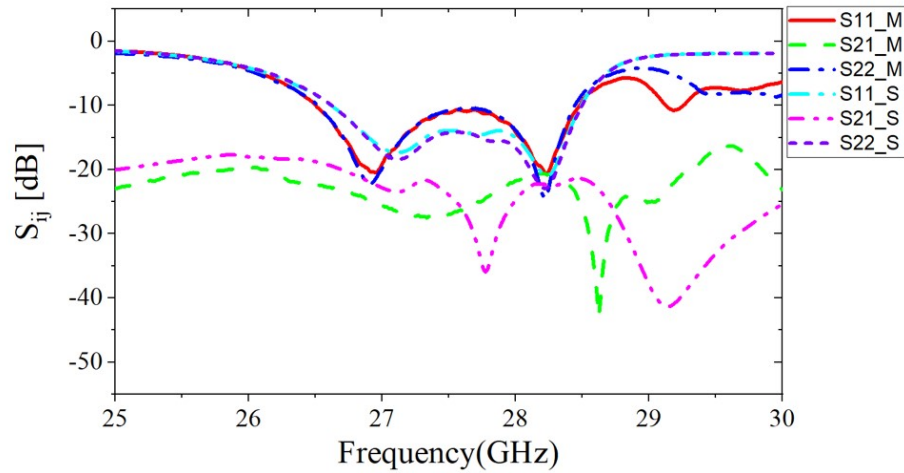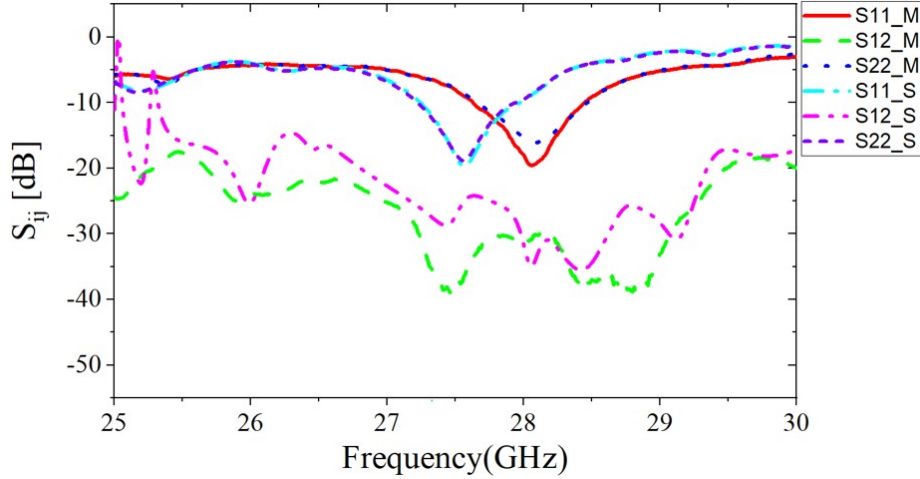
Figure 3.20: S-parameter of the Cavity-slot antenna vs frequency(single element).
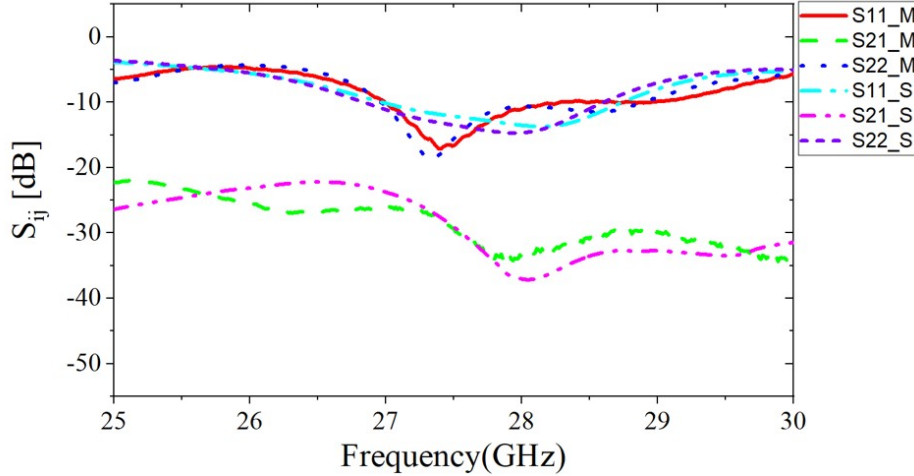
Figure 3.21: S-parameter of the Cavity-slot antenna vs frequency(Array element)

port 1 and port 2. It has a sufficient gain of 5.5 dBi and 9.1 dBi for the single and array antenna, respectively over the bandwidth and it is depicted in Fig. 3.22. The simulated far-field radiation patterns at 28 GHz are shown in Fig. 3.23. The simulated 3-dB gain-beamwidth is 77°, 63°, 18.4°, and 71° for the H-plane single, E-plane single, H-plane array, and E-plane array antenna, respectively for both vertical and horizontal ports.

In this part, a compact flexible single and dual polarized Cavity-slot antenna for a 5G communication system with relatively large bandwidth coverage on 202 um substrates is designed for both single and array topology. High isolation of around 30 dB between the
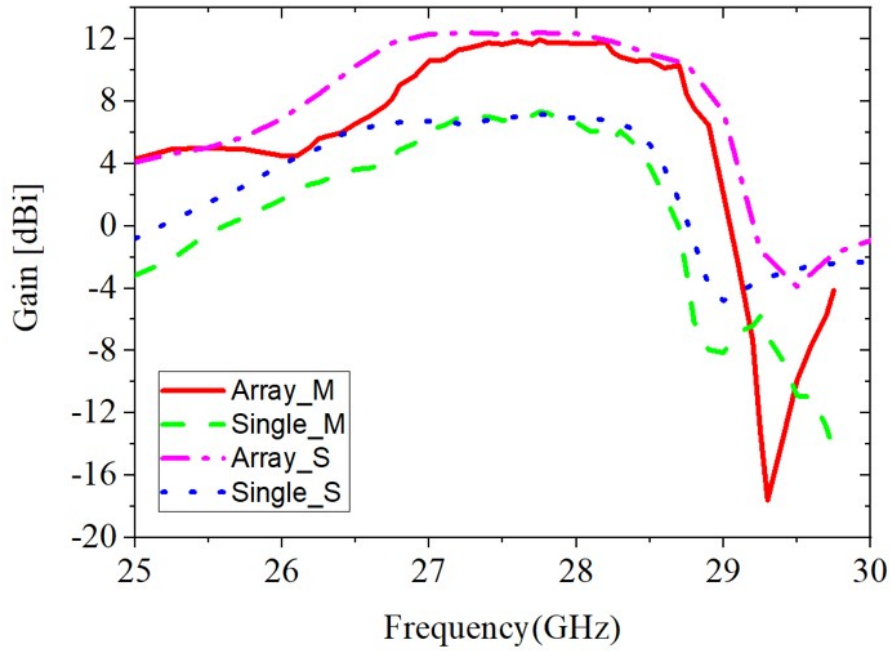
41

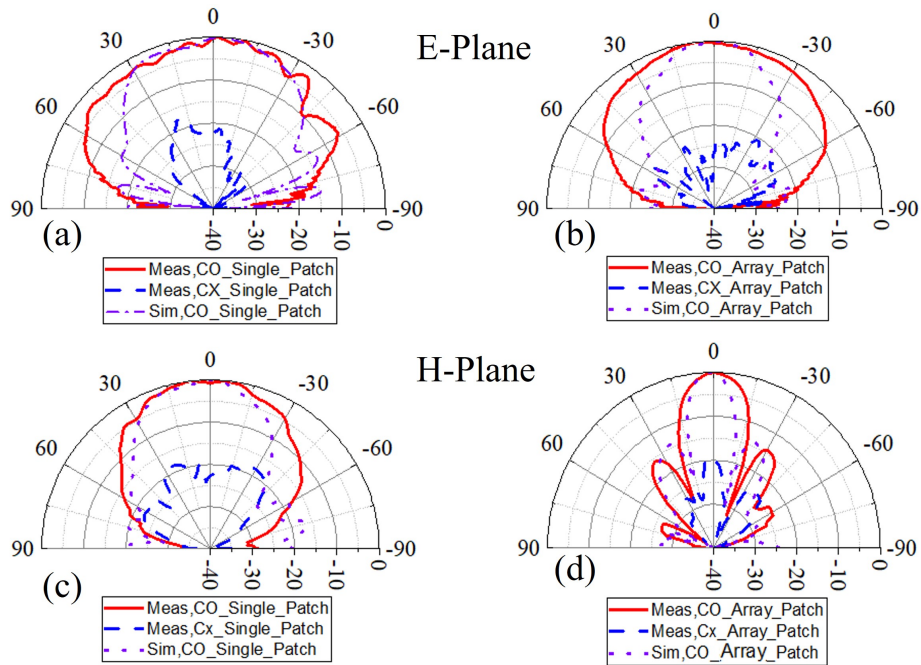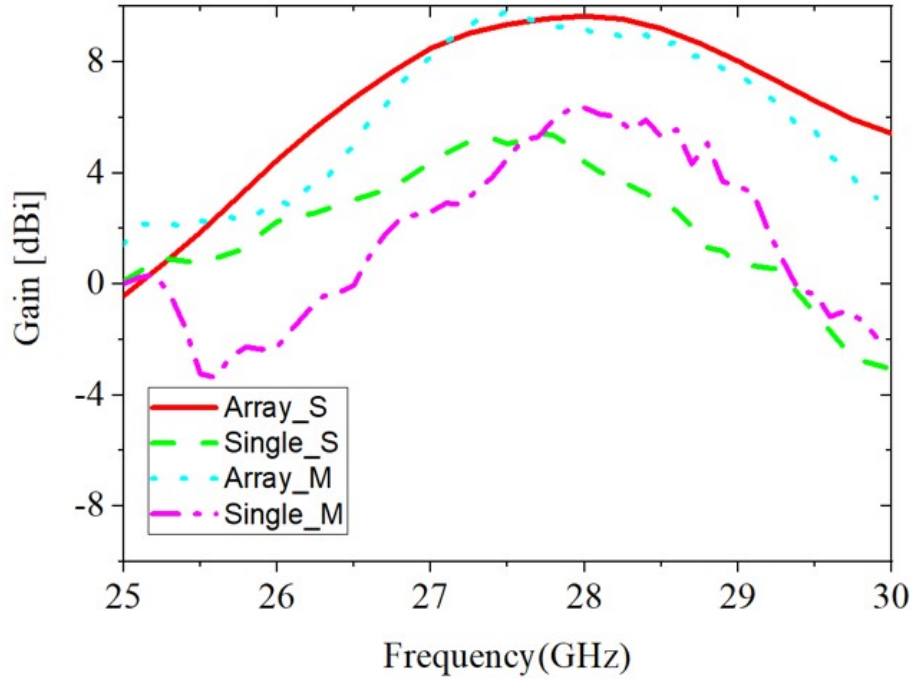Figure 3.22: Realized gain of the Cavity-slot antenna vs frequency
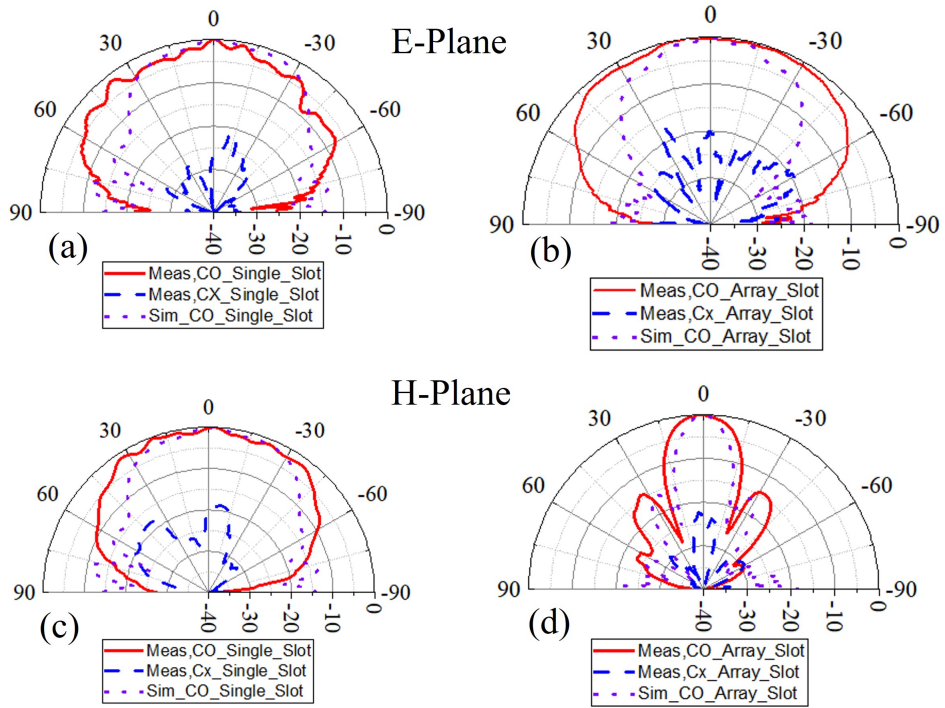
Figure 3.23: Radiation pattern at 28GHz for vertical port. (a) At E-plane (single). (b) At E-plane (Array). (c) At H-plane (Single). (d) At H-plane (Array).

42

ports is achieved in dual-polarized topology. The resultant antenna offers dual-polarized at 28 GHz having impedance bandwidths of 0.94 GHz and 1.65 GHz for single and array elements, respectively. The average gain offered by the proposed antennas over the operating bandwidth is about 5.5 dBi and 9.1 dBi in single and array antennas, respectively.

3.4   Aperture Coupled Antenna

Aperture coupled antenna is explained in [74]. This kind of antenna. compare with other feeding topologies has numerous advantages including non-contacting feed transition and shielding of the feed network from radiating aperture. Using an aperture coupled slot to excite the patch antenna also typically increase the bandwidth beyond the few percent which was obtained by a typical patch antenna. This feature makes an aperture-coupled antenna a good candidate for the ultra-thin substrate to achieve a better bandwidth. Wide bandwidth can be achieved either by using one patch with thicker substrate[75] or by using two or more stacked patches [76]. In this thesis parasitic element is added to the main patch to increase bandwidth and the main patch is excited by a slot shape aperture. In addition, we have used a stripline feed network to make the shielding between the feeding part and the radiation part better. Designing the aperture coupled antenna could be time-consuming and complicated because many design parameters have to be determined in addition to the complex stripline feed network. The effect of the main parameters is discussed below. Moreover, the geometry of the design is shown in Figure 3.24.

Substrate Thickness and Dielectric Constant: Thicker substrate and lower dielectric constant lead to larger bandwidth.

Patch Length and Width: Cross-shaped patch antenna is used in this design. The length of the antenna (PL1) determines the resonance frequency and the width (PW1) mainly deter-

mines the amount of power that is coupled to the parasitic elements. In addition, this width dictates the ratio resonance wavelength between the main patch and the parasitic elements. By dictating the ratio between resonance frequency we mean, it is observed during the tuning that by setting the two lengths close to each other we expected to see two resonances close together. But, this phenomenon would happen only for the specific value of the PW1. Therefore, the width of the main patch determines should select carefully to see these two resonances.

Parasitic element length and width: The length (Para_L1) of the patch antenna determines the second resonance frequency of the antenna. The width (Para_w1) of the parasitic element will be set large enough to have appropriate realized gain due to the length of the parasitic element determining the resonance frequency and we do not have the freedom to make the change on it. So, to have the same gain at the second resonance one should try to have the same radiation area to not see a drop in the gain for the extended bandwidth caused by the second resonance.

Aperture Length and Width: The coupling power from the stripline to the main patch is mainly controlled by the length of the aperture. It is recommended to set the length of the aperture to less than a quarter guided wavelength of the resonance frequency. Longer lengths cause more undesirable back radiation. The width of the aperture also influences the coupling strength, but its effect is less than the length of the aperture. The shape of the coupling aperture has a remarkable effect on the strength of coupling between the stripline and patch. Thin rectangular coupling slots have been used in the majority of aperture coupled microstrip antennas, as these give better coupling than round apertures. Slots with expanded ends, such as dog bone, bow-tie, or H-shaped apertures can further improve coupling. In our design, we have used the H-shape aperture to improve the coupling and bandwidth. It is shown in Figure 3.24(b).

It is obvious that designing an antenna to have the desired performance at 28 GHz is purely
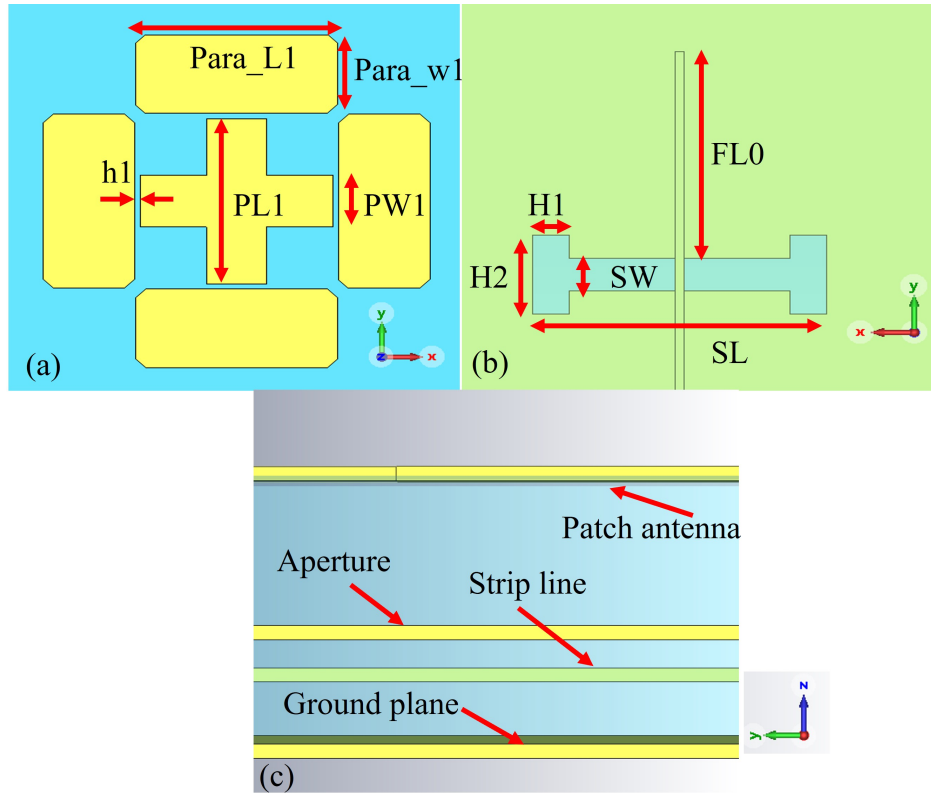
Figure 3.24: (a) Geometry of the proposed aperture coupled antenna. (b) feed line and aperture (c) Side view of the structure

empirical design because of too many strongly related parameters. This design is practically impossible and challenging and we relied on a combination of using software (CST STUDIO SUITE) and basic patch antenna design theory [74] such as fixing the length of patch and parasitic element to resonate near 28 GHz.

In this design, the thickness of the substrate in the feeding line is set to be 87 um and the substrate for the patch is only 125 um thick. Two resonance frequencies are set to be closed together to make the bandwidth more wide-band. As explained before PW1 is chosen to see two resonances near together. Patch and parasitic sizes are initially estimated using simple approximations and then tuned empirically. It is a very tedious method because of the interaction of the parasitic element, main patch, and aperture coupled. The main goal here is to achieve a good bandwidth at the frequency of 28GHz. The radiation area of the

Table 3.4: PARAMETERS OF THE APERTURE COUPLED ANTENNA

PL1	PW1	Para_L1	Para_W1	h1	H1	H2	SW	SL	FL0
2.75 mm	0.925 mm	2.95 mm	1.4 mm	0.1 mm	0.25mm	0.35 mm	0.22 mm	1.3 mm	1.35mm

parasitic element should choose close to the main patch to see the smooth and stable realized gain over the bandwidth. The dimensions of the proposed antenna are summarized in table 3.4. After several tuning, the slot length is found to be 1.3 mm because it gives an input impedance near 50Ω. Moreover, the length of the tuning stub is set to be quarter guided wavelength at the frequency of interest. Figure 3.24(b) shows the details of the aperture in more detail. In this dissertation for the first time, a new method is introduced to increase the bandwidth of the aperture coupled antenna. So far, We have used parasitic elements to increase the bandwidth by introducing a second resonance near the main resonance. But, we can work on the resonance near the aperture slot to increase the bandwidth as well. As shown in Figure 3.25 two lines are added near the main stripline. These two lines add two more resonances near the main one and as a result, increase the bandwidth of the antenna. These two lines detune the amount of the reactive loading of the patch antenna. By several tuning the parameters, the bandwidth of the antenna is increased by around 40% from around 1GHz to 1.4 GHz. Figure 3.26 shows the comparison between the return loss of the two designs. The 1.05 GHz bandwidth was the best we could get by several tuning by only using one feed. Therefore, this method could improve the bandwidth by 40%.

The simulated gain is summarized in Figure 3.27 and improvement in gain is obvious. Here the conclusion is that this method not only improves the bandwidth but also makes the gain figure flatter and smoother. The peak gain for the desired bandwidth is 6.05 dBi for both designs.

The radiation pattern compares in figure 3.28. Both E-plane and H-plane are plotted in this figure and like another conventional patch antenna, the radiation pattern is broadside
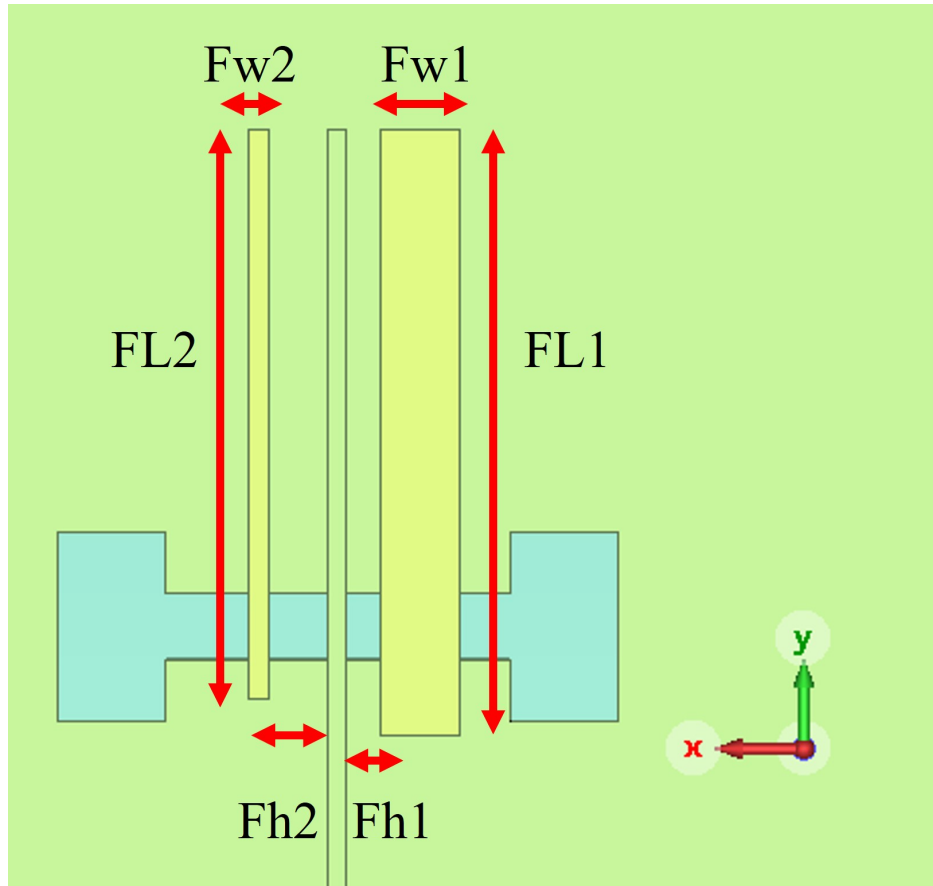
Figure 3.25: (a) Geometry of the proposed aperture coupled antenna. (b) feed line and aperture (c) Side view of the structure

in both designs. The simulated far-field radiation patterns at 28 GHz are shown in Figure 3.28 for both designs. The simulated 3-dB gain-beamwidth is 73°, 65° for the E-plane and H-plane of design_01 and 75°, and 78° for the E-plane and H-plane of design_02, respectively. By aforementioned properties, the proposed aperture coupled patch antenna can be practical in 5G communications in addition to providing flexible properties. In comparing with the previous design we reach the almost same bandwidth but use only 125 um thickness not 202 um thick substrate for the patch. This design also provides better isolation due to shielding the feed line from the radiation part.
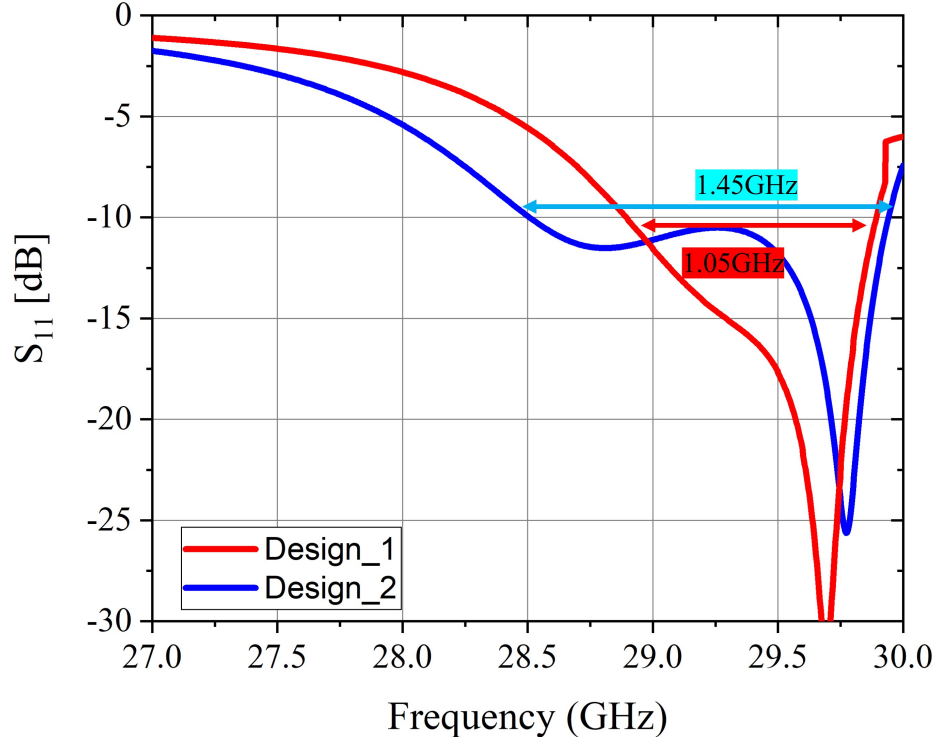
Figure 3.26: Comparison of the S_{11} between Design_01 and Design_02

3.5 Dual-Band Stack Patch Antenna for 5G Applications

In this part, a compact 4×4 dual-band dual-polarized (DBDP) antenna array with a wide bandwidth operating at the Ka-band is presented. A stacked patch topology is used for dual-band operation and feeding probes are used to excite the antenna array. Higher band elements have parasitic patches to achieve higher gain and increase the bandwidth. Moreover, a small metal ground on top of the common ground plane is designed for each element to suppress the coupling between the antenna elements and improve the beam scanning range effectively. The proposed antenna array with the size of $19mm \times 19mm$ operates at the center frequencies of 28 GHz and 38 GHz and the simulated results show that both wide bandwidth and stable gain were achieved. The 10 dB impedance bandwidths are 17.5%
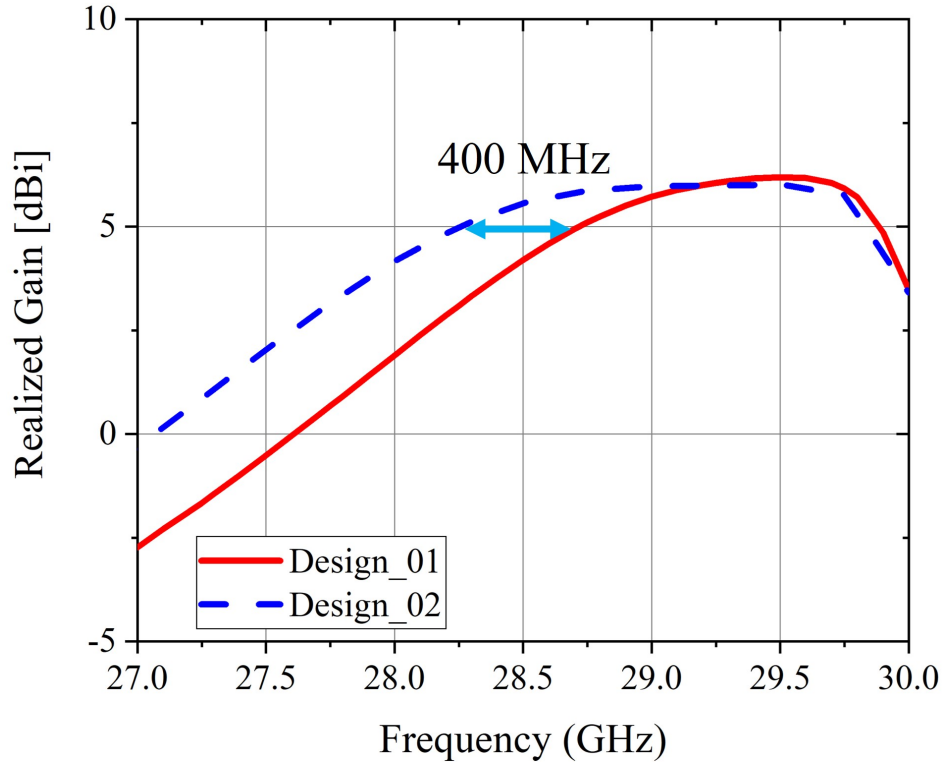
Figure 3.27: Comparison of the realized gain between Design_01 and Design_02
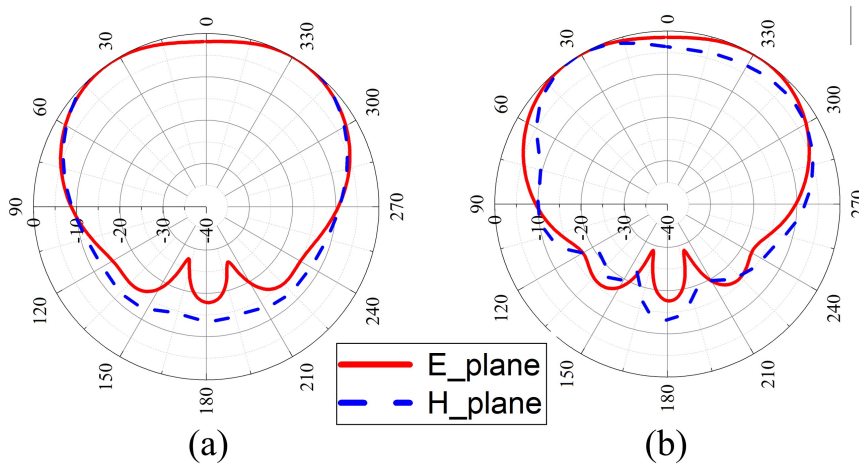
Figure 3.28: Radiation pattern at 28 GHz for (1) Design_01 and (b) Design_02.

and 13.5% in the lower and higher bands, respectively. The realized gain is almost stable over the bandwidth and is around 16.45 dB and 17.28 dB for the lower and higher bands.

Meanwhile, it has a relatively wide scanning angle ranging from -45° to +45° with stable gain and sidelobe level. After successfully develop a dual band antenna with a thick material and make sure this geometry works well we will design same geometry for the ultra thin and flexible material.

Several frequency bands have been made available by the U.S. Federal Communications Commission (FCC) for the incoming 5G communications including the Ka-band at 28 GHz (27.5–28.35 GHz), 37 GHz (37–38.6 GHz), and 39 GHz (38.6–40 GHz). Therefore, the design of a phased array antenna which can operate at multiple frequency bands is needed. This becomes more vital in multi-input multi-output (MIMO) applications when there are several numbers of antennas. In this case, if the phased array antenna is designed with separated radiation apertures for different frequency bands, it occupies a large device area. Thus, designing a phased array antenna with a small footprint, wideband, high efficiency, low cost, and low mass to operate at multiple frequency bands will become a necessity. Moreover, it is more efficient to design a dual-polarized antenna to transmit and receive two orthogonal signals at the same time in the same aperture and be able to prevent polarization mismatch.

The type of design where multiple bands use the same aperture for radiation is called an aperture-shared antenna [77, 78]. It has the advantages of dual-polarization, multi-band element combined design and it is suitable for mobile platform applications. Several shared-aperture antennas with different radiation elements have been reported so far in the literature [79, 80, 81, 82]. The first method of the shared-aperture antenna is the dual-polarized antenna which operates at the same frequency band with orthogonal polarization. For this design, all the elements are usually symmetric, and the feed network is polarized orthogonally [83, 84]. The challenges appear when a dual-band antenna is needed. It is due to the different sizes of the antenna elements and spacing between them, especially when the frequency ratio is large, which means that it occupies a large area.

The second is the inserting method in which the higher band elements are added into one

lower band element and they use the common aperture at the same time. In one of the previous designs, the lower band patch is penetrated in order to put the higher band elements inside it for dual-band shared-aperture applications. The result was 9.7% and 6.73% 10 dB impedance bandwidths for the Ku and X bands respectively. In the other methodology, the radiating elements are interleaved at each band with their shared apertures. In this work, the tri-band dual-polarized aperture-shared array where X-band elements and S-band elements were added in different parts of the L-band array and the results were 14.8%, 13.4% and 16.8% bandwidth for the L-band, S-band, and X-band, respectively. However, additional decoupling networks are usually required to enhance the feeding isolation for this configuration.

The third method in designing an aperture-shared antenna is stacked technology where the higher band element is placed above the lower band element [85, 78] and this method is used in this work. One of the issues of this method is high coupling between the lower and higher bands when operating in the dual-polarized array topology. The other challenge is sharing the same aperture for two separate arrays, operating at two widely separate frequencies without limiting the array scan capability. In this work, a compact dual-polarized dual-band antenna at the center frequencies of the 28GHz and 38 GHz with a stacked technology, high isolation, simple structure, and wide scan ability, is introduced.

3.5.1   Design Concepts of The Antenna

The configuration of a dual-band dual-polarized antenna operating at the Ka-band for 5G applications, is shown in Figure 3.29. For the future 5G application the targeted bandwidth for the dual-band dual-polarized antenna is around 10% at center frequencies of 28 GHz and 38 GHz. The prospective 5G frequency bands are 26.5-29.5 GHz and 37-40 GHz. This design consists of three layers. Substrates 1 and 2 are similar with the thickness of 468 um
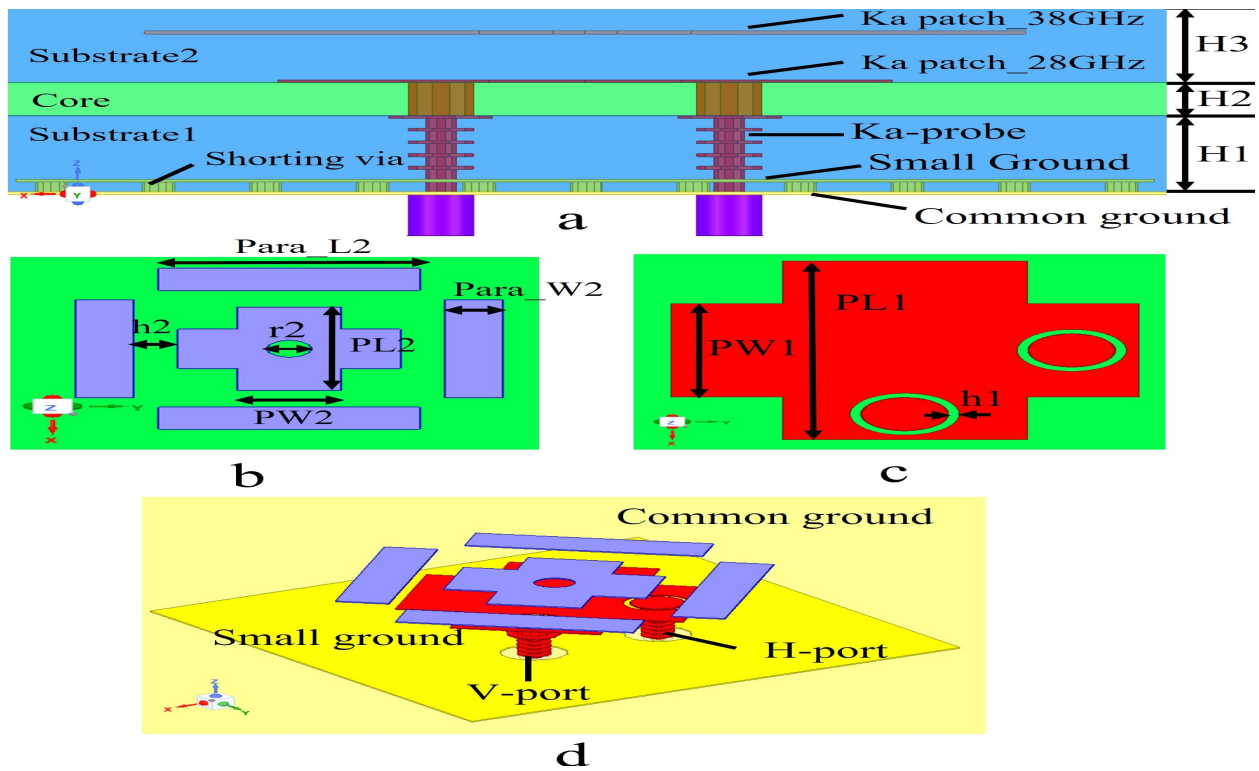
Figure 3.29: layout of the proposed DBDP element. (a) side view. (b) top view of the higher band patch. (c) top view of the lower band patch. (d) Perspective view of the lower band, higher band antenna, common and small ground planes.

Table 3.5: PARAMETERS OF THE PROPOSED ANTENNA [mm]

H1	H2	H3	h1	h2	PL1
468	200	468	0.60	300	2135
PL2	PW1	PW2	Para_L2	Para_W2	r2
1500	1115	700	1765	365	300
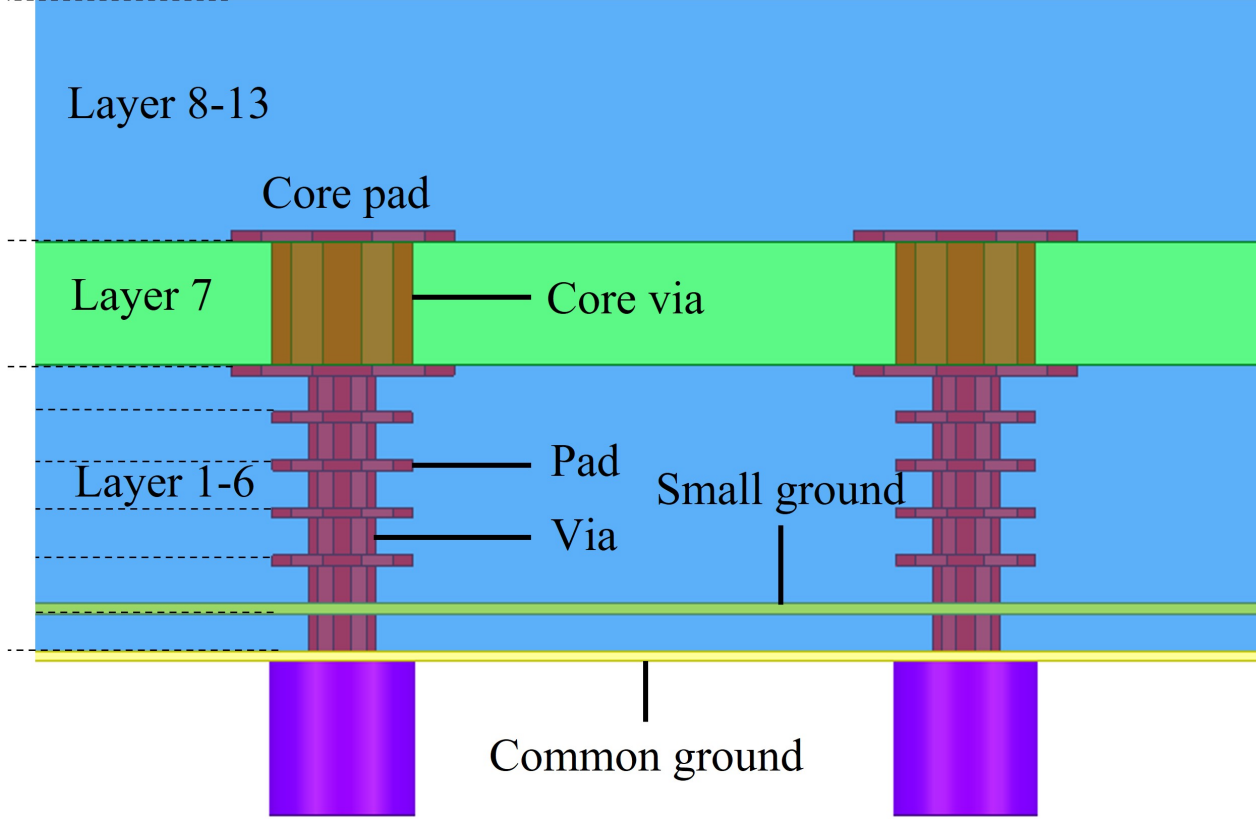
Figure 3.30: Stack-up of the proposed DBDP element.

and a relative permittivity of 3.14, and with a loss of 0.002. The core layer is 200 um thick with relative permittivity of 3.3 and a loss tangent of 0.003. As a result, the total thickness of the antenna is 1.136 mm. The stacked patch antenna configuration is implemented for the dual-band operation and low-profile antenna design.

3.5.2 Single Antenna Element

The radiating elements for the two bands are selected to be a patch. The low band antenna (28 GHz) consists of a driven patch and two capacitive feeds to excite the antenna at two polarizations. The driven patch is placed on top of the core layer as shown in Figure 3.29(c) and fed by two perpendicular probes to achieve dual-polarization (Figure 3.29(a,d)). The high band antenna (38 GHz) is placed inside substrate 2 and above the lower band (Figure 3.29(b)). Moreover, to improve the antenna bandwidth and gain, four parasitic rectangular elements are added in the same layer of the higher patch. These parasitic elements can add a new resonance near the primary patch resonance and as a result, increase the bandwidth. Also, due to the inherent poor isolation of the capacitive feeding, these parasitic elements can improve isolation between the two orthogonal polarizations by reducing the amount of energy leaks to the adjacent element, if the antenna is used for dual-polarization application. This is because if we consider the two ports on the patch as two-separate antennas, the current on one antenna induces a current on the second antenna and leads to mutual coupling based on the reciprocity theorem. The parasitic element here neutralizes the first inter-element coupling. In other words, the current which is directly induced on the second port by the first port is out of phase in comparison to the induced current by the parasitic element and they will cancel each other out.

The dimensions of the patches and parasitic elements can be calculated as follows:

$$f_{L,H} = \frac{c}{2PL_i\sqrt{\epsilon_i}} \ and \ f_{parasitic} = \frac{c}{2Para\_L2\sqrt{\epsilon_2}} \ , \ i = 1,2 \tag{3.4}$$

where c is the speed of the light in the free space. $PL_{1,2}$ and $Para\_L2$ are the lengths of the driven low, high band patch and parasitic patch, respectively. ϵ_1 and ϵ_2 are the effective

dielectric constants for the two antennas. By tuning these lengths, the resonance frequency can be fixed at the desired bands which are 28 GHz and 38 GHz. The antenna is optimized using the ANSYS HFSS software and the optimized parameters are given in the table 3.5.

3.5.3 Probe Feeding and individual ground plane

Figure 3.30. shows the side view of the feeding with more details, where the smaller patch is excited by two probes (Vertical-port and Horizontal-port). The height of the vias in the probe is 60 um and the radius of the vias and its pad is 60 um and 125 um, respectively. Figure 3.29 shows a compact antenna which is achieved by stacking patch antenna and parasitic elements. Another benefit of this design, as shown in Figure 3.29(d), is that each antenna can be isolated from its adjacent elements by a small ground plane on top of the common ground plane. The distance between these two planes is 60 um and they are connected by multiple shorting vias. As a result, cross-talk between components (caused by surface waves) decreases and the scanning performance of the array will get better. However, the electrically long probing causes some mismatch due to excess inductance. To solve this problem, capacitive feeding is used by adding a gap between the probe and the lower band patch. This gap forms the shunt capacitance to compensate for the inductance is formed by a long probe from the ground plane to the substrate 2. As a result, this type of feeding helps to utilize thicker substrates to achieve wider bandwidth.

3.5.4 Single Element Performance

With a proper choice of dimensions for the lower and higher bands patch as well as for the parasitic elements and feeding, a large bandwidth is achieved at both frequency bands. In the final stage, the overall area of the antenna element is $3.8mm \times 3.8mm$. Figure 3.31(a). shows the reflection coefficient of the antenna. In these simulations, the dual-band dual-polarized
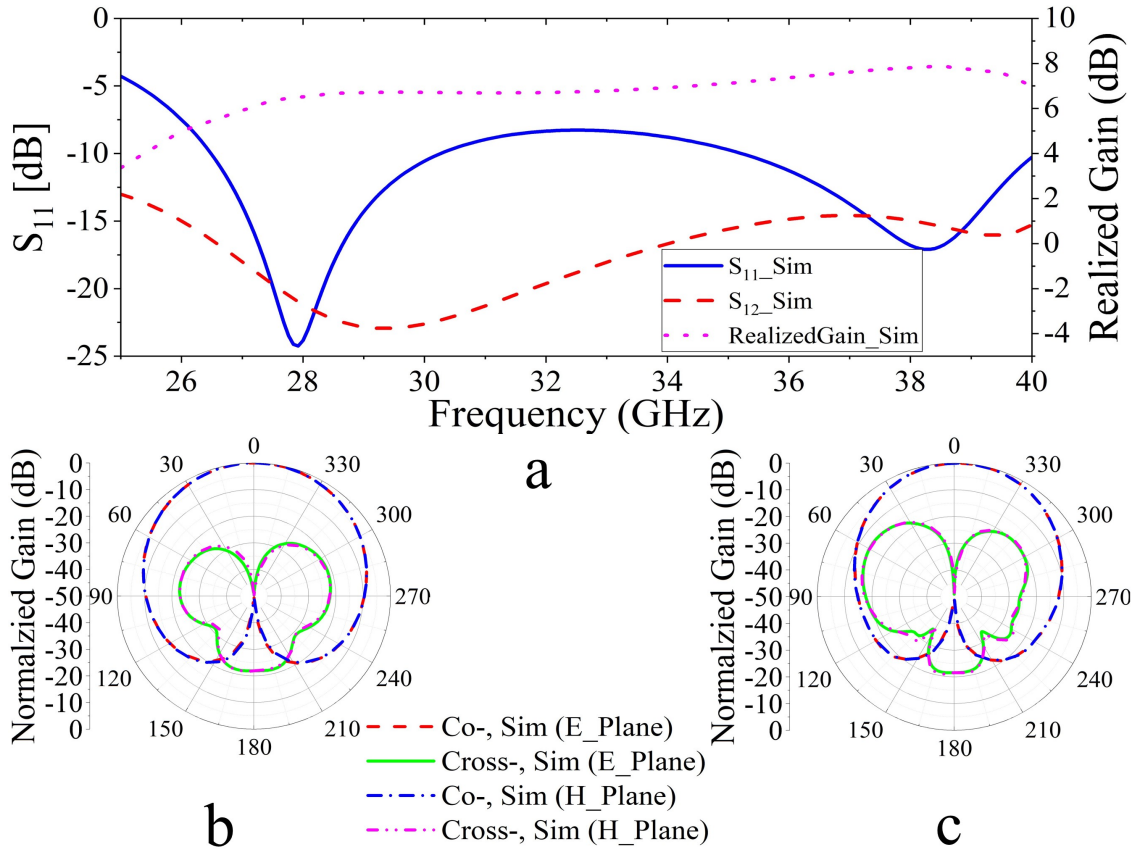
Figure 3.31: (a) S-parameter and realized gain of the proposed single element. Normalized E_plane and H_plane radiation pattern at (b) 28.5 GHz and (c) 38.5 GHz.

antenna shows a -10 dB reflection coefficient with a wide bandwidth at both frequencies. This covers a 3.7 GHz bandwidth from 26.5 GHz to 30.2 GHz and a 4.9 GHz bandwidth from 35.2 GHz to 40.1 GHz for the lower and higher bands, respectively. This bandwidth covers the required frequency bands for the 5G applications in the Ka-band. Moreover, as depicted in Figure 3.31(a) the isolation between two feeds of the dual-polarized antenna is about 20 dB in the lower and about 15 dB in the higher band.

The radiation performance of the single element in both frequency bands is simulated, and it is shown in Figure 3.31(b,c). It can be observed that the antenna exhibits a stable radiation pattern over the bandwidth and with a peak realized gain of 6.5 dB and 7.2 dB for the lower and higher bands as shown in Figure 3.31(a), respectively. According to the Figure 3.31(b,c), the half-power beamwidth of a single element is 71° and 82° for E-plane and H-plane and is 60° and 78° for E- plane and H-plane for the lower and higher bands, respectively.

3.5.5   Antenna Array Performance

The designed single element in the previous section allows making a 4 × 4 antenna patch array at the Ka-band. The antenna should work probably over the whole band to cover the two desired bands which are 28 GHz and 38 GHz. The configuration of Figure 3.32. is used to implement the 4 × 4 array. As it is shown in the figure the antenna elements are rotated 45° with respect to the substrate. This technique results in better isolation and decreases the coupling between adjacent antenna elements when used in an array configuration [86, 87].

To ensure that the phased array antenna has the maximum possible scanning angle without the phenomenon of grating lobes, the required element spacing d can be determined by using:
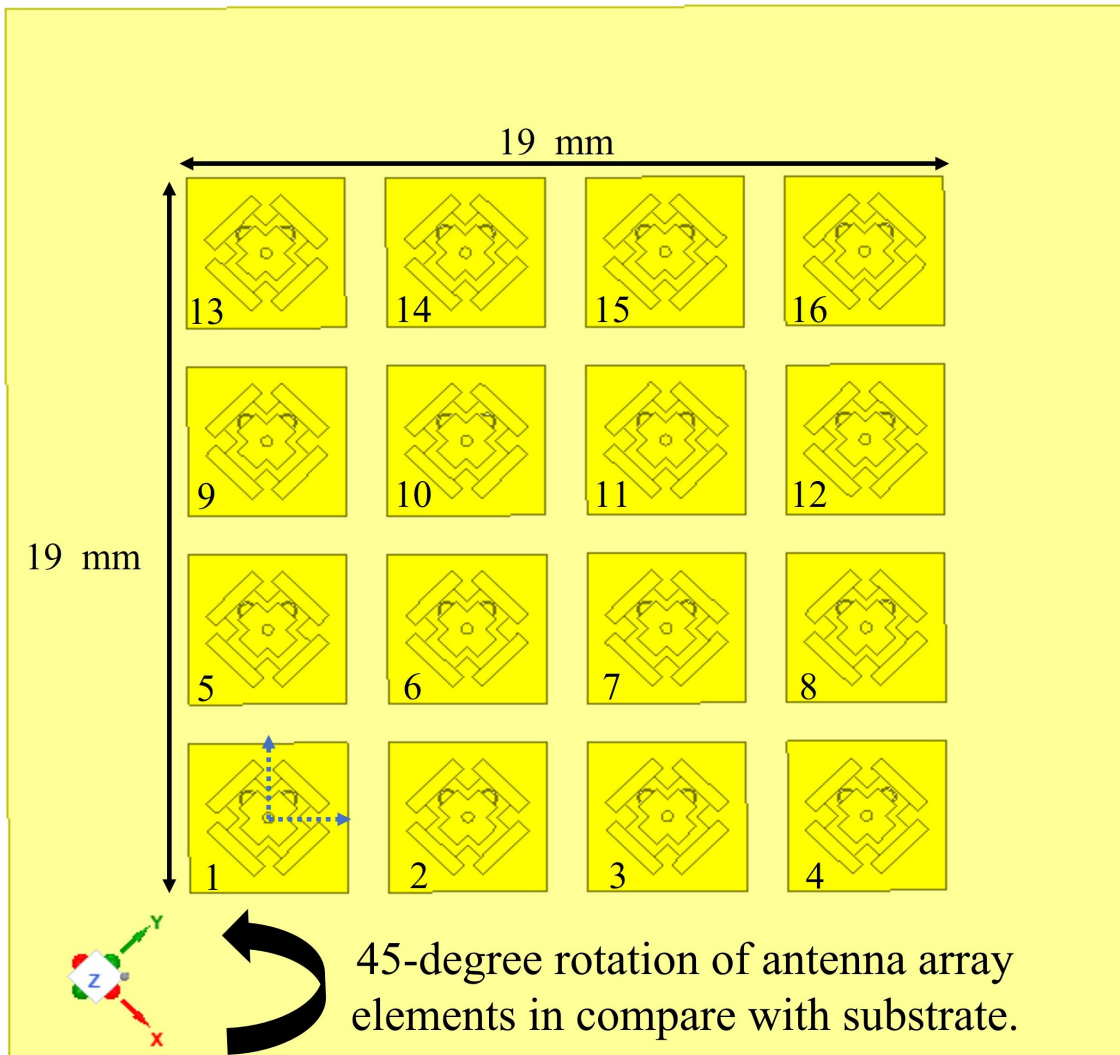
Figure 3.32: Configuration of the proposed antenna array.

Table 3.6: Realized Gain [dB] of the antenna array for different frequencies and scanning angles

Frequency (GHz)	0°	15°	30°	45°
27.5	16.45	16.1	15.6	13.8
28.5	16.46	16.5	15.5	13.8
29.5	16.49	16.6	15.3	13.9
37.5	17.28	15.4	16.5	14.8
38.5	16.8	16.2	16.8	15.5
39.5	17	16.01	16.3	15.4

$$d \leq \frac{\lambda}{1 + |\sin \theta|} \tag{3.5}$$

Here λ is the operation wavelength at 28 GHz and 38 GHz, respectively. θ, the target scanning angle is 45° which is very challenging. Based on equation (2), the element spacing is set to be 4.4 mm due to the maximum element spacing for the lower band is 6.2 mm and for the higher band is 4.8 mm. Therefore, the proposed dual-band and dual-polarized antenna array have the total dimensions of $19mm \times 19mm$. The excitation for the array is the same as for the single element. The probe feeding will be designed on back of the common ground plane. This results in excellent isolation from the radiation pattern side. In this simulation, the antenna array is fed by a lump port with a uniform amplitude excitation.

The realized gain pattern for the array antenna at 28.5 GHz and 38.5 GHz for different scanning angles are shown in Figure 3.33(a,b). This configuration shows a stable radiation pattern over different scanning angles from -45° to +45° for both frequency bands. The maximum realized gain is 16.46 dB and 17.28 dB for the lower band and higher band, respectively. It is also worth mentioning that the maximum gain drops less than 3 dB while scanning in both azimuth and elevation directions for both desired bands. The side lobes are simulated to be as low as 10 dB and 8 dB for the 45° scanning angle at the lower and higher bands, respectively.
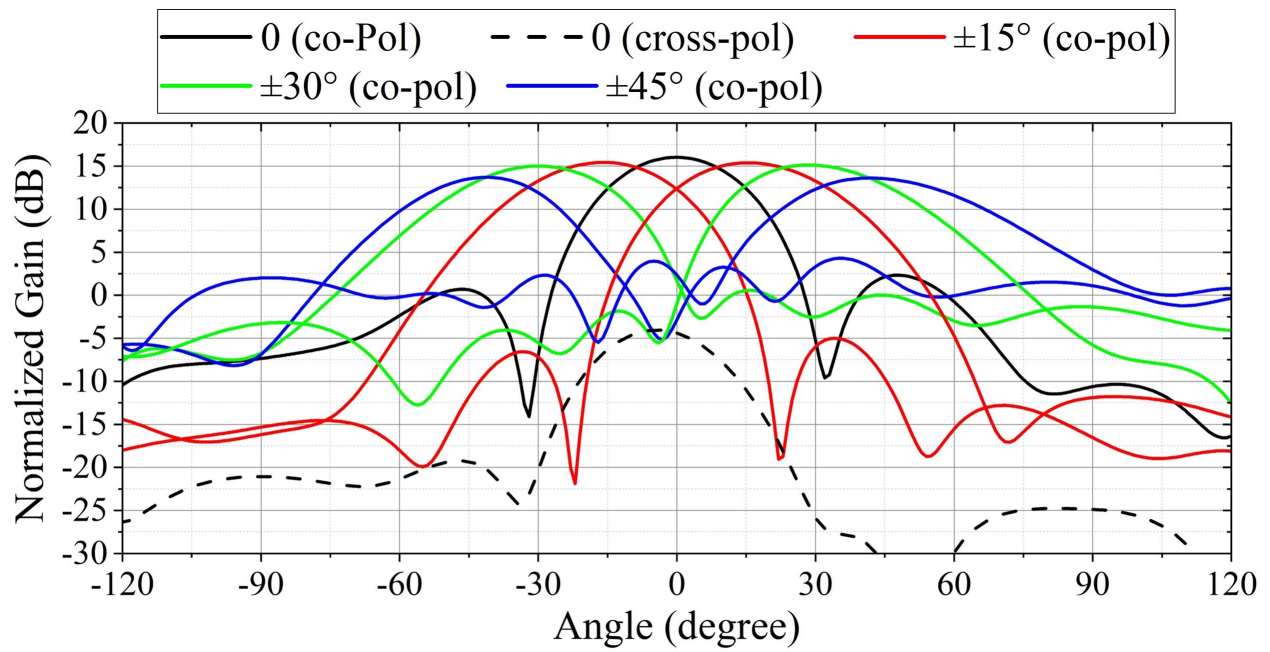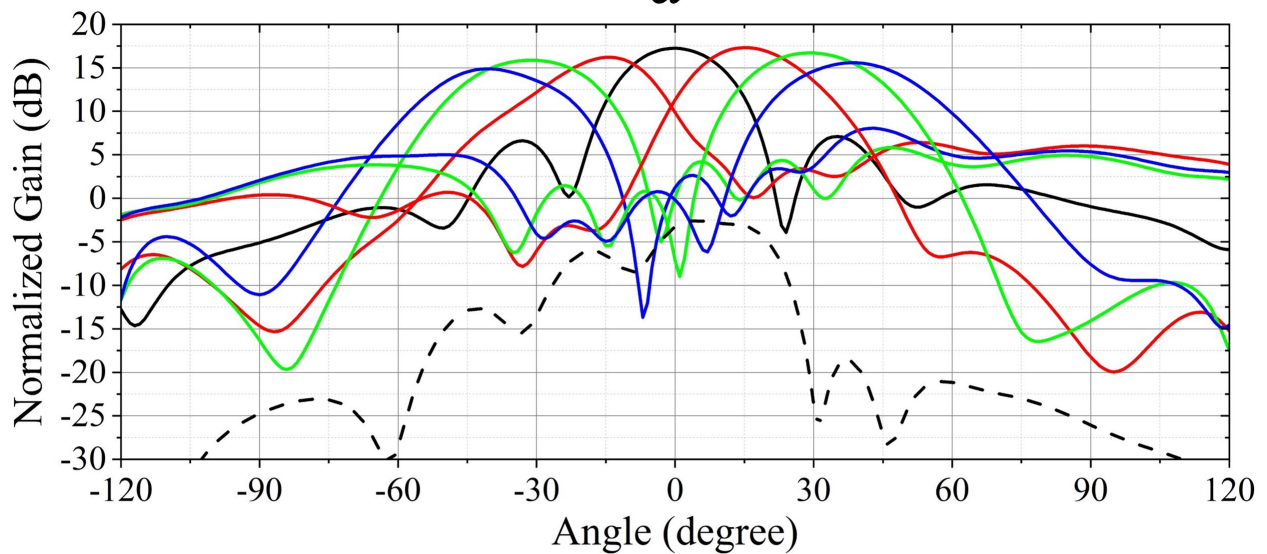
Figure 3.33: Simulated realized gain patterns in E-plane for different scanning angles operating at (a) 28.5 GHz and (b) 38.5 GHz
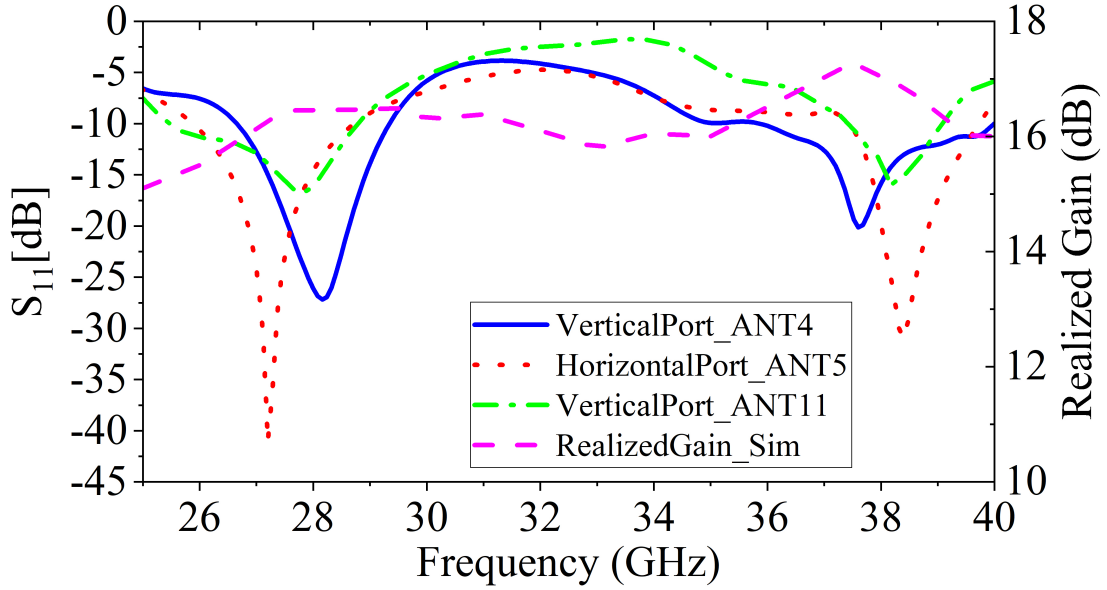
Figure 3.34: The Active Reflection coefficient (ARC) for the the 45° scanning angle (both polarization) and realized gain of the proposed antenna array.

It is also observed that the simulated XPDs are about 21 dB in the broadside direction for both bands. More details of scanning angle and realized gain are shown in the Table 3.6 for six different operation frequencies and different scanning angles. The simulated s-parameter of the three ports of the array antenna is shown in Figure 3.34. The simulated impedance bandwidth (Active S-parameter) ranges from 25.6 GHz to 30.5 GHz and 35.5 GHz to 40.5 GHz for the lower and higher bands, respectively. This bandwidth range corresponds to 17.5% and 13.5% bandwidth at 28 GHz and 38 GHz, respectively. It can be seen that in both E- and H-plane, the 3dB beamwidth of the antenna array is 22°, 21° and 18°, 16° for the lower and higher bands, respectively. Therefore, based on these observations, this antenna array design can be recommended for 5G applications.
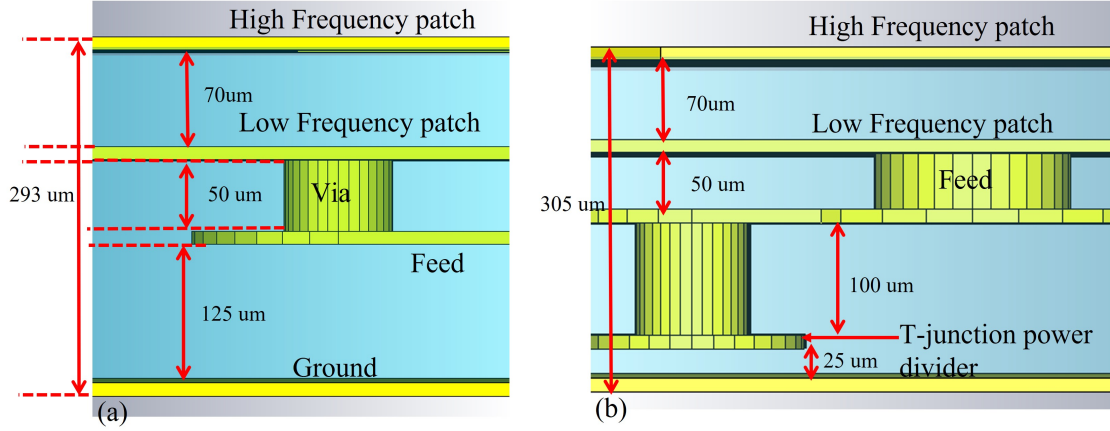
Figure 3.35: layer stack of (a) single element and (b) array element.

Table 3.7: Parameters of the dual band antenna on ultra thin material [mm]

PL1	Para_L1	PW1	Para_W1	h1
3.04	2.9	1.05	1.5	0.15
PL2	Para_L2	PW2	Para_W2	h2
2.55	2.3	1.22	1.15	0.34

3.5.6   Dual Band Antenna on Ultra Thin material

After designing a dual-band antenna on such a thick material we used the same structure to have a dual-band antenna on an ultra-thin material. The proposed antenna is 293 um and 305 um thick for single and array elements. Figure 3.35 shows the layer stack of the single and array element.

The geometry for the patch antenna is introduced which is suitable for a thin substrate and is designed to resonate at 28 GHz and 38 GHz. The geometry of the proposed antenna is depicted in Fig. 3.36. The overall size of the proposed patch antenna, including parasitic elements, is 6.5 mm × 6.5 mm. The optimized value of each parameter in Fig. 3.36 is shown in table 3.7.

A feed network comprised of microstrip lines and a T-junction is used to integrate the patch in a 1×4 linear array. The size of the linear array is 6.5 mm × 25 mm, and element spacing
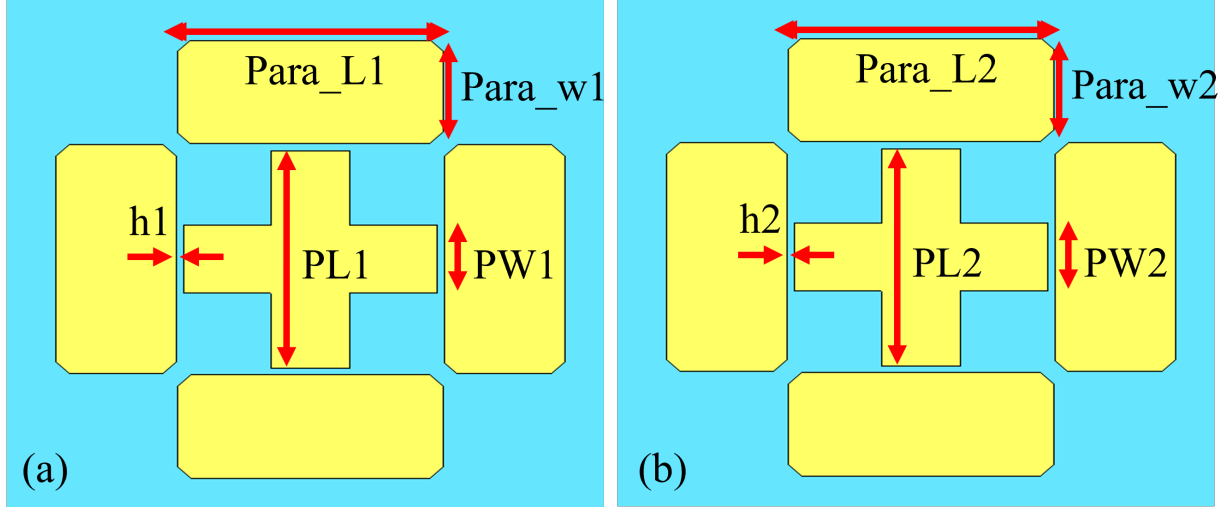
Figure 3.36: Geometry of the (a) single element and (b) array element.

is set to be 6.5 mm. One of the issues with using parasitic elements is that we should make sure the radiation area for both resonances is almost the same to not see a drop in gain. To show this effect two designs are presented here one with a smaller effective aperture for the second resonance and another one with a bigger effective aperture. To increase the effective aperture area we make Para_w1 and Para_w2 bigger in the design that we called Design_2. The S_{11} parameters of the proposed single element and array antenna were simulated and Figures 3.37 and 3.38 show a comparison between the two designs. If we consider S11¡-10 dB as good impedance matching. The single element of the design_2 has a bandwidth of 1.71 GHz, [27.2-28.91 GHz] and 1.27 GHz, [36.35-37.62 GHz] for the lower band and higher band, respectively. The array element has a bandwidth of 2 GHz, [26.6-28.6 GHz] and 1.5 GHz, [36.1-37.6 GHz] for the lower band and higher band, respectively.

The simulated broadside gain over the impedance bandwidth for both design_1 and design_2 are depicted in Figures 3.39 and 3.40. The summary of the gain performance for four different designs (single and array element for design_1 and design_2) is summarized in table 3.8.

Based on Table 3.8 it is obvious that design_1 suffers from a gain drop in the second part of the bandwidth for both low and high bands. This problem is solved in design_2 by improving
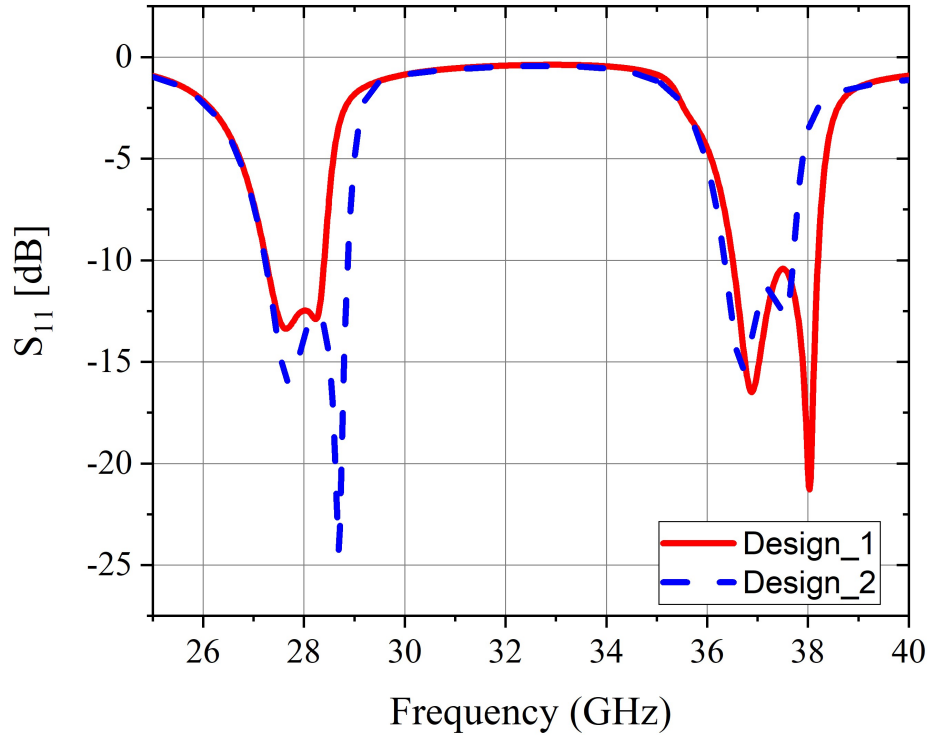
Figure 3.37: Comparison between S_{11} of the single dual band antenna for design_1 and design_2.

Table 3.8: Gain performance of two different designs for single and array elements

| | [Gain over bandwidth [dBi], max gain in bandwidth [dBi] | | | |
	Single (28GHz band)	Single(38 GHz)	array (28GHz band)	Array (38 GHz ban)
Design_!	[5.6 - 2.7], 6	[5.6 - 0.7], 6.2	[10.3 - 2], 11	[9.6 - 4.3], 10.5
Design_2	[6 - 4.1], 6.3	[4.6 - 3.8], 5	[10.6 - 7],11.5	[9.2 - 6.2], 10
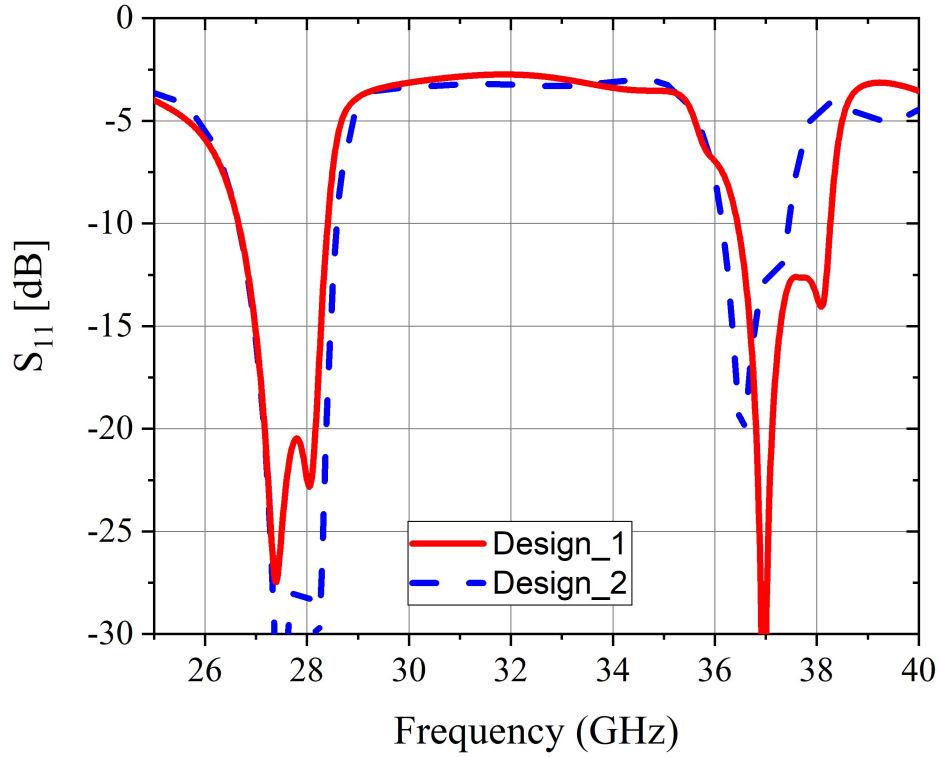
Figure 3.38: Comparison between S_{11} of the array dual band antenna for design_1 and design_2.
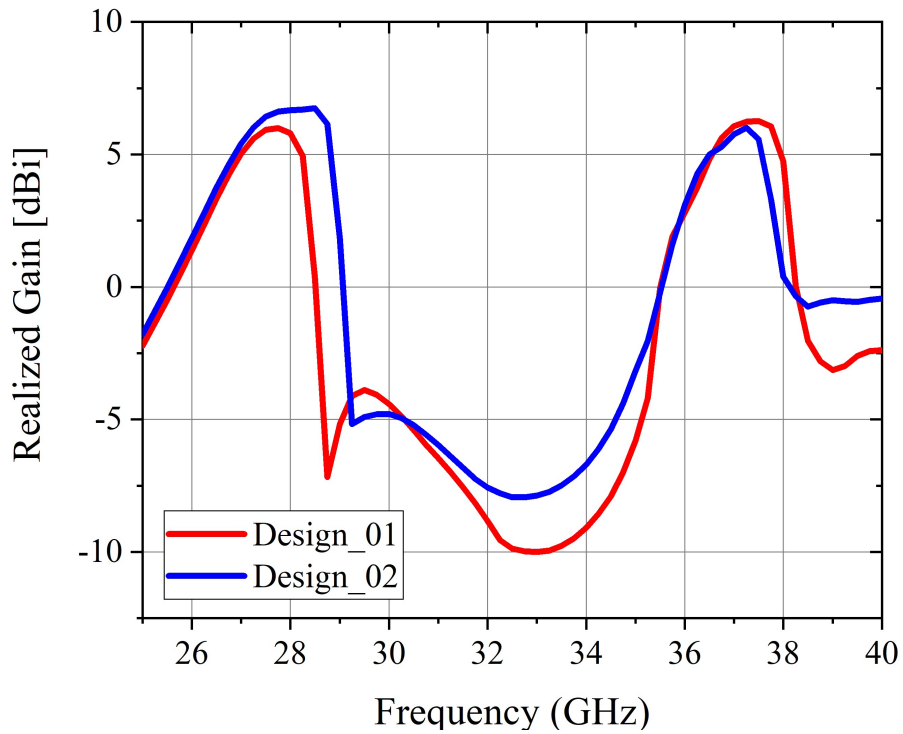
Figure 3.39: Comparison between realized gain of the dual band single antenna for design_1 and design_2.

65
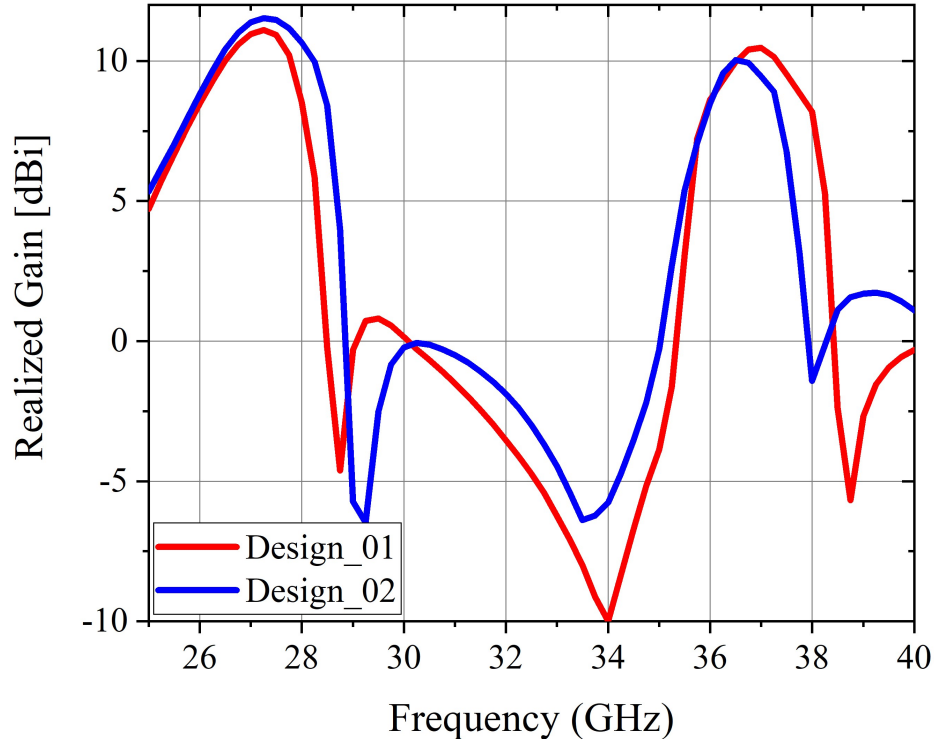
Figure 3.40: Comparison between S_{11} of the dual band array antenna for design_1 and design_2.

the effective radiation area. Gain performance is more stable over the bandwidth in both 28 GHz and 38 GHz bandwidth.

Figures 3.41 and 3.42 show the radiation patterns of the proposed antennas at 28 GHz and 38 GHz. Observe that the cross-polarization levels are around below 20 dB in both E-plane and H-plane for both bands in antenna design_2. The back radiation pattern is also greater than 23 dB for both design and operations bands.

3.6   Summary

In summary, the specifications for all proposed antenna designs in this dissertation are presented in Table. 3.9. The main advantages of these designs are: a) Adequate bandwidth, b) Stable radiation patterns, c) Acceptable realized gain over the designated band, and d)
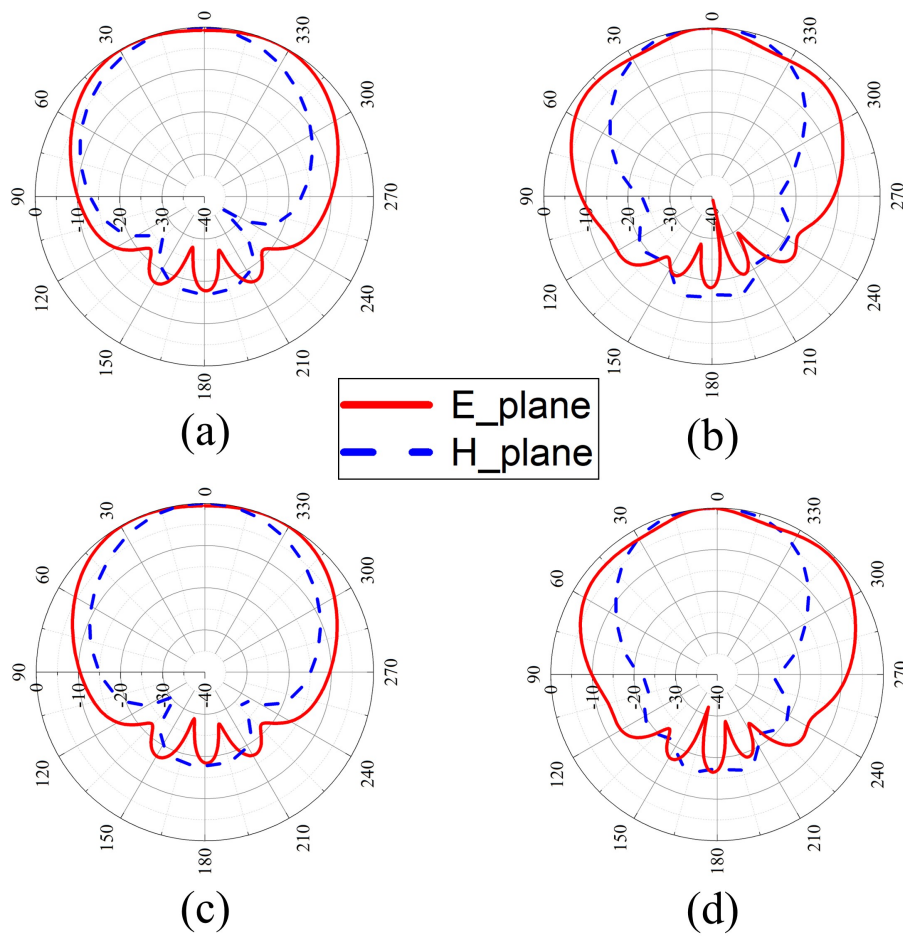
Figure 3.41: Simulated radiation pattern of the single element at (a) 28 GHz design_1. (b) 38 GHz design_1. (c) 28 GHz design_2. (d) 38 GHz design_2.
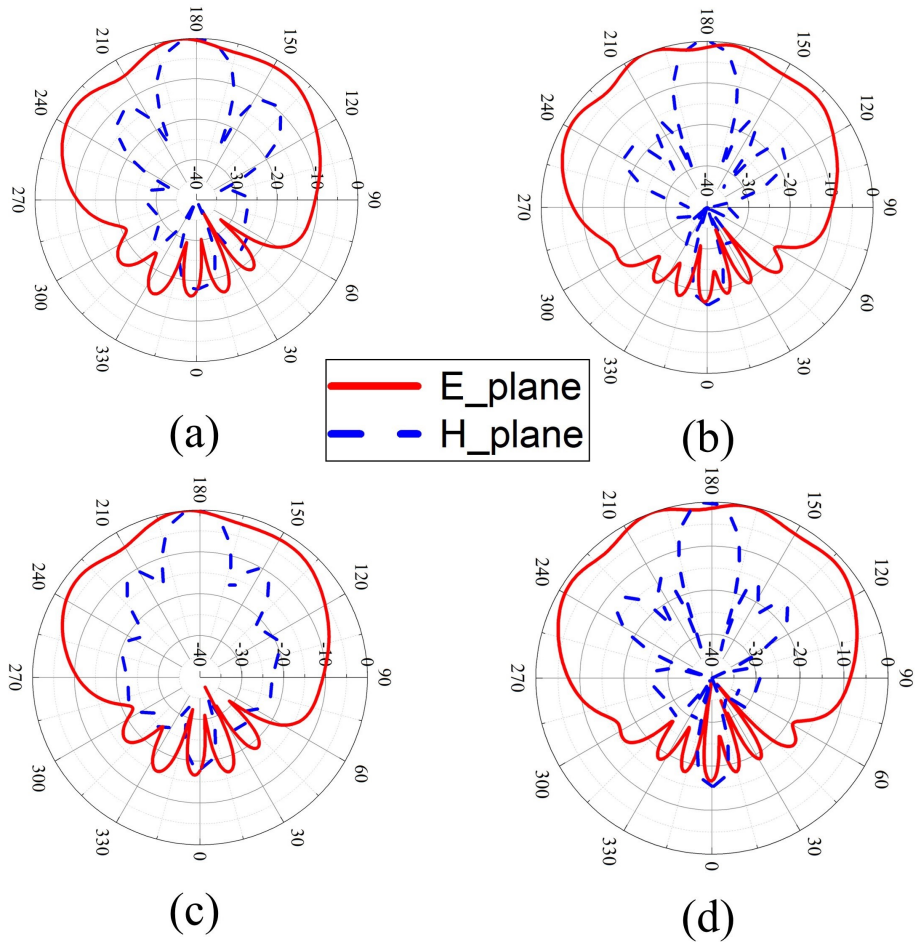
Figure 3.42: Simulated radiation pattern of the array element at (a) 28 GHz design_1. (b) 38 GHz design_1. (c) 28 GHz design_2. (d) 38 GHz design_2.

Table 3.9: Summary of the performance of proposed antennas

	Antenna type	Configuration	Thickness [um]	Bandwidth (GHz) [28GHz]	Bandwidth (GHz) [38GHz]	Average gain [dBi] [28GHz]	Average gain [dBi] [38GHz]
1	Yagi-Uda	Single	120	7	N/A	5.7	N/A
		Array	120	7	N/A	9.7	N/A
2	Yagi-Uda	Single	50	6.1	N/A	5.7	N/A
		Array	50	7.4	N/A	10.3	N/A
3	Single pol patch	Single	202	1.8	N/A	10.2	N/A
		Array	202	2.3	N/A	10.8	N/A
4	Single pol slot	Single	202	1.55	N/A	4.6	N/A
		Array	202	1.7	N/A	10.3	N/A
5	Dual pol patch	Single	202	1.9	N/A	6.5	N/A
		Array	202	2.4	N/A	12.3	N/A
6	Dual pol slot	Single	202	0.95	N/A	5.5	N/A
		Array	202	1.65	N/A	9.1	N/A
7	Aperture couple single pol patch	Single	198	1.4	N/A	5.5	N/A
		Array	N/A	N/A	N/A	N/A	N/A
8	Dual band dual pol patch	Single	1136	3.7	4.9	6.5	7.2
		Array	1136	4.9	5	16.45	17.28
9	Dual band patch	Single	293	1.71	1.27	5.2	4.2
		Array	305	2	1.5	9	8.5

Use of flexible material substrates. Therefore, valuable antenna designs are presented for the next generation of communications.

Chapter 4

Artificial Intelligence in Radio Frequencies

The ubiquitous presence of data-driven technologies that move information from the edge of the Industrial Internet of Things (IIoT) to the cloud for advanced computation and back to the edge for action is pushing wireless connections to the limit. Under these conditions optimizing WIFI Received Signal Strength Intensity (RSSI) can improve data management, computational workflows, and geolocation accuracy while reducing energy consumption to minimize charging and computational resource requirements at the edge. Ensuring connectivity for these mission-critical processes will require detailed knowledge (either measured or simulated) of the state of the electromagnetic fields in advanced manufacturing scenarios. Simulation has the advantage of developing more scalable solutions to this characterization problem but comes at a very high computational cost that may not be possible on edge devices with limited computational resources. In order to reduce the time and resource cost of achieving real-time simulations with low computing specification edge devices, we propose creating a novel method that exploits the notion of information channels to create efficient Convolutional Neural Networks (CNNs) capable of determining the RSSI given a completely

new geometry (never used in training) where objects or obstacles (walls, machines, tables, etc.) and their respective location, size, and reflectivity indices, along with the antenna location are completely random.

4.1 Physics

WIFI is a radio-frequency electromagnetic field. Hence, its coverage and behaviour can be predicted by the Maxwell equations:

$$\nabla \times \mathbf{E} = -\frac{\partial \mathbf{B}}{\partial t} = -i\omega\mathbf{B} \qquad \text{(Faraday equation)} \quad (4.1)$$

$$\nabla \times \mathbf{B} = \mu_0\left(\mathbf{J} + \epsilon_0\frac{\partial \mathbf{E}}{\partial t}\right) = \mu_0(\mathbf{J} + i\omega\mathbf{E}) \qquad \text{(Ampère law)} \quad (4.2)$$

$$\nabla \cdot \mathbf{B} = 0 \qquad \text{(Gauss law)} \quad (4.3)$$

$$\nabla \cdot \mathbf{E} = \frac{\rho}{\epsilon_0} \qquad \text{(Coulomb law)} \quad (4.4)$$

Where $\mathbf{E}$ and $\mathbf{B}$ are the corresponding complex spatial electric and magnetic fields, ρ and $\mathbf{J}$ the electric charge and current densities, ϵ_0 and μ_0 the permittivity and permeability of free space, that are defined as $c = \frac{1}{\sqrt{\epsilon_0\mu_0}}$, where c is the speed of light. ω is the angular frequency defined as $\omega = k \cdot c$, k being the wavenumber. ∇ denotes the 3-dimensional gradient operator, so that $\nabla\cdot$ and $\nabla\times$ denote the divergence and curl operator respectively. Finally, $i = \sqrt{-1}$ is the imaginary unit.

Solutions to these equations come in several forms. Radiation and scattering problems can be approached with modal solutions that are limited to objects whose surfaces can be described by orthogonal curvilinear coordinates. Integral Equation methods that convert the PDE into an integral problem are common and lend themselves to Method of Moments (MOM) solutions. However, if the objects under study have dimensions much larger than the signal

wavelength, these methods can be mathematically troublesome. Methods such as MOM are in the form of infinite series which are imperfectly convergent and are difficult to apply due to the massive computational burden on computer memory and low computational efficiency. There are some techniques to overcome these issues. Classic methods include GO [28] and the geometrical theory of diffraction (GTD), which is originated by [88] and developed by [89, 90] to extend GO by introducing diffraction phenomena. Physical optics (PO) [91] and physical theory of diffraction (PTD) [92] are other methods which can be used to describe these phenomena. GO and GDT are known as ray tracing techniques, while PTD is an extension of PO that applies corrections to PO by considering the effects of diffraction from edges of conducting surfaces.

4.1.1 Governing equations

GO is based on an asymptotic solution of Maxwell's equation for the wavenumber, k. In GO, the power density between two points is controlled by the conservation of the flux of energy in a tube of rays (see Figure 4.1.) In this illustration, a point source at $\mathbf{s} = 0$ is emanating power as an isotropically spherical wave. Within a tube of rays, the cross-sectional areas at some reference point $\mathbf{p} = 0$ and s are given, respectively, by A_0 and A_1. The power density P_0 at $\mathbf{p} = 0$ is related to the power density P_1 at $\mathbf{p} = \mathbf{p}_1$ by

$$P_0(\mathbf{p} = 0) \times A_0 = P_1(\mathbf{p} = \mathbf{p}_1) \times A_1. \tag{4.5}$$

It is assumed that both P_0 and P_1 are constant throughout the cross-sectional areas and no power leaks outside of the conical tube. In the far field zone, the electric field of the electromagnetic wave is related to the power density as:

$$P(r, \Theta, \phi) = \frac{1}{2}\sqrt{\frac{\epsilon}{\omega}}|E(r, \Theta, \phi)^2|. \tag{4.6}$$
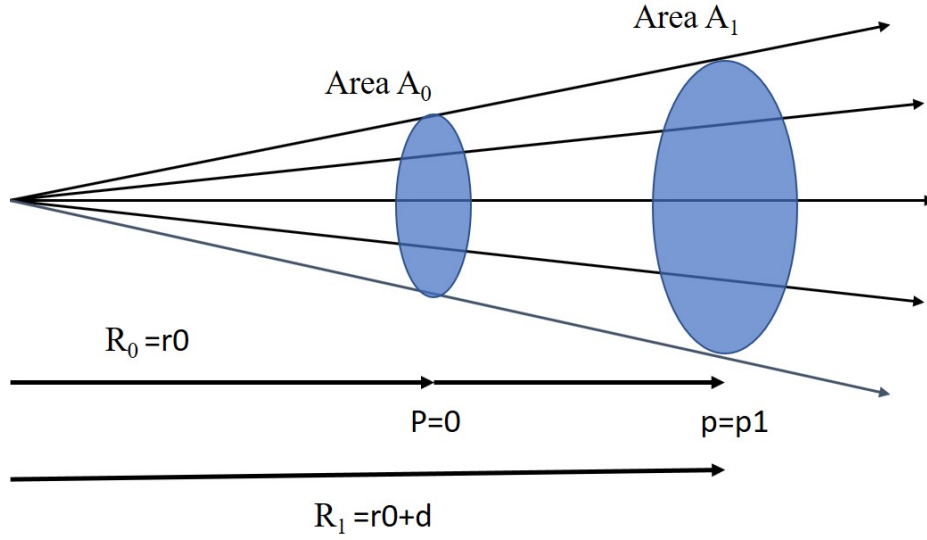
Figure 4.1: Tube of rays for spherical radiated wave.

Therefore, equation 4.5 can be written as

$$\frac{E_0}{E_1} = \sqrt{\frac{A_0}{A_1}}, \tag{4.7}$$

where A_0 and A_1 are spherical surfaces with radius of R_0 and R_1. Thus, equation 4.7 can be written in terms of the radius of curvature of the wave front as:

$$\frac{E_0}{E_1} = \sqrt{\frac{A_0}{A_1}} = \sqrt{\frac{4\pi R_0^2}{4\pi R_1^2}} = \frac{R_0^2}{R_1^2} = \frac{r_0}{r_0 + d} \tag{4.8}$$

GO is a robust approach for analyzing geometries whose dimensions are much larger than the radiation wavelength but has certain limitations for high-frequency diffraction problems. Diffraction occurs when incident rays hit edges, corners, or vertices of boundary surfaces. GO cannot predict the energy which is diffracted when the surface has edges or corners and is unable to account for the energy diffracted into the shadow area when the incident wave is tangent to the surface. Here, GTD comes to account and a diffraction term is incorporated into the solution of GO, as shown in figure 4.1.

Even though GTD overcomes deficiencies in GO in that it accounts for diffraction phenomena, it is important to note that GTD also fails near shadow boundaries, caustics, and foci. To overcome such issues PO is applied. The PO approximation is widely used (since 1912) in the analysis of antennas and scattering problems for electromagnetic and acoustic waves [91]. Since then, it has become a reliable tool in the analysis of electromagnetic problems in which objects' dimensions are large compared to the wavelength. The basic idea is that the incident wave creates a surface current $\vec{J}$ on perfectly conducting objects as equation 4.9 shows,

$$\vec{J} = 2n \times \vec{H}, \tag{4.9}$$

where $\vec{H}$ is the magnetic field of the incident wave. By knowing the current on the conductive surface, scattered fields can easily be found [28]. Thus, PO is a good approximation for large plates. As stated before, PO provides a correct asymptotic description for the field near shadow boundaries, caustics, and foci of GO rays. As noted before, PTD extends applicability of PO by correcting for the effects of diffraction at the edges of conducting surfaces.

4.1.2 Electromagnetic Simulation

Running electromagnetic wave simulations is computationally demanding. Numerous commercial software apply a full wave method that yield accurate results even in complicated electromagnetic problems. However, they also require elevated computational resources and it very quickly becomes time-consuming and challenging to apply these techniques to objects with dimensions larger than many wavelengths including the problem presented in this paper

(a room with $20m \times 20m \times 4m$).

In this paper standard 2.4GHz WIFI band with a 15 cm wavelength is assumed. Full wave packages generate adaptive meshes at the subwavelength scale to solve the 3D Maxwell equations. By comparing the room size to the operating wavelength, it is clear that the solver must manage huge 3D matrices. For demonstration purposes, the same problem proposed for this study was also solved by a full-wave method and required more than 24 hours to solve a single geometry on reasonably provisioned desk-side scientific workstations. Thus, it is not affordable to use this technique to generate enough data to feed a NN, where thousands of simulations are required.

In this paper we will use the ray tracing methods (GO and GTD) as well as PO and PTD to simulate the defined problem and to deliver maximum accuracy for large-scale problems. By using this techniques, 2000 different geometries were simulated in less than 24h.

4.2 Applying Machine Learning: Neural Networks

NNs enhance computer intelligence in many different fields, such as computer vision, natural language processing, data mining, etc.and with the recent breakthroughs in deep architected NNs, they are being broadly deployed across essentially all scientific and engineering fields. Their utility is based upon many useful properties which, for our application, include computational efficiency and code simplification. Instead of solving the complicated PDEs of Maxwell (as described in the previous section) with unique Initial Conditions (IC) and Boundary Conditions (BC) for each geometry, we trained a NN model to learn the relative spatial relationships between the WIFI antenna and the objects in order to predict the RSSI in the whole space; which as we will show, significantly reduces the computational effort and simlifies the code to the point that it can efficiently run on edge devices like a Raspberry PI.

| Simulation (Target) | Dielectric Constant Input Layer | Distance Input Layer | Angle Input Layer | Integration Input Layer |
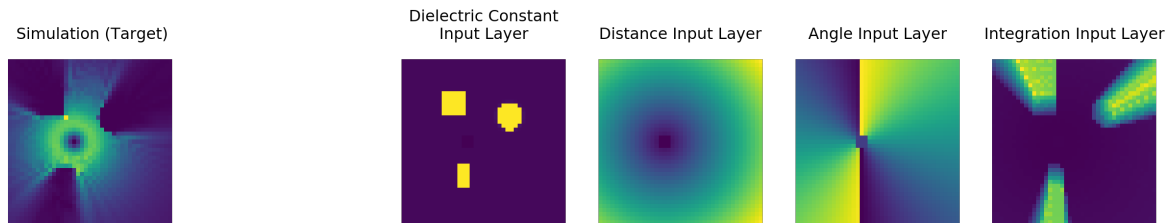
Figure 4.2: A visual example of simulation results and a comparison with the model input layers.

There are two major categories of architectures for NN: Convolutional Neural Networks (CNN) and Recurrent Neural Networks (RNN). Recently CNNs have been widely used in visual recognition by learning features from the distribution of an image's digital representation in pixels. Spatial and temporal relationships of pixels are learned by the CNN and stored in the model weights and biases during the training process. In this paper, we will focus on CNN structure since the spatial features of the environmental layout play a critical role in solving physical models. The CNN is a special design of Feedforward Neural Network which have been shown to be capable of approximating any measurable functions to any expected accuracy [93].

4.2.1 Pre-process and Integration Path

Our CNN model considers the locations and material properties of objects, as well as antenna locations and emitting power as the primary source of information. A naive approach would be to feed these raw parameters (which are used in the numerical PDE simulations) into the simulation as an ordered one-dimensional input array to the CNN. However, this approach lacks information about the connectivity of this data (e.g. nodal connectivity of the mesh) which prevents the CNN from capturing localized information (which is critical to efficient learning) about the WIFI signal correlations among neighboring locations in the boundary environment. Instead, we incorporated those parameters into a two-dimensional matrix - a geospatial map, where each index in the matrix stands for the geo-location coordinates
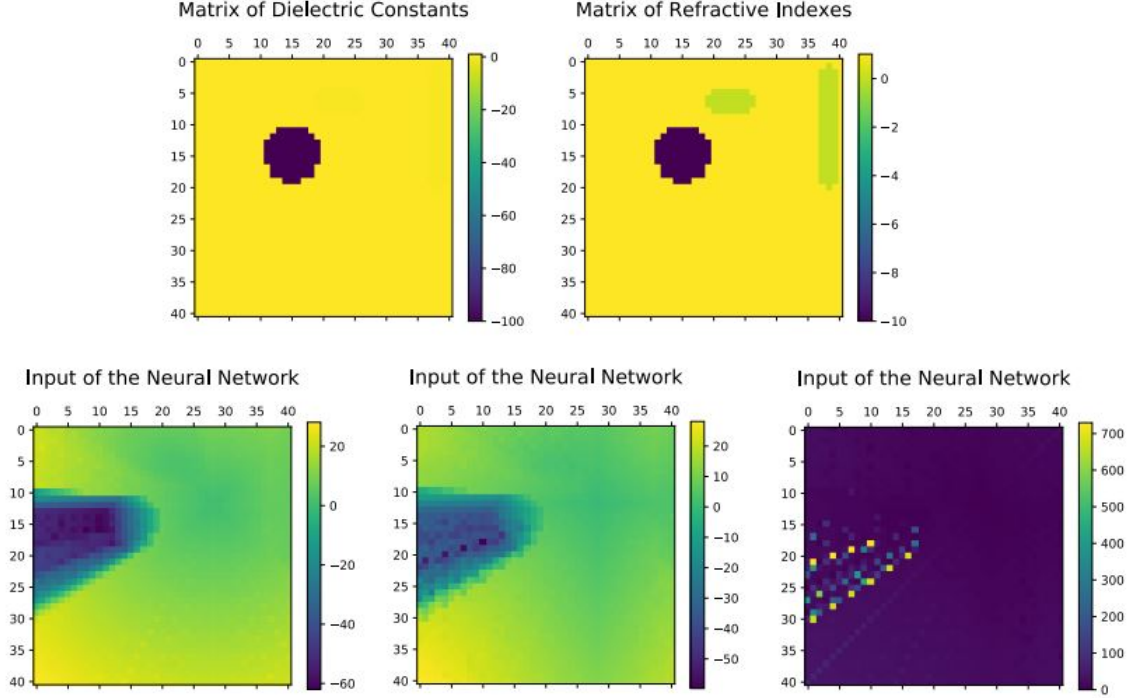
Figure 4.3: Top row: typical Physics information-channel inputs. Bottom row: typical Integration Path information-channel inputs (Linear, Exponential & Complex Filters respectively)

of the map, and each entry represents the corresponding object identity (e.g. antenna / obstacles) and its property (e.g. emitting power / dielectric constant). With the increased two-dimensional input layer, neighboring signal patterns are better accounted for through the kernels of the convolutional layers of the CNN model.

Pre-processing the data to reduce training time has been extensively studied [94, 95, 96]. In this study, the approach is to extract key features from the data in order to reduce the required amount of data that must be input to the NN. Ours differs in that we exploit the existing knowledge of influential factors in the distribution of electromagnetic signals to extend the input data in the following four two-dimensional information-channels:

- **Physics information-channel**. This channel incorporates the essential information needed to describe the physics of the problem (e.g the IC that a numerical PDE simulation would initially require) such as location of the antenna and objects. Importantly

it differentiates the localized material properties (e.g. dialectric constant) of objects in the geospatial map.

- **Geometric information-channel (Distance)**. Computes the distance between the antenna and the objects.

- **Geometric information-channel (Angle)**. Computes the plane angles between the antenna and the objects.

- **Integration Path information-channel**. Exploits known electromagnetic features to integrate an approximation of a Wave Function along the path from the objects to the antenna.

A simplified version of this approach can be seen in [97], where the authors use a Geometric information-channel, based only on the distance, to solve the Poisson equation. The broader implementation of information channels into a four dimensional perspective described above is novel to the approach that we present here-in.

The dielectric constant layer within the physics information-channel represents the Dirichlet BC. The distance layer within the geometric information-channel combined with the elements of the integration path information-channel provides the notion of dissipation, while the angle layer within the geometric information-channel combined with elements of the integration path information-channel captures the angle of the ray hitting against the objects, helping to predict the reflection component (based on the GO approach). The distance and angle layers of the geometric information-channel also provide information regarding the connectivity of the physical objects within the field to improve the networks access to local information during training. Neumann BC are assumed at the walls to account for the WiFi signal escaping the enclosed room under study.

An illustration of each input layer is shown in figure 4.2. As can be noticed from this

example, the dielectric constant layer (i.e. physics information channel) distinctly indicates the locations of the objects in the bounded environment and the integration path channel provides information about the signal propagation path.

Integration Path information-channel filters

A purposeful radial integration path filter can be designed so that it takes into account some of the following electromagnetic phenomena: (1) The linear relationship between the distance and the refractive index; (2) The reflection and transmission at the interface of different materials along the straight ray's path from the antenna to the object; (3) The power decay reciprocal with the distance from the antenna; and (4) The complex nature of the refractive index and of the phasor.

These filters integrate frequency-asymptotic approximations of the decaying wave equation along the straight path from the antenna to every point of the mesh, ordered in increasing computational effort:

- **The Linear Filter** describes the linear relationship between the refractive index and the distance, such as

$$F_l = \sum_s n_s d_s, \tag{4.10}$$

  where the sub-index s indicates the cell of the mesh with refractive index n_s and length of the ray crossing the cell d_s.

- **The Exponential Filter** takes into account the reciprocal power decay with respect to the distance from the antenna but neglects the importance of reflection and of the

oscillatory nature of the solutions. The Exponential Filter function reads

$$F_e = \sum_s n_s \frac{d_s}{\ln(d_s)} + n_{s+1} \frac{d_{s+1} - d_s}{\ln(d_{s+1} - d_s)}. \tag{4.11}$$

- **The Complex Filter** describes the best approximation to the radial solution of a Dipole Antenna by taking into account all the previously listed phenomena. The Complex Filter reads

$$F_c = \sum_s t_{s-1} \frac{e^{jn_s d_s}}{d_s} + r_s \frac{e^{-jn_s d_s}}{d_{s+1} - d_s}, \tag{4.12}$$

where $t_{s-1} = \frac{2n_s}{n_s + n_{s-1}}$ and $r_s = \frac{n_{s+1} - n_s}{n_{s+1} + n_s}$ stand as the transmission and reflection coefficients.

A graphic comparison between the impact of these filters can be seen in figure 4.3, where they are applied to the same matrix of dielectric constants.

A similar approach to utilization of these information-channel filters is described by [51]. In both approaches, the main idea is that physics equations have a higher relevance during the generation of the black-box process of weight generation during the training phase. However, whereas the the physics-informed NNs work on the space of the inner layer weights, for the presented case the information-channel filters are included as part of the input. Although the effect of the physics equations on the weights is probably lower in the information-channel approach, this becomes a more resilient option, that can be directly applied to any kind of ML architecture and hence to more diverse problems. In
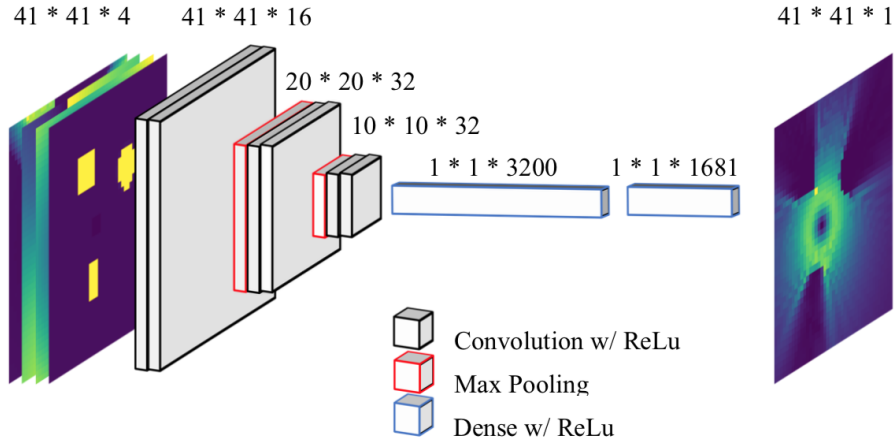
Figure 4.4: The proposed CNN model Architecture is comprised of a four channel 2D input, 5 inner layers (3 convolutional plus 2 fully connected layers) and a 2D heat-map shape output.

4.2.2 CNN Architecture

Existing deep CNN models have shown high accuracy and efficiency in imaging classification tasks. Some of the most common approaches are

- VGGNet [98],

- GoogLeNet [99],

- ResNet [100].

The CNN model presented in this paper is designed to predict the WIFI RSSI in a whole geo-space given the pre-processed information-channel map. Although the target problem differs in nature, inspired by the deep NN architectures, we propose a relatively shallow but efficient (i.e. reduced training effort), scaled to simulation size CNN model, as described in figure 4.4.

The model first consists of several stacked convolutional and max-pooling layers, which help to extend the initial four input layers into a larger latent feature space, capturing more

81

complex inter-relationships between signals from different locations. The latent feature layers are then flattened into a one-dimensional array, connected by dense layers, and eventually reshaped into the numerical PDE simulation generated signal map. With the proposed architecture, the WIFI RSSI distribution prediction is obtained as a 41×41 by $2D$ image.

The weights within each layer are updated during training to minimize a loss function that represents the approximation error at each epoch. The simplest loss function is the Mean Square Error (MSE). With N being the total number of training sets, MSE reads

$$MSE = \sum_{i=1}^{N} \frac{(y_{true}^i - y_{pred}^i)^2}{N}, \tag{4.13}$$

where superscript i is the i-th training set and y_{true} and y_{pred} represent the target value and the one predicted by the CNN, respectively.

Because different geometries can easily produce different distributions and thus maximum values that can skew results, a Normalized Mean Squared Error (NMSE) is considered by

$$NMSE = \frac{MSE}{\sigma^2}, \tag{4.14}$$

where σ is the standard deviation. Thus, the NMSE can be written as

$$NMSE = \frac{\sum_{i=1}^{N} (y_{true}^i - y_{pred}^i)^2}{\sum (y_{true}^i - \hat{y}_{true}^i)^2}, \tag{4.15}$$

where $\hat{y}_{true} = \frac{\sum_{i=1}^{N} y_{true}^i}{N}$ is the mean true value.

There exist other expressions to normalize the MSE, such as dividing by the mean, by the difference between maximum and minimum, or by the quarterlies (when the sample has few extreme values). In most scenarios the extreme value is given by the power of the antenna and only when the antenna is close to a reflective surface might a slightly higher

value be obtained. Therefore, normalizing by the standard deviation can be considered a logical option [101, 102]. As the training data distribution can significantly vary because of different geometries (i.e., higher or lower refraction and reflections), for our purposes we consider the NMSE as the most effective loss function. Unlike Mean Squared Error (MSE) shown in equation 4.13, the NMSE normalizes the variance of the incoming data, thus removing possible bias.

For validation, we use the Coefficient of Determination R^2, described as

$$R^2 = 1 - \frac{\sum (y_{true} - y_{pred})^2}{\sum (y_{true} - \hat{y}_{true})^2}.$$
(4.16)

Once the CNN is trained, a completely new simulation can be generated by using the boundary environment from the pre-processed data input plus the coordinates of the antenna location.

4.3 Scientific Workflow

One of the main goals of this paper is to demonstrate that WIFI RSSI simulations can be solved in real time using the edge computing resources characterized by low specification, low cost computing systems typically found in IIoT deployments (e.g. Raspberry Pi scale). In these settings it becomes important to have actionable intelligence that can be deployed to take effective action for improving process outcomes, either by an automated system or by a human in the loop. To accomplish this we are proposing that the computational effort needed to produce training data be done with cloud based high spec (e.g high performance clusters) equipment, initial model training is conducted in the cloud for pre-processing the weights and biases of a phenomena (in our case electromagnetic wave propagation) and deploy the resulting algorithm (i.e CNN) for rapid computation (and adaptive training) at

the edge (in this scenario, Raspberry Pi class computation).

In Machine Learning (ML), three stages are typically defined to build the final model: training, testing and validation. For the CNN that is herein described we propose:

- Acquire training data and fit the model [103] by computing the weights that connect neurons of different layers;

- Segment an independent data set from the training set that follows the same probability distribution to test the precision of the NN; and

- Segment data (validation) from the training set to validate convergence while the network parameters (weights and biases) are adjusted during training.

Generating simulated data and training the NN will require more computational time with higher specification computing, but needs only to be done once. Once the NN is properly trained and achieves the desired accuracy, it can be exported to other computational environments to solve complex problems (which can include adaptive training to incorporate site specific features from sensor acquired data) in low specification computational systems typically found at the edge of the IIoT. The workflow for creating, training and refining these CNNs is shown in figure 4.5. This schematic workflow was implemented with a Kepler scientific workflow [104, 105] to automate the creation of the PINNs that we describe in this paper.

This workflow is generic for any kind of NN that is trained with synthetic data (i.e. generated via simulations.) Herein, the choice of boundary conditions (BCs) to incorporate into the synthetic data is a key factor in properly training of the NN. If the various BC's are too dissimilar, training will diverge and if they are too similar (i.e., oversampling) the NN will not generalize and will represent only very specific scenarios.
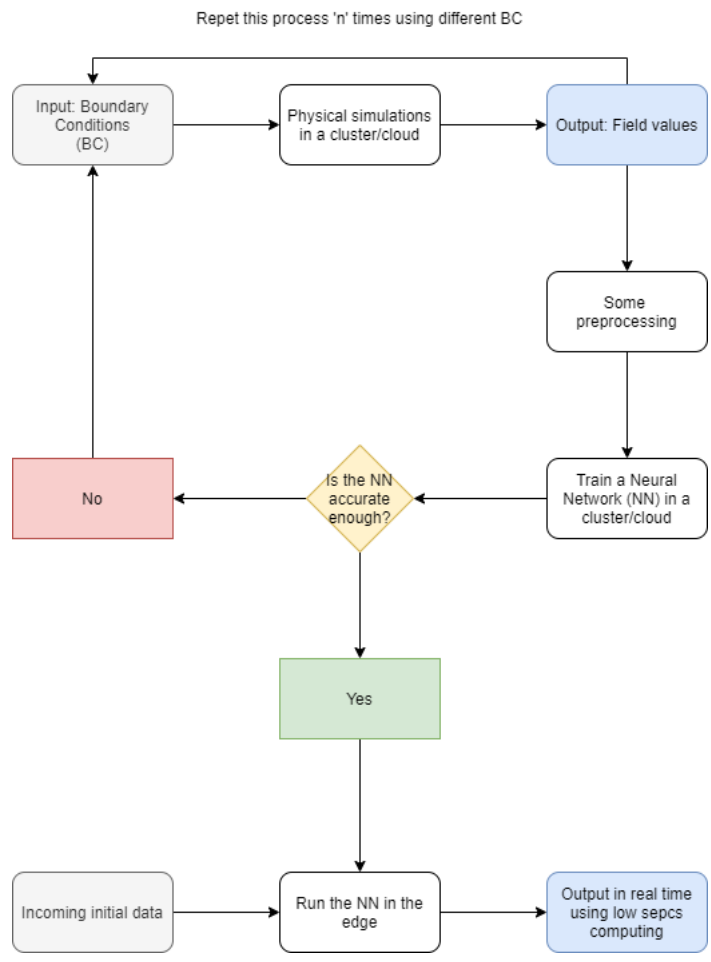
Figure 4.5: Visualization of the required workflow to train and run a NN. Top: Training with synthetic data generated by physical simulations in the cloud or in a cluster. Bottom: Running a trained NN in the edge in real time

However, the generation of synthetic data remains computationally expensive, usually requiring thousand or tens of thousands of physical simulations. In the following subsection a process for generating random geometries and associated BCs that can significantly reduce computational effort and improve NN training is described.

4.3.1 Random Geometry Generation

The geometries used to create the map of dielectric constants are generated randomly. For this purpose, key values (e.g., center, radius and height if it is a cylinder or width, length and height if it is a parallelepiped) for the elements or objects that are part of the geospatial map are randomly allocated. In the case where the gap between objects is too small to neglect channel effects, the objects are overlapped generating a new all-in-one object. The limit of the room is bounded by Neumann BC, and assumed to be a continuum space, in order not to limit the simulations by the size of the room.

With this approach we find that not all cases are represented in the appropriate amount, which translates into reduced training performance. [106, 107]. The imbalanced class problem has also been extensively studied in [108], where it is shown that the training set can be oversampled without regard for over-fitting when utilizing CNNs that generally do not present an over-fitting problem. For our purposes, where a CNN is trained, we are more concerned with reducing training time (and associated computational resources) and therefore using smaller training sets is desirable.

Building upon this idea, the Shannon entropy [109] of every image is measured to ensure the maximum representation of different cases.

The Shannon entropy is a measure of the uncertainty associated with a random variable. Specifically, it quantifies the expected value of the information contained in a message. The

Shannon entropy s of a random variable χ is defined as

$$s(\chi) = s(P_1, ..., P_n) = -\sum_{i=1}^{n} P_i log_2 P_i, \qquad (4.17)$$

$$P_i = Pr(\chi = x_i); \qquad (4.18)$$

with x_i indicating the ith possible value of χ out of n symbols, while P_i denotes the possibility of $\chi = x_i$. This definition can be exported to a digital image. As shown in [110], in an image with MxN pixels, χ denotes a sample from a certain L intensity-scale (normally grey-scale) source. For example, an 8-bit gray image allows $L = 256$ gray scales from 0 to 255. Then,

$$P_l = Pr(\chi = l) = \frac{n_l}{\tau}, \qquad (4.19)$$

where subscript $l \in 0, 1, ..., L - 1$, n_l is the intensity scale and $\tau = MxN$ is the total number of pixels. Thus, the Shannon entropy of an image becomes

$$s_{image}(\chi) = -\sum_{l=1}^{L-1} P_l log_2 P_l = \sum_{l=0}^{L-1} \frac{n_l}{\tau} log_2 \frac{\tau}{n_l}, \qquad (4.20)$$

herein, the maximum Shannon entropy is given when each symbol is uniformly distributed.

Although this calculation could be done by using the gray-scale image of every geometry within its dielectric constant values, we only consider two options: air (equivalent to 0) and object (equivalent to 1). By doing this, only the geo-spatial position is taken into account, ensuring that a higher uniformity (i.e., higher Shannon Entropy) increases the probability of generating an image where the distance between objects is close to the bound below which GO is not feasible and the behavior of the electromagnetic signal becomes more complex and requires a full treatment of the Maxwell equations. This way, Shannon Entropy provides a metric to compute diversity for the training data plus an upper bound, where GO would not

be valid anymore.

The connection between the Shannon entropy and the electromagnetic field is still uncertain. This uncertainty can be circumvented by introducing the Kolmogorov Complexity, which is the shortest string of binary digits to faithfully describe the object. The Kolmogorov Complexity finds a lower bound at the Shannon Entropy of that object, as shown in [111, 112]. The Shannon entropy can be understood as a measure of the uncertainty for the value of the dielectric constant in an arbitrary position of the room. As it increases for certain examples, so does the lower bound of its Kolmogorov complexity. Intuitively, the higher the Shannon entropy of the image, the larger the probability of objects being close to one another, which implies a greater complexity in the resulting electromagnetic field.

4.4   Results

Initially, 2000 geometries are generated, all of them $400m^2$ square rooms that could represent a warehouse, manufacturing facility, office or any other type of industrial facility. Each of these different geometries is formed by a 11×11 regular mesh where the edges represent a possible location for the antenna (121 antenna locations). This mesh must not be mistaken for the finite element mesh (in this case 41×41) that the numerical simulation software uses to solve the PDEs that characterize the electromagnetic field. These are simple geometric points used to calculate errors during training and incorporating the essential physics information of the problem.

It is important to highlight that for the same geometry but different antenna positions, the Geometric and Integration Path Information Channels can drastically change. An intuitive understanding can be built using the following reasoning: In figure 4.6a, we can fathom from the Geometric Information Channels image that the antenna is in the bottom left corner of

	Percentage	Different Geometries	Number of Simulations
Testing	20%	400	48400
Training	64%	1280	154880
Validation	16%	320	38720

Table 4.1: Geometry distribution for each process: testing, training and validation

the room, which causes the RSSI to be low in the opposite corner. If on the contrary the antenna were located in the upper right corner, the RSSI would show a completely different shape.

20% of the cases were used for testing and the remaining 80% were split again: 80% for active training and 20% for validation, as shown in the table 4.1. In the case a geometry was used for testing, training or validation, all of the 121 antenna locations related to this geometry were included in the same process in order to guarantee that the testing and validation processes were always done with completely new geometries. All sets were randomly selected from the data to avoid bias and overlap, so that validation and testing are independent of training.

The entire workflow is run on a moderately provisioned workstation in order to represent typical computing capability for a small to medium sized company. The specifications include: an Intel Xeon W-2155 CPU (3.30GHz), 128GB RAM (2666MHz DDR4 RDIMM ECC) and a Nvidia Quadro P6000 (24 GB GDDR5) Graphics Card. With these resources, the entire workflow required 2 days to produce an "edge ready" CNN capable of reproducing similar results compared to classic simulations. It is important to highlight that for computational effort comparison, we used the same amount of data (and the same Kepler Scientific Workflow) to train a Residual NN (ResNet), which required twenty times as much computational time to reach acceptable but worse training errors. It is likely that the accuracy results will improve with more data which will push the computation time delta even further. This is a typical barrier to using these deep NNs which require huge data sets (e.g., ImageNet dataset).

The input data consisted of four nominally independent information-channels as explained in the CNN architecture that provide essential independent information. For example, the integration path channel provides the network with information needed to embed fundamental wave physics into the network structure during training via application of the integration path filters. Herein, three different filters can be applied. Resulting differences between each filter are illustrated in table 4.2. Based upon the Normalized Mean Squared Error (NMSE), it is shown that including the complex filter in the integration path channel achieves the best results. This filter is the only one that considers the imaginary part of the behavior of the EM signal, and therefore also becomes the most computationally expensive one, as seen in table 4.5.

Once the best filter is found, we are ready to run the information-channel comparison by removing one information channel at a time (one of the experiments is also done removing both geometric channels). The physics information channel is retained in each experiment because it contains information about the basic physics (e.g. antenna location/power and geolocated material properties) needed to solve the problem, and the integration path channel is applied with the complex filter (which achieved the best results). In table 4.3 the importance of the geometric channel (when both angle and distance are considered as a single one) is shown, as performance drops significantly when removed. The geometric (distance) channel, when it is considered as a different one than the geometric (angle), appears to be the second most relevant one, nearly tied with the integration path information channel (with the complex filter) in training performance. Indeed, both can be considered to provide similar information: power decay with distance. However, these results show that both are necessary, if one of them is removed the precision will drop significantly. The geometric (angle) channel computes the lowest improvement. This result makes sense given that the angle is only important when a ray bounces within the boundaries, which is at the same time the most difficult behavior to predict.

Filter	Loss (NMSE)	R^2	MSE	NMSE (dB)
Complex	0.1866	0.8133	0.0643	-7.29088
Exponential	0.1920	0.8080	0.0561	-7.16699
Linear	0.1926	0.8074	0.0667	-7.15344

Table 4.2: Results obtained comparing the 3 different filters of the Integration Path Information Channel. These results show that the complex filter has a significantly lower NMSE indicating better performance.

Active Information Channels	Loss (NMSE)	Δ
Physics, Geometric (distance), Geometric (angle)	0.1941	0.0075
Physics, Geometric (angle), Integration Path	0.1947	0.0081
Physics, Geometric (distance), Integration Path	0.1914	0.0048
Physics, Integration Path	0.2811	0.0945

Table 4.3: One or two of the channels is removed. The difference between the best result obtained in table 4.2 is computed by $\Delta = Loss_i - Loss_b$, where i indicates the ith-layer missing and $Loss_b = 0.1866$ is the base loss to compare with. In the cases the integration path channel is active, the complex filter is applied.

For a more visual comparison, in figure 4.6a we present a random geometry used for testing purposes with the four information channels. Figure 4.6b provides a comparison of the numerical simulation result and the one predicted by the trained NN to demonstrate the precision of the prediction for one of the thousands of geometry tested. Although the NN output is more granulated and does not capture the diffraction behavior due to the channel effect, the main regions of good coverage and shadowed regions are differentiated with high precision.

With these results along with the capacity of the NN to run thousands of simulations in a regular laptop or tablet in few seconds this approach can be effectively applied to several engineering applications. While a single GO simulation took a mean time of 14s, our trained NN needs 0.35s (we reduce more than 100 times the prediction time). As an example of practical application, this approach can be practically used to determine the best antenna location(s) within the complex floor-plans of a typical advanced manufacturing facility. For this, an efficient workflow can be developed where tens or hundreds of different antenna locations can be digitally tested with the trained NN in real time and the antenna location

that obtains the best coverage results (such as the most space covered above a certain threshold) is selected as the effective one. Another example where this speed boost can be beneficial is in indoor localization applications.
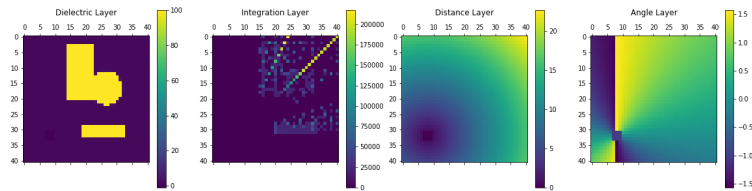
(a) The four input layers are shown. In the dialectric layer the geometry is described.

(b) Numerical simulation on the left and neural network prediction on the right.

Figure 4.6: Result comparison within numerical simulation and our NN results during the testing process. The object shadows are predicted, but not the channel effect.

In addition, having efficient and effective workflows for NN development of electromagnetic response reveals new opportunities to explore relationships between encoded information of NN and the numerical of WIFI communications. For example, these studies have revealed an intriguing relationship between the Shannon Entropy of study problems and amount of computational effort (e.g. number of training epochs) required to achieve accurate results. We have found that geometries with low Shannon Entropy required noticeably lower training effort to achieve similar NMSE compared to the high Shannon Entropy geometries. To illustrate this we divide the geometries into 3 classes by applying the simple arithmetic equation: $\delta_s = \frac{s_{max} - s_{min}}{3}$. Hence, each class is defined as

- *low entropy*: $s_{min} \leq s < s_{min} + \delta_s$.
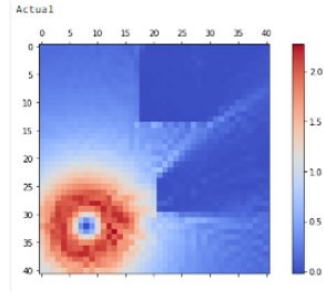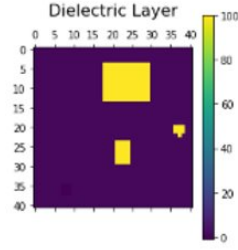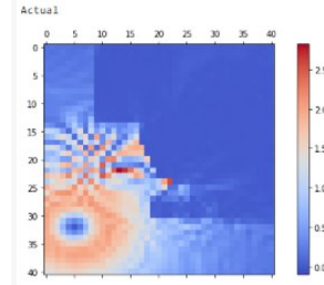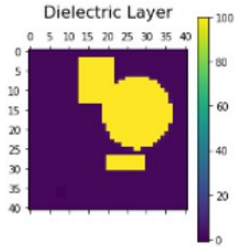
Figure 4.7: In low entropy geometries *(top)* objects' distance ensures negligible radio channel effects, whereas in the high entropy ones *(bottom)* these effect become an important part of noise.

- *transient entropy*: $s_{min} + \delta_s \leq s < s_{min} + 2\delta_s$.

- *high entropy*: $s_{min} + 2\delta_s \leq s < s_{max}$.

These names are assigned to differentiate the classes and have no physical implications beyond reflecting the limit where GO approach is still valid for the highest entropy. By way of example, in figure 4.7 the differences between a low and high entropy simulation are shown where we see the radio channel effect is insignificant in the low entropy geometry, but notable in the high entropy one.

This behavior opens up the possibility of optimizing training for random geometries by sorting according to Shannon Entropy. To illustrate this the number of geometries used for training purposes for these different classes are:

- Number of geometries used in Training:

Entropy / Loss	Complex Filter (NMSE)	Exponential Filter (NMSE)	Linear Filter (N...
High	0.2162	0.2211	0.2328
Transient	0.1674	0.1725	0.1666
Low	0.1627	0.1690	0.1600

Table 4.4: Results obtained when testing separately the three 3 entropical classes.

  - 666 High-Entropy geometries,

  - 548 Transient geometries,

  - 386 Low-Entropy geometries.

- Number of geometries used in Testing:

  - 167 High-Entropy geometries,

  - 137 Transient geometries,

  - 96 Low-Entropy geometries.

Note that even though the number of geometries with high entropy are much higher than for low entropy, the results are better for the low entropy cases as shown in table 4.4. These results show the NMSE obtained if the training data is taken without regard to entropic class, but the testing is only done with one of the groups. It can be seen that the simpler the geometry (less detail in the floor-plan), the faster is the training and the better the precision of the model. In addition, a more significant performance drop can be seen for the highest entropy class, whereas transient and low entropy classes could be even be regrouped into a single one. As these classes where artificially generated by just splitting them in three equal parts, a more detailed study is needed to properly understand this behavior.

Resources	Training Time (s)
Complex Filter	54354
Exponential Filter	40569
Linear Filter	38934

Table 4.5: Computational Resources spent in training a NN with different Integration Path Filters

4.5 Conclusions and Future Work

In this paper, we have presented an efficient scientific workflow that produces a Physics-Informed Convolutional Neural Network (CNN) model capable of running complicated electromagnetic wave propagation (at WiFi frequencies) simulations to determine the real time Received Signal Strength Intensity (RSSI) which can be used for determining wireless communication connectivity in advanced manufacturing contexts. These simulations are done in a constant enclosed space composed by inner objects with variable position, shape, size and reflectivity. The workflow utilizes numerical PDE simulations to generate synthetic data for both training and testing states, and suggests adaptive mechanisms to incorporate real time sensed data to improve accuracy for geolocating people (inferred from their mobile technologies such as smart watches) moving through WiFi fields.

The resulting CNN has been trained to predict similar results to a more common approach that utilizes numerical approximations to PDEs at drastically reduced computational cost. We show how different information channels effect the training and performance of the resulting CNNs. Importantly we show the effectiveness of incorporating physics based information channels to improve the CNN performance. Not only do these physics based information channels inculcate critical behaviors (e.g., dissipation, reflection and refraction in WiFi simulations) into the structure of the CNNs, the results implicate useful insight into future work regarding the interpretability issues surrounding artificial neural networks in general. As additional future work, research must be done about how to improve radio channel effects, which is the main source of error in many numerical approaches to electromagnetic signal

estimation.

The scientific workflows described in this paper are, relatively speaking, computationally intensive with respect to data acquisition and training. However, the resources required amount to two days of effort on a modestly provisioned deskside workstation. Incorporation of important information channels such as the complex filter integration path channel can significantly reduce this effort and represents a generalized method for improving scientific workflows to generate CNNs in other fields that are commonly described by wave equations. Although this integration path is a common technique for many applications, the use of the integration path for improving training and prediction performance for Artificial Neural Networks applied to electromagnetic fields seems to be a new approach.

When designing model architectures, we also evaluated the incorporation of pre-trained inner layers from deep neural networks into our model, considering the learned underlying associations between neighboring pixels can be possibly transferred to our study case. In fact, the inclusion of deep neural networks in Physics-Informed problems is under considerable debate [54, 50]. As a future work, scaling a ResNet architecture according to the cost of data acquisition and training computational power will be discussed.

Also of importance is the observation of correlations between the Shannon Entropy of the geometry, which we initially used to ensure the data independence, and the total amount of data required for our CNN to converge. The greater the Shannon Entropy, the greater the amount of data required. Regardless of the size of the training set, if it has a greater Shannon Entropy it seems to produce a NN with a lower precision. We consider these links between the Shannon Entropy of an object, the complexity of the physics occurring around that object and the capacity of a NN to reproduce the latter from the former an interesting case for future study. This surprising result also conforms to our findings relative to the impact on CNN learning efficiency that incorporation of diverse information channels exhibits. These interesting results will certainly inform the next step in the evolution of

these workflows to include real time measured data associated with factory floor workflows in real industrial settings that are increasingly provisioned with Industrial Internet of Things technologies dependent upon reliable wireless communications.

4.6 Using the Convolutional Neuron Network for Target Localization and Wall Characterization in the Through the Wall Imaging Problem

This part pf thesis investigates the Through the Wall Imaging (TWI) problem via machine learning. To solve the TWI problem in presence of the wall, a Convolution Neuron Network (CNN) is proposed. The detection of the scatterers behind the wall when there is a strong reflection from the front wall is very challenging. Several microwave imaging algorithms have been introduced to extract the unknown parameters of the wall and mitigate the wall clutter to predict the location of the target. This process is very time-consuming even though it has accurate results. In this paper, we developed a method for exploiting the complex information for the TWI problem by using a CNN that accepts complex numbers from the receiver to predict wall thickness, material, and location of the target behind the wall at the same time. We show that our proposed model can predict these parameters with an accuracy of 92.6%.

Recent experiments in microwave imaging cover various applications such as radar imaging [56], object detection [113], medical imaging [58] and so on. Real-time through-the-wall imaging is one of the most interesting applications of this technology [59, 60, 61]. In a TWI system, the main goal is to detect and locate targets behind the wall by transmitting and receiving EM waves. The back-scattered signal from the wall and targets should be analyzed to extract the necessary information such as location, wall thickness, and dielectric

constant. The main challenges in this process are unknown parameters of the wall, the strong reflection of the wall, and time-consuming algorithms to reconstruct images. In the introduced microwave imaging algorithms in the literature, first, we need to estimate wall parameters and then complex algorithms are required for clutter removal as wall reflection.

An alternative method that is introduced in this paper is in the area of machine learning (ML). This method is based on the statistical theory to extract the interesting, practical, and unknown parameters from the big database. ML is a very practical way to extract information from big data. Support vector machines (SVMs) are new tools that by using optimization methods solve the problem of machine learning. Many applications based on the ML have been developed for the imaging problem such as through the wall imaging and synthetic aperture radar (SAR) [62, 63, 64].

In this section, we have introduced Convolution Neuron Network (CNN) to provide comparative performance to the previous microwave imaging algorithms when TWI is considered as the regression problem. This method not only estimates the wall thickness and permittivity but also estimates the location of the target behind the wall. In comparison with traditional electromagnetic methods, our proposed approach needs only a few seconds to process the estimation. However, to the best of our knowledge, this is the first reported attempt to use ML in the TWI problem to extract four parameters one at a time. It means we can remove the back-scattered signal and at the same time roughly calculate the parameters of the wall and more importantly calculate the location of the target behind the wall, all at the same time and one algorithm.

4.7   Complex CNN for TWI Problem and Results

We present a simple example with simulated data generated by Comsol Multiphysics software. For simplicity, a 2D one-layer dielectric wall is considered and the two-dimensional frequency-domain study for Electromagnetic Wave is performed. Moreover, An infinite line current as a transmitter and the co-polarized electric field as the received signal is used. In this study, one PEC cylinder is placed behind the wall at (x,y) location and its radius is 2 cm. Locations are 100 random points in the region behind the wall with 10 random values for both x and y. The line current is in (0,-100cm) and measured electric fields are randomly placed in y-axis from -100 cm to 100 cm with a step size of 10cm, behaving as a transceiver parallel to the first interface of the layered media with a standoff distance of 100 cm. The operating frequency of the source is 2 GHz. The wall is a one-layer dielectric slab with relative permittivity of epsilon with 10 random value which is randomly selected between 2 and 5. Also, the thickness of the wall (d) is randomly spaced between 10 and 30 cm with 10 values. So there are a total of 10,000 simulations and data sets. The geometry of the TWI problem is depicted in Figure 4.8.

We describe the proposed CNN that uses the two separated input layers. This CNN consists of several multi-resolution layers such as convolution and pooling layers to pass information from layer to layer and link them together in a chain.

The proposed CNN topology for the TWI problem which enables the prediction of the location of the cylindrical object (x,y), thickness, and dielectric constant of the wall are summarized in Figure 4.9. The number of network layers and filters in the proposed CNN is smaller than in many general-purpose CNN implementations in order to protect against overfitting due to the limited number of training data in this problem.

The received signals from 21 linear antennas are complex numbers. One of the challenges of the implementation of CNN with complex numbers is selecting an appropriate activation

function. A practicable activation function should be differentiable and non-linear at the same time. But none of the well-known activation functions such as ReLU, Sigmoid and hyperbolic tangent is differentiable for complex inputs. In the TWI problem, both magnitude and phase contain significant information and can not be disregarded. In order to solve this issue, magnitude and phase information from each antenna is separated and fed the CNN individually as depicted in Fig. 4.10. It is clear that using the real and imaginary part of the received complex number in training reach the same results. The rest of the network consists of common convolution and pooling layers, then this information will be linked together in a chain of again convolution and pooling layers. The goal of the combination of the two inputs is to find out the relationship between the magnitude and phase of the received signal from the object by these hidden layers. Tanh activation function is used for all the layers instead of the last layer which is set as linear to implement the CNN regression problem properly. The output of the designed CNN has 4 values to estimate our desired targets which are the location of the object (x,y), thickness, and material of the wall between antenna array and object.

Before using input signals by CNN for training, they are normalized to the value that falls between [-0.5, 0.5], with a signal average of 0. If $E(x, y)$ represents the received unnormalized electric field as input and N total number of data set which is 10000 in our problem, then the normalized feature $E(x, y)$ is defined as bellow:

$$E_n(x, y) = \frac{E(x, y) - \frac{1}{N} \sum_{i,j} E(x, y)}{\sigma(E(x, y))} \tag{4.21}$$

Where σ is the standard deviation of the feature values. The same approach is used for the normalization of the wall parameters.
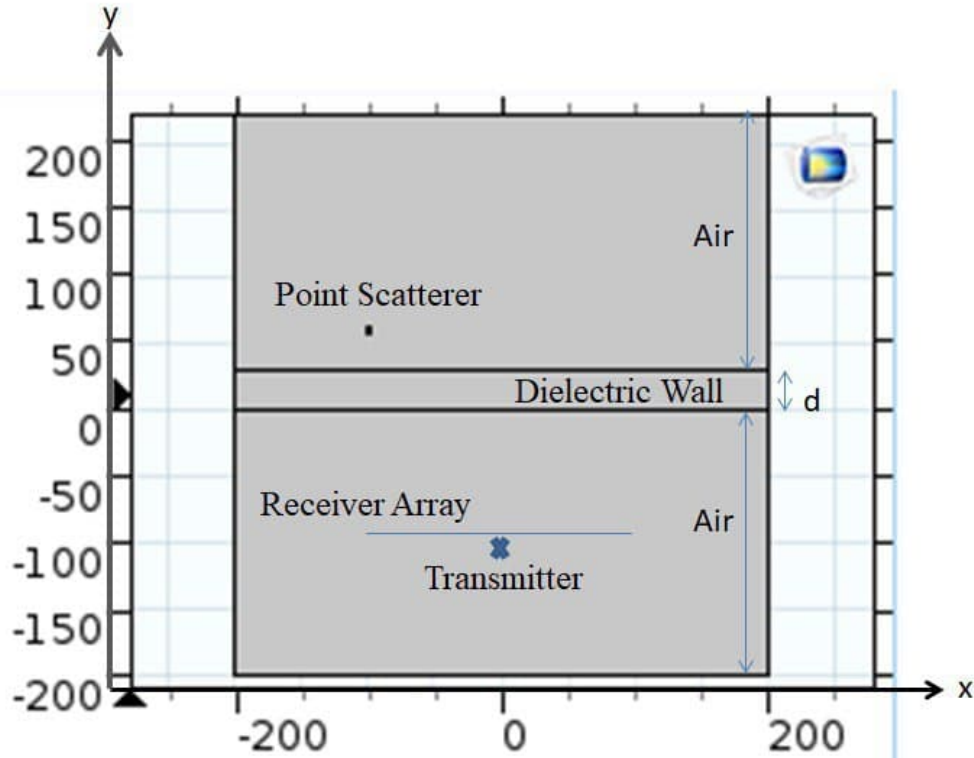
Figure 4.8: Simulation setup of the through the wall imaging problem.

Finally, the data set is split into 80% training and 20% test sets of 8000 and 2000 scenarios respectively. Then we trained the CNN with a batch size of 128 and each test involved training for 1000 epochs. For the Magnitude/Phase CNN the training accuracy is 96.5%, while the accuracy for the testing set is 92.6%. The loss function is set to be the root mean squared error (RMSE) for this regression problem and defined to be the average RMSE of the 4 output parameters. The unit of RMSE for the center location of the object and wall thickness is (cm) and for the material of the wall is unitless. For the training set, the RMSE is calculated near 0.007 and for the test set, is around 0.06. In Fig. 4.10, the round dots shows some of the predicted value of the location of the object (x,y), permittivity, and thickness of the wall. Also, 45° diagonal line is shown to indicate how the predicted value is accurate. These results show proposed approach has desirable prediction properties and can be used for further investigation.
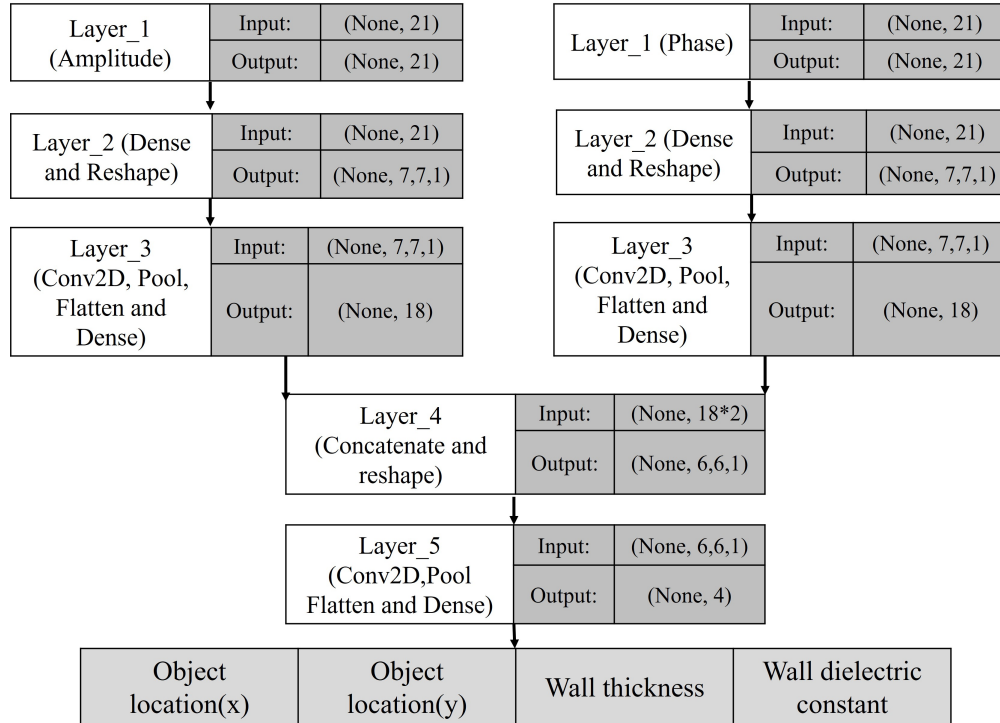
Figure 4.9: architecture of the proposed magnitude-phase CNN.

4.8 Conclusion and future work

Through the wall target detection is an important area that has a wide range of applications. By using a deep convolutional neural network, we have shown that we can predict the location of unknown targets as well as wall material and the thickness of the wall precisely at the same time and with less time in comparison with previously proposed algorithms which are very complex. These results show that this method can be utilized for suppressing the wall and background clutter as well. Our future work will focus on validating the performance improvement of the proposed complex-valued CNN when there is noise in the data set with different SNR. Another plan is to detect and classify multiple targets of different sizes at the same time. Another improvement could be showing the accuracy and loss of each output individually.
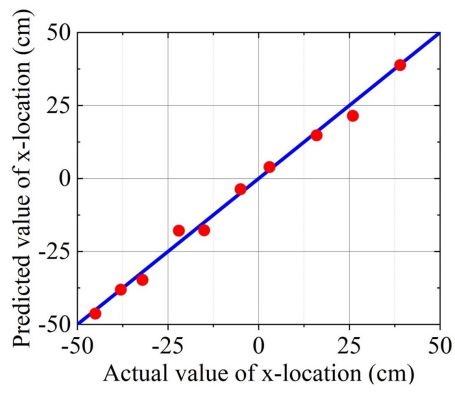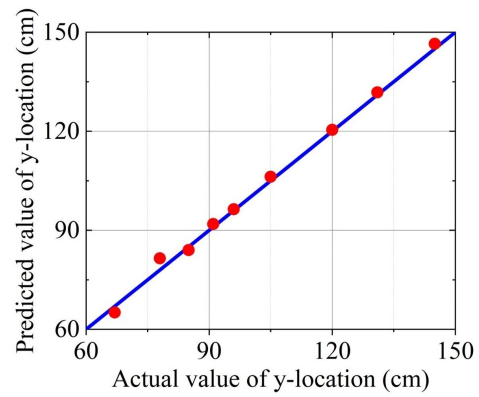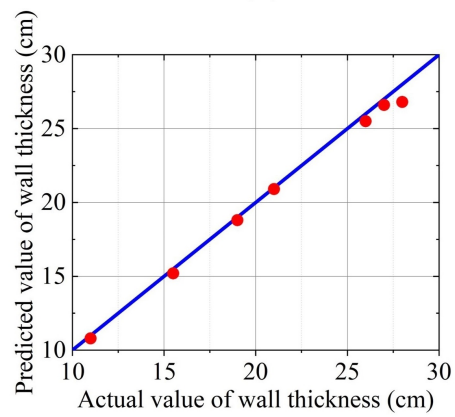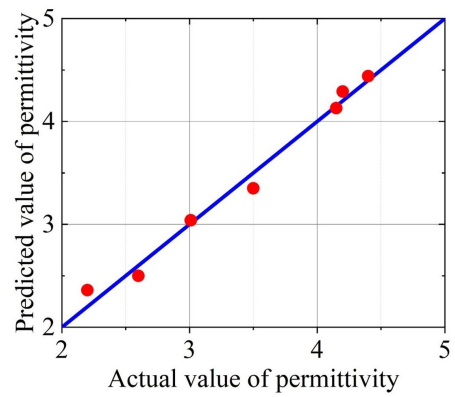
Figure 4.10: prediction values of the (a) x-location, (b) y-location, (c) wall-thickness and (d) permittivity versus the actual values.

Bibliography

[1] Theodore S Rappaport, Shu Sun, Rimma Mayzus, Hang Zhao, Yaniv Azar, Kevin Wang, George N Wong, Jocelyn K Schulz, Mathew Samimi, and Felix Gutierrez. Millimeter wave mobile communications for 5g cellular: It will work! *IEEE access*, 1:335–349, 2013.

[2] Ekram Hossain and Monowar Hasan. 5g cellular: key enabling technologies and research challenges. *IEEE Instrumentation & Measurement Magazine*, 18(3):11–21, 2015.

[3] Theodore S Rappaport, Robert W Heath Jr, Robert C Daniels, and James N Murdock. *Millimeter wave wireless communications*. Pearson Education, 2015.

[4] Ahmed Iyanda Sulyman, AlMuthanna T Nassar, Mathew K Samimi, George R MacCartney, Theodore S Rappaport, and Abdulhameed Alsanie. Radio propagation path loss models for 5g cellular networks in the 28 ghz and 38 ghz millimeter-wave bands. *IEEE communications magazine*, 52(9):78–86, 2014.

[5] A Dierck, T De Keulenaer, F Declercq, and H Rogier. A wearable active gps antenna for application in smart textiles.

[6] Giulia Orecchini, Manos M Tentzeris, Li Yang, and Luca Roselli. ” smart shoe”: an autonomous inkjet-printed rfid system scavenging walking energy.

[7] B Gupta, S Sankaralingam, and S Dhar. Development of wearable and implantable antennas in the last decade: A review.

[8] Luigi Vallozzi, Waldo Vandendriessche, Hendrik Rogier, Carla Hertleer, and Maria Lucia Scarpello. Wearable textile gps antenna for integration in protective garments. *Proceedings of the Fourth European Conference on Antennas and Propagation*, pages 1–4, 2010.

[9] Masood Ur-Rehman, Nabeel Ahmed Malik, Xiaodong Yang, Qammer Hussain Abbasi, Zhiya Zhang, and Nan Zhao. A low profile antenna for millimeter-wave body-centric applications. *IEEE Transactions on Antennas and Propagation*, 65(12):6329–6337, 2017.

[10] Maggie Yihong Chen, Daniel Pham, Harish Subbaraman, Xuejun Lu, and Ray T Chen. Conformal ink-jet printed c-band phased-array antenna incorporating carbon nanotube

field-effect transistor based reconfigurable true-time delay lines. *IEEE Transactions on Microwave Theory and Techniques*, 60(1):179–184, 2011.

[11] Syeda Fizzah Jilani, Ardavan Rahimian, Yasir Alfadhl, and Akram Alomainy. Low-profile flexible frequency-reconfigurable millimetre-wave antenna for 5g applications. *Flexible and Printed Electronics*, 3(3):035003, 2018.

[12] Syeda Fizzah Jilani, Max O Munoz, Qammer H Abbasi, and Akram Alomainy. Millimeter-wave liquid crystal polymer based conformal antenna array for 5g applications. *IEEE Antennas and Wireless Propagation Letters*, 18(1):84–88, 2018.

[13] Jack P Lombardi, Robert E Malay, James H Schaffner, Hyok Jae Song, Ming-Huang Huang, Scott C Pollard, Mark D Poliks, and Timothy Talty. Copper transparent antennas on flexible glass by subtractive and semi-additive fabrication for automotive applications. *2018 IEEE 68th Electronic Components and Technology Conference (ECTC)*, pages 2107–2115, 2018.

[14] Soumyadeep Das and Debasis Mitra. A compact wideband flexible implantable slot antenna design with enhanced gain. *IEEE Transactions on Antennas and Propagation*, 66(8):4309–4314, 2018.

[15] Mohammed Tighezza, SKA Rahim, and MT Islam. Flexible wideband antenna for 5g applications. *Microwave and Optical Technology Letters*, 60(1):38–44, 2018.

[16] Seungman Hong, Seok Hyon Kang, Youngsung Kim, and Chang Won Jung. Transparent and flexible antenna for wearable glasses applications. *IEEE Transactions on Antennas and Propagation*, 64(7):2797–2804, 2016.

[17] Arnaut Dierck, Hendrik Rogier, and Frederick Declercq. A wearable active antenna for global positioning system and satellite phone. *IEEE Transactions on Antennas and Propagation*, 61(2):532–538, 2012.

[18] Hadi Bahramiabarghouei, Emily Porter, Adam Santorelli, Benoit Gosselin, Milica Popović, and Leslie A Rusch. Flexible 16 antenna array for microwave breast cancer detection. *IEEE Transactions on Biomedical Engineering*, 62(10):2516–2525, 2015.

[19] Rula S Alrawashdeh, Yi Huang, Muayad Kod, and Aznida Abu Bakar Sajak. A broadband flexible implantable loop antenna with complementary split ring resonators. *IEEE antennas and wireless propagation letters*, 14:1506–1509, 2015.

[20] Jang-Soon Park, Jun-Bong Ko, Heon-Kook Kwon, Byung-Su Kang, Bonghyuk Park, and Dongho Kim. A tilted combined beam antenna for 5g communications using a 28-ghz band. *IEEE Antennas and Wireless Propagation Letters*, 15:1685–1688, 2016.

[21] Igor Syrytsin, Shuai Zhang, Gert Frølund Pedersen, and Arthur S Morris. Compact quad-mode planar phased array with wideband for 5g mobile terminals. *IEEE Transactions on Antennas and Propagation*, 66(9):4648–4657, 2018.

[22] Lingyu Kong and Xiaojian Xu. A compact dual-band dual-polarized microstrip antenna array for mimo-sar applications. *IEEE Transactions on Antennas and Propagation*, 66(5):2374–2381, 2018.

[23] Qinyin Jia, Hongcheng Xu, MF Xiong, Binzhen Zhang, and Junping Duan. Omnidirectional solid angle beam-switching flexible array antenna in millimeter wave for 5g micro base station applications. *IEEE Access*, 7:157027–157036, 2019.

[24] Syeda Fizzah Jilani, Qammer H Abbasi, and Akram Alomainy. Inkjet-printed millimetre-wave pet-based flexible antenna for 5g wireless applications.

[25] Yu Jian Cheng, Hang Xu, Da Ma, Jie Wu, Lei Wang, and Yong Fan. Millimeter-wave shaped-beam substrate integrated conformal array antenna. *IEEE Transactions on Antennas and Propagation*, 61(9):4558–4566, 2013.

[26] Hsuan-Ling Kao, Cheng-Lin Cho, Xiu Yin Zhang, Li-Chun Chang, Bai-Hong Wei, Xin Dai, and Hsien-Chin Chiu. Bending effect of an inkjet-printed series-fed two-dipole antenna on a liquid crystal polymer substrate. *IEEE Antennas and Wireless Propagation Letters*, 13:1172–1175, 2014.

[27] Hsuan-Ling Kao, Chih-Sheng Yeh, Xiu Yin Zhang, Cheng-Lin Cho, Xin Dai, Bai-Hong Wei, Li-Chun Chang, and Hsien-Chin Chiu. Inkjet printed series-fed two-dipole antenna comprising a balun filter on liquid crystal polymer substrate. *IEEE Transactions on Components, Packaging and Manufacturing Technology*, 4(7):1228–1236, 2014.

[28] Constantine A. Balanis. *Advanced Engineering Electromagnetics By C. A. Balanis.* 2007.

[29] John W. McKown and R. Lee Hamilton. Ray Tracing as a Design Tool for Radio Networks. *IEEE Network*, 1991.

[30] Kate A. Remley, Harry R. Anderson, and Andreas Weisshar. Improving the accuracy of ray-tracing techniques for indoor propagation modeling. *IEEE Transactions on Vehicular Technology*, 2000.

[31] Ying Wang, Safieddin Safavi-Naeini, and Sujeet K. Chaudhuri. A hybrid technique based on combining ray tracing and FDTD methods for site-specific modeling of indoor radio wave propagation. *IEEE Transactions on Antennas and Propagation*, 2000.

[32] Guillaume de la Roche, Katia Jaffrès-Runser, and Jean Marie Gorce. On predicting in-building WiFi coverage with a fast discrete approach. *International Journal of Mobile Network Design and Innovation*, 2007.

[33] Cassio Bento Andrade and Roger Pierre Fabris Hoefel. IEEE 802.11 WLANS: A comparison on indoor coverage models. In *Canadian Conference on Electrical and Computer Engineering*, 2010.

[34] S. Zvanovec. Results of indoor propagation measurement campaign for WLAN systems operating in 2.4 GHz ISM band. 2005.

106

[35] Kaveh Pahlavan and Allen H. Levesque. *Wireless Information Networks: Second Edition.* 2005.

[36] Jaime Lloret, Jose J. López, Carlos Turró, and Santiago Flores. A fast design model for indoor radio coverage in the 2.4 GHz wireless LAN. In *1st International Symposium on Wireless Communication Systems 2004, Proceedings ISWCS '04*, 2004.

[37] Klemen Bregar and Mihael Mohorcic. Improving Indoor Localization Using Convolutional Neural Networks on Computationally Restricted Devices. *IEEE Access*, 2018.

[38] Jahyoung Koo and Hojung Cha. Localizing WiFi access points using signal strength. *IEEE Communications Letters*, 2011.

[39] Stuart A. Golden and Steve S. Bateman. Sensor measurements for Wi-Fi location with emphasis on time-of-arrival ranging. *IEEE Transactions on Mobile Computing*, 2007.

[40] Sirin Tekinay. Wireless Geolocation Systems and Services. *IEEE Communications Magazine*, 1998.

[41] Guolin Sun, Jie Chen, Wei Guo, and K. J.Ray Liu. Signal processing techniques in network-aided positioning: A survey of state-of-the-art positioning designs. *IEEE Signal Processing Magazine*, 2005.

[42] Chouchang Yang and Huai Rong Shao. WiFi-based indoor positioning. *IEEE Communications Magazine*, 2015.

[43] Edgar A. Martínez, Raúl Cruz, and Jesús Favela. Estimating user location in a WLAN using backpropagation neural networks. In *Lecture Notes in Artificial Intelligence (Subseries of Lecture Notes in Computer Science)*, 2004.

[44] Arvin Wen Tsui, Yu Hsiang Chuang, and Hao Hua Chu. Unsupervised learning for solving RSS hardware variance problem in WiFi localization. *Mobile Networks and Applications*, 2009.

[45] Wei Zhang, Kan Liu, Weidong Zhang, Youmei Zhang, and Jason Gu. Deep Neural Networks for wireless localization in indoor and outdoor environments. *Neurocomputing*, 2016.

[46] Michacł Nowicki and Jan Wietrzykowski. Low-effort place recognition with WiFi fingerprints using deep learning. In *Advances in Intelligent Systems and Computing*. 2017.

[47] Ming Luo and K. Huang. Prediction of the electromagnetic field in metallic enclosures using artificial neural networks. *Progress in Electromagnetics Research*, 116(March):171–184, 2011.

[48] Chao Xu, Changlong Wang, Fengzhu Ji, and Xichao Yuan. Finite-element neural network-based solving 3-D differential equations in mfl. *IEEE Transactions on Magnetics*, 2012.

[49] Md. A. Salam, Swee P. Ang, Quazi M. Rahman, and Owasis A. Malik. Estimation of Magnetic Field Strength near Substation Using Artificial Neural Network. *International Journal of Electronics and Electrical Engineering*, pages 166–171, 2016.

[50] Oameed Noakoasteen, Shu Wang, Zhen Peng, and Christos Christodoulou. Physics-Informed Deep Neural Networks for Transient Electromagnetic Analysis. *IEEE Open Journal of Antennas and Propagation*, 1:404–412, 2020.

[51] M. Raissi, P. Perdikaris, and G. E. Karniadakis. Physics-informed neural networks: A deep learning framework for solving forward and inverse problems involving nonlinear partial differential equations. *Journal of Computational Physics*, 2019.

[52] Lu Lu, Xuhui Meng, Zhiping Mao, and George Em Karniadakis. DeepXdE: A deep learning library for solving differential equations. In *CEUR Workshop Proceedings*, 2020.

[53] Ryan King, Oliver Hennigh, A. Mohan, and M. Chertkov. From deep to physics-informed learning of turbulence: Diagnostics, 2018.

[54] Jonathan Viquerat and Elie Hachem. A supervised neural network for drag prediction of arbitrary 2D shapes in laminar flows at low Reynolds number. *Computers and Fluids*, 210, 2020.

[55] Phillip Isola, Jun Yan Zhu, Tinghui Zhou, and Alexei A. Efros. Image-to-image translation with conditional adversarial networks. In *Proceedings - 30th IEEE Conference on Computer Vision and Pattern Recognition, CVPR 2017*, 2017.

[56] Müjdat Çetin, Ivana Stojanović, N Özben Önhon, Kush Varshney, Sadegh Samadi, William Clem Karl, and Alan S Willsky. Sparsity-driven synthetic aperture radar imaging: Reconstruction, autofocusing, moving targets, and compressed sensing. *IEEE Signal Processing Magazine*, 31(4):27–40, 2014.

[57] Marco Salucci, Lorenzo Poli, Giacomo Oliveri, Raffaele Persico, Grazia Semeraro, Corrado Notario, and Andrea Massa. Advanced techniques for gpr microwave imaging: An experimental study. *2017 IEEE International Symposium on Antennas and Propagation & USNC/URSI National Radio Science Meeting*, 2017.

[58] S Sadeghi and R Faraji-Dana. A practical uwb microwave imaging system using time-domain dort for tumor detection. *The Applied Computational Electromagnetics Society Journal (ACES)*, pages 692–699, 2016.

[59] Sajjad Sadeghi, Karim Mohammadpour-Aghdam, Kai Ren, Reza Faraji-Dana, and Robert J Burkholder. A pole-extraction algorithm for wall characterization in through-the-wall imaging systems. *IEEE Transactions on Antennas and Propagation*, 67(11):7106–7113, 2019.

[60] S Sadeghi, K Mohammadpour-Aghdam, R Faraji-Dana, and Robert J Burkholder. A novel algorithm for wall characterization in through the wall imaging based on

spectral analysis. *2018 18th International Symposium on Antenna Technology and Applied Electromagnetics (ANTEM)*, pages 1–2, 2018.

[61] Sajjad Sadeghi, Karim Mohammadpour-Aghdam, Reza Faraji-Dana, and Robert J Burkholder. A dort-uniform diffraction tomography algorithm for through-the-wall imaging. *IEEE Transactions on Antennas and Propagation*, 68(4):3176–3183, 2019.

[62] Michael Wilmanski, Chris Kreucher, and Alfred Hero. Complex input convolutional neural networks for wide angle sar atr. *2016 IEEE Global Conference on Signal and Information Processing (GlobalSIP)*, pages 1037–1041, 2016.

[63] Fok Hing Chi Tivive and Abdesselam Bouzerdoum. Toward moving target detection in through-the-wall radar imaging. *IEEE Transactions on Geoscience and Remote Sensing*, 59(3):2028–2040, 2020.

[64] Aihua Wood, Ryan Wood, and Matthew Charnley. Through-the-wall radar detection using machine learning. *Results in Applied Mathematics*, 7:100106, 2020.

[65] Ming Yu, Antonio Panariello, Mostafa Ismail, and Jingliang Zheng. Passive 3-d simulators. *IEEE Microwave Magazine*, 9(6):50–61, 2008.

[66] Kepei Sun. Rectangular waveguide filled with uniaxial medium and negative resistance enhanced composite right/left-handed transmission line. 2017.

[67] NG Alexopoulos. Integrated-circuit structures on anisotropic substrates. *IEEE Transactions on Microwave Theory and Techniques*, 33(10):847–881, 1985.

[68] Lin-Feng Chen, CK Ong, CP Neo, VV Varadan, and Vijay K Varadan. Microwave electronics: measurement and materials characterization. 2004.

[69] RM Nelson, DA Rogers, and A Gomes D'Assuncao. Resonant frequency of a rectangular microstrip patch on several uniaxial substrates. *IEEE transactions on antennas and propagation*, 38(7):973–981, 1990.

[70] Thomas Weiland, Martin Timm, and Irina Munteanu. A practical guide to 3-d simulation. *IEEE Microwave Magazine*, 9(6):62–75, 2008.

[71] http://www.cst.com/.

[72] Daniel G Swanson and Wolfgang JR Hoefer. Microwave circuit modeling using electromagnetic field simulation. *Artech House*, 2003.

[73] Ao Li, Kwai-Man Luk, and Yujian Li. A dual linearly polarized end-fire antenna array for the 5g applications. *IEEE Access*, 6:78276–78285, 2018.

[74] David M Pozar. Microstrip antenna aperture-coupled to a microstripline. *Electronics letters*, 21:49, 1985.

[75] F Croq, A Papiernik, and P Brachat. Wideband aperture coupled microstrip subarray. *International Symposium on Antennas and Propagation Society, Merging Technologies for the 90's*, pages 1128–1131, 1990.

[76] J Wang, R Fralich, C Wu, and J Litva. Multifunctional aperture coupled stacked antenna. *Antennas and Propagation Society Symposium 1991 Digest*, pages 727–730, 1991.

[77] Jin-Dong Zhang, Wen Wu, and Da-Gang Fang. Dual-band and dual-circularly polarized shared-aperture array antennas with single-layer substrate. *IEEE Transactions on Antennas and Propagation*, 64(1):109–116, 2015.

[78] Yan Wang and Zhengwei Du. Dual-polarized dual-band microstrip antenna with similar-shaped radiation pattern. *IEEE Transactions on Antennas and Propagation*, 63(12):5923–5928, 2015.

[79] Abdelheq Boukarkar, Xian Qi Lin, Yuan Jiang, Li Ying Nie, Peng Mei, and Yi Qiang Yu. A miniaturized extremely close-spaced four-element dual-band mimo antenna system with polarization and pattern diversity. *IEEE Antennas and Wireless Propagation Letters*, 17(1):134–137, 2017.

[80] Sai Ho Yeung, Alejandro Garcia-Lamperez, Tapan Kumar Sarkar, and Magdalena Salazar-Palma. Thin and compact dual-band four-element broadside patch antenna arrays. *IEEE Antennas and Wireless Propagation Letters*, 13:567–570, 2014.

[81] Shenario Ezhil Valavan, Dinh Tran, Alexander G Yarovoy, and Antoine G Roederer. Dual-band wide-angle scanning planar phased array in x/ku-bands. *IEEE transactions on antennas and propagation*, 62(5):2514–2521, 2014.

[82] Gobi Vetharatnam, Chung Boon Kuan, and Chuah Hean Teik. Combined feed network for a shared-aperture dual-band dual-polarized array. *IEEE Antennas and Wireless Propagation Letters*, 4:297–299, 2005.

[83] Satyajit Chakrabarti. Development of shared aperture dual polarized microstrip antenna at l-band. *IEEE transactions on antennas and propagation*, 59(1):294–297, 2010.

[84] Yizhu Shen, Shi-Gang Zhou, Guan-Long Huang, and Tan-Huat Chio. A compact dual circularly polarized microstrip patch array with interlaced sequentially rotated feed. *IEEE Transactions on Antennas and Propagation*, 64(11):4933–4936, 2016.

[85] P Li, KM Luk, and KL Lau. A dual-feed dual-band l-probe patch antenna. *IEEE transactions on antennas and propagation*, 53(7):2321–2323, 2005.

[86] K Woelder and Johan Granholm. Cross-polarization and sidelobe suppression in dual linear polarization antenna arrays. *IEEE transactions on antennas and propagation*, 45(12):1727–1740, 1997.

[87] Mirhamed Mirmozafari and Guifu Zhang. On sidelobe problem of configured array antennas. *IEEE transactions on Antennas and propagation*, 66(7):3475–3481, 2018.

[88] John W. Dettman and Robert L. Weber. Mathematical Methods in Physics and Engineering. *American Journal of Physics*, 1963.

[89] Ivar Stakgold and Michael Hoist. *Green's Functions and Boundary Value Problems: Third Edition*. 2011.

[90] William H. Adams. Mathematical Methods for Physics and Engineering: A Comprehensive Guide, 2nd Edition. *Materials Research Bulletin*, 2003.

[91] Pyotr Ya Ufimtsev. New insight into the classical Macdonald physical optics approximation. *IEEE Antennas and Propagation Magazine*, 2008.

[92] Pyotr Yakovlevich Ufimtsev. *Theory of edge diffraction in electromagnetics: Origination and validation of the physical theory of diffraction*. 2009.

[93] Kurt Hornik, Maxwell Stinchcombe, and Halbert White. Multilayer feedforward networks are universal approximators. *Neural Networks*, 1989.

[94] Y. S. Wang, C. M. Lee, D. G. Kim, and Y. Xu. Sound-quality prediction for nonstationary vehicle interior noise based on wavelet pre-processing neural network model. *Journal of Sound and Vibration*, 299(4-5):933–947, 2 2007.

[95] Rahat Yasir, Md Ashiqur Rahman, and Nova Ahmed. Dermatological disease detection using image processing and artificial neural network. In *8th International Conference on Electrical and Computer Engineering: Advancing Technology for a Better Tomorrow, ICECE 2014*, 2015.

[96] J M Corchardoa, N Rees', C Fyfea, and B Leesa. Study and Comparison of Multilayer Perceptron NN and Radial Basis Function NN in Oceanographic Forecasting. Technical report.

[97] Wei Tang, Tao Shan, Xunwang Dang, Maokun Li, Fan Yang, Shenheng Xu, and Ji Wu. Study on a Poisson's equation solver based on deep learning technique. In *2017 IEEE Electrical Design of Advanced Packaging and Systems Symposium, EDAPS 2017*, 2018.

[98] Karen Simonyan and Andrew Zisserman. Very deep convolutional networks for large-scale image recognition. In *3rd International Conference on Learning Representations, ICLR 2015 - Conference Track Proceedings*, 2015.

[99] Christian Szegedy, Wei Liu, Yangqing Jia, Pierre Sermanet, Scott Reed, Dragomir Anguelov, Dumitru Erhan, Vincent Vanhoucke, and Andrew Rabinovich. Going deeper with convolutions. In *Proceedings of the IEEE Computer Society Conference on Computer Vision and Pattern Recognition*, 2015.

[100] Jia Deng, Wei Dong, Richard Socher, Li-Jia Li, Kai Li, and Li Fei-Fei. ImageNet: A large-scale hierarchical image database. 2010.

[101] Jessica Chani-Cahuana, Christian Fager, and Thomas Eriksson. Lower Bound for the Normalized Mean Square Error in Power Amplifier Linearization. *IEEE Microwave and Wireless Components Letters*, 2018.

[102] Sudheer Ch, Nitin Anand, B. K. Panigrahi, and Shashi Mathur. Streamflow forecasting by SVM with quantum behaved particle swarm optimization. *Neurocomputing*, 2013.

[103] Gareth James, Daniela Witten, Trevor Hastie, and Robert Tibshirani. *An introduction to Statistical Learning.* 2000.

[104] Ilkay Altintas, Chad Berkley, Efrat Jaeger, Matthew Jones, Bertram Ludäscher, and Steve Mock. Kepler: An extensible system for design and execution of scientific workflows. In *Proceedings of the International Conference on Scientific and Statistical Database Management, SSDBM*, 2004.

[105] Bertram Ludäscher, Ilkay Altintas, Chad Berkley, Dan Higgins, Efrat Jaeger, Matthew Jones, Edward A. Lee, Jing Tao, and Yang Zhao. Scientific workflow management and the Kepler system. In *Concurrency Computation Practice and Experience*, 2006.

[106] Stephan Dreiseitl and Lucila Ohno-Machado. Logistic regression and artificial neural network classification models: A methodology review. *Journal of Biomedical Informatics*, 2002.

[107] Jacek M Zurada, Aleksander Malinowski, and Ian Cloete+. Sensitivity Analysis for Minimization of Input Data Dimension for Feedforward Neural Network. Technical report.

[108] Mateusz Buda, Atsuto Maki, and Maciej A. Mazurowski. A systematic study of the class imbalance problem in convolutional neural networks. *Neural Networks*, 106:249–259, 2018.

[109] C. E. Shannon. A Mathematical Theory of Communication. *Bell System Technical Journal*, 1948.

[110] Yue Wu, Yicong Zhou, George Saveriades, Sos Agaian, Joseph P. Noonan, and Premkumar Natarajan. Local Shannon entropy measure with statistical tests for image randomness. *Information Sciences*, 2013.

[111] P Grünwald and P. Vitányi. Kolmogorov Complexity and Information Theory. *Journal of Logic, Language and Information*, 12:497–529, 2003.

[112] A. N. Kolmogorov. On tables of random numbers. *Theoretical Computer Science*, 207(2):387–395, 11 1998.

[113] Adel Omrani, Mahdi Moghadasi, and Mojtaba Dehmollaian. Localisation and permittivity extraction of an embedded cylinder using decomposition of the time reversal operator. *IET Microwaves, Antennas & Propagation*, 14(9):851–859, 2020.